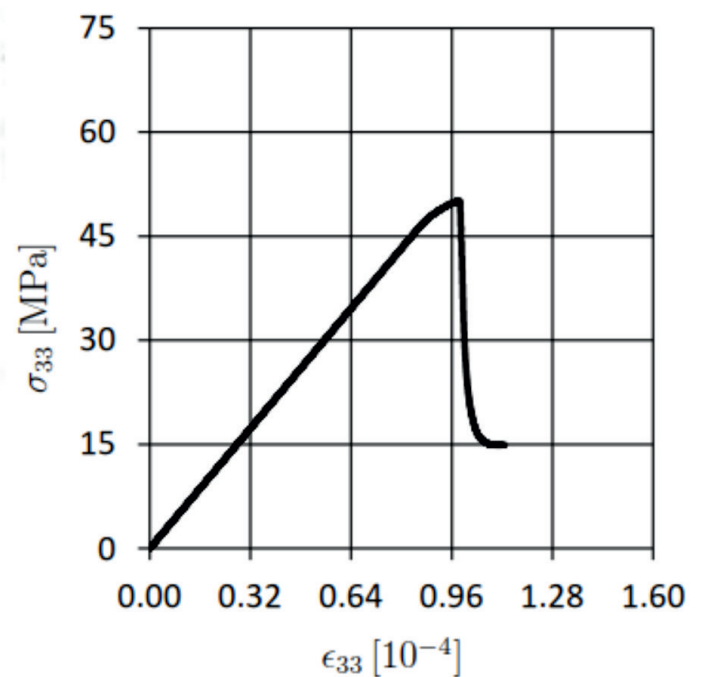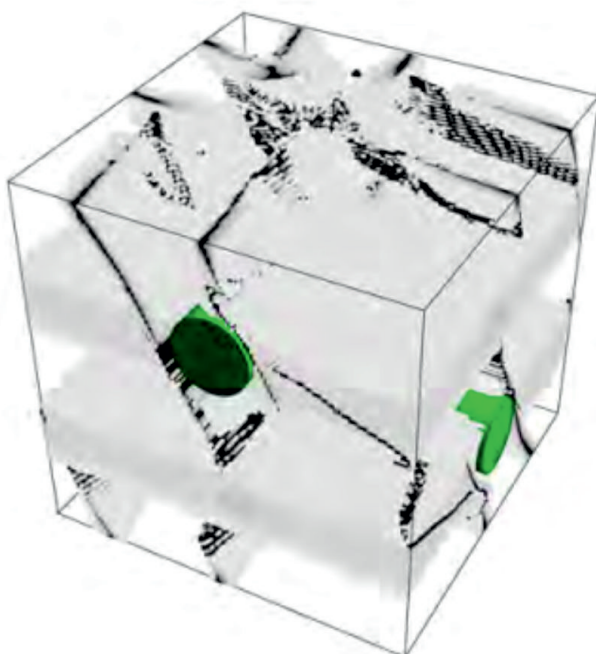**RU**B

An algorithm for damage mechanics based on the fast fourier transform

Christoph Moos

Dissertation

An Algorithm for Damage Mechanics Based on the Fast Fourier Transform

Zur Erlangung des akademischen Grades

Dr.-Ing.

vorgelegt der

Fakultät für Maschinenbau

an der Ruhr-Universität Bochum

von

Christoph Moos,
geb. 15.04.1983 in Iserlohn-Letmathe
Bochum 2013

Bochum, November 2013   Christoph Moos

Contents

1 Introduction

One of the basic phenomena an engineer of any discipline encounters is fatigue of design material, or, in more words, the increasing degradation of material properties in structural members under service conditions, no matter whether service loads are constant or time dependent (dynamic). Many different aspects are touched by this very general specification, like crack initiation, crack propagation, chemical reaction and others. Over the course of the twentieth century a vast body of theories and experimental investigation has taken place, and research is still going on in all of the related areas. Probably the two most mathematically grounded theories are fracture mechanics and damage mechanics, both developed within the framework of continuum mechanics [7, 89]. In fracture mechanics researchers investigate the stress fields in the vicinity of discretely modeled cracks in a continuum, as well as their impact on macroscopic, phenomenological properties, and it is tried to calculate the forces driving crack propagation. The approach in damage mechanics is a different one: damage is interpreted as a thermodynamic state of a solid, affecting its properties like elastic stiffness, yield limit, creep rate etc. It is treated as a continuous field variable (usually labeled d) with spatial dependence. This implies that material flaws like cavities or cracks are very small compared to specimen dimensions, and are distributed statistically homogeneous, at least when observation is restricted to finite regions of the solid. Both approaches have their justification, of course. The appeal of damage mechanics is that it is applicable to simulation of macroscopic bodies more easily, and theoretically it gives more directly insight into those aspects of fatigue that are important to engineers.

A publication by Kachanov from 1958 [76] is accepted by many authors as the birth of damage mechanics. There a scalar field variable d was introduced to help investigate tertiary creep and creep rupture. The main idea was that micropores reduce the cross section area of a specimen in a tensile test, and the ratio between pore cross sectional area and specimen cross section is labeled d

$$d = \frac{A_{\text{pores}}}{A_{\text{specimen}}}.$$

If the area in a plane perpendicular to an external load is reduced, the stresses acting on that plane increase, and this leads to increasing deformation when the elastic stiffness of the material remains the same. Macroscopically this is observed as a loss in stiffness of the specimen. An analogous interpretation of damage is therefore a reduction of apparent material stiffness. Later authors (e.g. in [25]) interpreted d as a thermodynamic state variable, making techniques from classical thermodynamics applicable to the concept. In the following decades additional variables have been introduced to account for different damage mechanisms, and tensorial quantities have been used to model anisotropic damage [89].

Although sixty years have passed since the publication by Kachanov, a lot of active research is still done on the field. In a survey paper from 2000 Krajcinovic [79] pointed out that the main task of damage mechanics, i.e. prediction of remaining structural reliablility, had not been achieved to a satisfactory degree, and he claimed that this hampered wide acceptance of

the methods in industry. The literature of the last decade indeed shows an increased number of papers with focus on engineering challenges, and Lemaitre claims already in 2005 that damage mechanics has found its way into industry [89]. Nonetheless theoretical papers on the topic continue to be published, for example Alves [6] on exact evaluation of stiffness degradation, Turcotte [145] on scaling laws in damage mechanics, Dattoma et. al. [31] on non-linear damage models, Wahab [3] on interaction between damage and adhesive friction and Menzel [101] on anisotropic damage at large strains. Examples of applied damage mechanics can be found in Lee [85] and Sadd [128], who model deterioration of asphalt concrete, Main [95], Weiya [151] or Najo [109] with geophysical applications, and Li [90] with a publication on fiber reinforced concrete or Nguyen [112] on concrete. An example from mechanical engineering is found in [120] by Perrin who modeled creep rupture of ferritic steel and finally an example from electrical engineering: Gomez and Basaran who investigated damage of microelectronics solder joints [56]. All these papers date from 2000 or later, and the list presented here is far from complete. The intention is to show the relevance the topic still has in the scientific community.

The concept of damage mechanics is based on a two-scale ansatz. On a microscale, with typical dimension of several times the length of microdefects, a discrete distribution of pores, cracks and cavities is assumed, and stress and strain fields have a highly heterogeneous character. The details of these are not accounted for, since the defects are abstracted as the damage parameter that models their overall effect on the stress and strain fields at a macroscopic scale. The perturbations are not considered. The abstract procedure of simplification of microscopic patterns into average quantities is usually called homogenization [108]. In many cases of practical importance a further distinction of length scales is needed. This can be the case in mechanical engineering, where defect length scales are small compared to grain size, and typical grain size itself is small compared to dimensions of a machine part. The three cases are often labeled micro-, meso- and macroscale, respectively. An example from civil engineering can be found in steel reinforced concrete, where the steel fibers are large compared to microcracks in the concrete matrix, and the structural dimensions are large compared to fiber size. Even more than three different length scales can be important in geological investigations.

In these cases it can be prohibitively expensive in the sense of computational costs to directly simulate the mesostructure, thus an additional scale separation in modeling is applied. This could be done by postulation of additional assumptions that treat the effects of both micro- and mesoscale patterns on the macroscale. In many cases, however, a more straight forward approach is used. The model for the macroscopic structure assumes homogeneous distribution of material properties, and is analyzed by use of the finite element method. The stress strain relationship at the integration points, that is needed to calculate the element stiffness matrices, is obtained by use of an additional boundary value problem. A model of a small volume of the structure is proposed that incorporates details about the microstructure, e.g. grain size or fiber geometry in the previously mentioned examples. The local stress and strain fields are calculated, and a local damage model as described above is used. Once these results are obtained the material tangent is calculated and stored for subsequent use in a macroscopic load step. This approach is called Multiscale Finite Element Method (MsFEM).

This approach is relatively new, which is understandable since its practicability depends on the availability of large computational power. From the mathematical point of view this is a topic from numerical analysis of elliptic partial differential equations with oscillating

coefficients, and questions arise about convergence, error estimates and the like. Efendiev analyzed convergence issues [39], nonlinear problems [37], as does Allaire [4], or the case of highly oscillating coefficients [40]. Ohlberger provides error estimates [114] and Arbogast and Kouznetsova discuss several solution strategies [9, 77]. A comprehensive overview about this theory is found in [38]. The MsFEM is not restricted to damage models of course, but to any physical problem that allows scale separation, like fluid mechanics [1, 2, 37, 98] or the simulation of earthquakes [70]. However, there are many examples for the use of MsFEM in damage mechanics, for example in aluminium matrix composites [134] or mason brick works [146], other examples can be found in [5, 48, 138, 150]. As was the case for damage mechanics, it is not intended to give a complete list of scientific articles but rather a selection of important articles to emphasize the interest in the topic.

This method has proven to be utile in many cases although it has one major disadvantage: it comes along with very high computational costs. At the macroscopic scale the stiffness matrix has to be assembled and an iterative procedure has to be employed to find the solution to the non-linear problem. The same has to be repeated for the submodels on all the integration points where detailed analysis is necessary. Multi core systems with large memory capacities as well as much CPU power have to be used. In order to increase to practicability of the MsFEM it is desirable to improve the efficiency of the involved numerical procedures.

The aim of this thesis is to provide steps in this direction. A damage mechanics model is proposed and an efficient numerical algorithm is presented to find solutions to the boundary value problem. The algorithm is based on the fast Fourier transform and can be executed efficiently on multi core computers. Periodic boundary conditions are automatically applied and thus the results are suitable for further use in MsFEM analyses. The results are mesh objective and the relationship between averaged stresses and strains reproduces the load curve typical to quasibrittle damage processes.

The structure of this thesis resembles the working plan on this project. In chapter 2 the theoretical background of continuum mechanics, fracture and damage mechanics is revisited, in order to give an orientation for further chapters. In sec. 3.1 a numerical algorithm is discussed that was published by Moulinec and Suquet in the late nineties [105–107]. It is based on fast Fourier transform and designed to calculate the overall elastic properties of composites with complex, periodic microstructure. In sec. 3.2 a damage model is formulated on thermodynamic grounds. It is given in form of the Gibbs free energy and a dissipation potential. The principle of the minimum of the dissipation potential [63] is applied to derive the equations governing the process. A Helmholtz like partial differential equation and a scalar algebraic equation are obtained this way. The Helmholtz equation is transformed into discrete Fourier space and the system of equations is solved with fixed point iteration method. Solution of the linear elastic part of the algorithm resembles the older algorithm by Suquet, but additional steps are inserted to include the nonlinear part. A discussion of the numerical uncertainty follows and it is shown that the accumulation of round-off errors remains small after a large number of iterations.

In chapters 4 and 5 the general model behavior is investigated. A convergence analysis is carried out, mesh objectivity of the results is ensured, a parameter study is presented and results for different examples are shown and discussed. In section 5.3 an example for combination of the presented algorithm with the finite element method, in the context of MsFEM, is given and its results are discussed. Such a method could be used on multi core systems to analyze complex problems involving damage at the microscale.

2 Theoretical Background

This chapter's purpose is to clarify the theoretical basis upon which the current work was carried out. The basic theory in computational analysis of material behavior is the mathematical theory of linear elasticity. Many more advanced theories are based on its results. The first section of this chapter recalls the central assumptions, theorems and solutions of this theory, to facilitate the reader's orientation and understanding. Other fields of classical mechanics important here are the Linear Elastic Fracture Mechanics and Damage Mechanics. At the end the basic properties of the Discrete Fourier Transform are listed because of the important role this method plays in the algorithms used within this work.

The following conventions about notation will be used throughout this text:

- Indexed quantities like vectors, tensors, matrices etc. are presented as bold greek or latin, lower or upper case letters (e.g. $\boldsymbol{\alpha}, \mathbf{u}, \mathbf{v}, \boldsymbol{\sigma}, \mathbf{C}$).

- The Einstein summation convention is used, if not explicitly stated otherwise:

$$v_i w_i = \sum_{\nu=1}^{3} v_\nu w_\nu$$

- The inner product (summation over one index) is denoted with the operator $(\cdot)$:

$$\mathbf{v} \cdot \mathbf{w} = v_i w_i.$$

- A linear mapping between two vector spaces is called a tensor. The mapping between two vectors $\mathbf{v} = v_i \mathbf{e}_i$ and $\mathbf{w} = w_i \mathbf{e}_i$ is called second order tensor, e.g.

$$\mathbf{v} = \mathbf{T} \cdot \mathbf{w} = T_{ij} w_l \delta_{jl} \mathbf{e}_i = T_{ij} w_j \mathbf{e}_i,$$

where δ_{ij} is the Kronecker Delta defined as

$$\delta_{ij} = \mathbf{e}_i \cdot \mathbf{e}_j.$$

The transpose $\mathbf{T}^T$ of a $\mathbf{T}$ is the unique tensor with the property

$$(\mathbf{T} \cdot \mathbf{v}) \cdot \mathbf{w} = \left(\mathbf{v} \cdot \mathbf{T}^T\right) \cdot \mathbf{w}.$$

The mapping from one second order tensor into another is called fourth order tensor and the corresponding operator symbol is the colon:

$$\begin{aligned} \boldsymbol{\alpha} &= \mathbf{C} : \boldsymbol{\beta}, \\ \alpha_{ij} &= C_{ijkl} \delta_{km} \delta_{ln} \beta_{mn} = C_{ijkl} \beta_{kl}. \end{aligned}$$

- It is common practice to denote the partial derivative of a function u_i with respect to the variable x_j as:

$$\frac{\partial u_i}{\partial x_j} = u_{i,j}.$$

For a scalar field $u(\mathbf{x})$ and a vector $\mathbf{v} = v_i \mathbf{e}_i$ the Gradient, Curl and Divergence are understood as:

$$\begin{aligned}
\operatorname{grad} u(\mathbf{x}) &= \nabla u(\mathbf{x}) = \frac{\partial u}{\partial x_i} \mathbf{e}_i \\
\operatorname{grad} \mathbf{v} &= \nabla \mathbf{v} = v_{i,j} \mathbf{e}_i \mathbf{e}_j \\
\operatorname{curl} \mathbf{v} &= \nabla \times \mathbf{v} = \epsilon_{ijk} v_{k,j} \mathbf{e}_i \\
\Delta \mathbf{v} &= \nabla\nabla\mathbf{v} \,(\text{Laplacian operator})
\end{aligned}$$

with the three dimensional alternator:

$$\epsilon_{ijk} = \begin{cases}
+ & 1 \text{ if } (i,j,k) \text{ is an even permutation of } (1,2,3) \\
- & 1 \text{ if } (i,j,k) \text{ is an odd permutation of } (1,2,3) \\
& 0 \text{ if } (i,j,k) \text{ is not a permutation of } (1,2,3).
\end{cases}$$

2.1 Theory of Linear Elasticity

The mathematical theory of elasticity aims at describing the displacements and deformations of parts of a body as a response to a system of external forces acting on the body. It is formulated in the context of classical Newtonian Mechanics, as to say it embraces the classical concepts of space, time and force, [93].

The mathematical system of reference is a coordinate basis in $\mathbb{R}^3$ with designated basis vectors $\mathbf{e}_1$, $\mathbf{e}_2$ and $\mathbf{e}_3$. Throughout this text a Cartesian basis is used always although any other coordinate system could be used in principle. A point is either referenced to by his Cartesian coordinates x_i or by the corresponding position vector $\mathbf{x} = x_i \mathbf{e}_i$. A physical body $\mathcal{D}$ is then described by the subset $\mathcal{D} \subseteq \mathbb{R}^3$ that contains all the points occupied by the body. A first basic assumption is that the mass of a body is distributed continuously in space. Formally this can be expressed by the condition that the mass of a body is always the volume integral of a density field over the region $\mathcal{D}$, [61]:

$$m = \int_{\mathcal{D}} \rho \, dV. \tag{2.1}$$

During a deformation process the shape of the body changes, and the material point formerly lying at $\mathbf{x}$ now occupies the point $\mathbf{x}'$, for example. The region $\mathcal{D}'$ occupied after deformation may or may not be the same as $\mathcal{D}$. The displacement is a function of the original position of each material point:

$$\mathbf{u}(\mathbf{x}) = \mathbf{x} - \mathbf{x}'. \tag{2.2}$$

In situations where $\mathbf{u}$ and $\nabla\mathbf{u}$ are small, the linear theory can be applied. When this assumption is no longer valid a theory of elasticity with non-linear kinematics is more appropriate.

A more in-depth explanation on what small does mean and how big the error will be is given in [61]. The infinitesimal strain tensor used in the linear theory is defined as

$$\boldsymbol{\epsilon}(\mathbf{x}) = \frac{1}{2}\left(\nabla\mathbf{u} + \nabla^T\mathbf{u}\right). \tag{2.3}$$

The strain $\boldsymbol{\epsilon}$ is symmetric:

$$\epsilon_{ij} = \epsilon_{ji}. \tag{2.4}$$

The compatibility theorem states that any strain field connected to a smooth and differentiable displacement field by (2.3) satisfies the compatibility equation:

$$\nabla \times \boldsymbol{\epsilon}(\mathbf{x}) \times \nabla = 0. \tag{2.5}$$

This condition is also valid vice versa: For any strain field that satisfies (2.5) the theorem assures its integrability, and a uniquely determined displacement field exists that is connected to the strain field via (2.3). The line integral

$$\mathbf{u}(\mathbf{x}) = \int_{\mathbf{x}_0}^{\mathbf{x}} \left[\boldsymbol{\epsilon}(\mathbf{y}) + \operatorname{grad}\boldsymbol{\epsilon} \cdot (\mathbf{x} - \mathbf{y}) + (\mathbf{x} - \mathbf{y}) \cdot \operatorname{grad}\boldsymbol{\epsilon}\right]\, \mathrm{d}\mathbf{y} \tag{2.6}$$

is path-independent and $\mathbf{u}(\mathbf{x})$ is the displacement field with the desired property. Eq. (2.6) is called Michel-Cesaro formula. Alternative formulations of the compatibility theorem are available, see [61].

A further important theorem is called Cauchy-Poisson theorem. It states that from assumption of balance of linear and angular momentum follows the existence of a symmetric second order tensor $\boldsymbol{\sigma}$ belonging to the linear mapping between the vector $\mathbf{n}(\mathbf{x})$ normal to a surface onto the force or traction vector $\mathbf{t}(\mathbf{x})$ acting on that surface:

$$\mathbf{t}(\mathbf{x}) = \boldsymbol{\sigma} \cdot \mathbf{n}(\mathbf{x}). \tag{2.7}$$

The surface can be a real one (surface of body $\mathcal{D}$) or an imaginative one cutting through the body. A second consequence from the theorem is that $\boldsymbol{\sigma}$ satisfies the equation of motion

$$\operatorname{div}\boldsymbol{\sigma} + \mathbf{f} = \rho\ddot{\mathbf{u}} \tag{2.8}$$

where $\mathbf{f}$ are external volumetric forces acting on the body and $\ddot{\mathbf{u}}$ is the second time derivative of the displacement field. It has to be mentioned that (2.8) is not restricted to the linear theory but is rather generally valid in continuum mechanics.

The infinitesimal strain tensor $\boldsymbol{\epsilon}$ and stress tensor $\boldsymbol{\sigma}$ are connected via a constitutive law, namely Hooke's law in linear elasticity:

$$\boldsymbol{\sigma} = \mathbf{C} : \boldsymbol{\epsilon}. \tag{2.9}$$

The fourth order tensor $\mathbf{C}$ is the elasticity tensor or stiffness tensor. For isotropic materials its components are:

$$C_{ijkl} = \lambda\delta_{ij}\delta_{kl} + \mu\left(\delta_{ik}\delta_{jl} + \delta_{il}\delta_{jk}\right). \tag{2.10}$$

The coefficients λ and μ are the Lamé-parameters and may or may not depend on the position $\mathbf{x}$. In engineering applications Young's modulus E and Poisson ratio ν are customarily used. They are related to λ and μ:

$$E = \frac{\mu(3\lambda + 2\mu)}{\lambda + \mu} \quad \text{and} \quad \nu = \frac{\lambda}{2(\lambda + \mu)}. \tag{2.11}$$

Equations (2.9) and (2.3) can be substituted into (2.8) to obtain Navier's equation, a partial differential equation for displacement:

$$\frac{1}{2}\text{div}\mathbf{C} : \left(\nabla\mathbf{u} + \nabla\mathbf{u}^T\right) + \frac{1}{2}\mathbf{C} : \text{div}\left(\nabla\mathbf{u} + \nabla\mathbf{u}^T\right) + \mathbf{f} = 0. \tag{2.12}$$

For constant coefficients the classical form is obtained:

$$\mu\Delta\mathbf{u} + (\lambda + \mu)\nabla\text{div}\mathbf{u} + \mathbf{f} = 0. \tag{2.13}$$

In addition to volumetric forces $\mathbf{f}$ the body can be subjected to areal forces $\mathbf{t}_S$ acting either on the whole surface or on parts of it. If the displacement is prescribed on parts of the surface, the formulation of the boundary value problem of linear elasticity is complete. On each point $\mathbf{x} \in \mathcal{S}$ belonging to the surface either traction or displacement can be prescribed, but not both at a time. Parts of $\mathcal{S}$ where neither of the two is prescribed are called free surface. If traction and displacement are prescribed on different parts of the surface, the problem is called mixed boundary value problem. If only displacements are prescribed it is called displacement boundary value problem and consequently a problem where only tractions are prescribed is called a traction boundary value problem. If the acoustic tensor $\mathbf{T}$, defined as

$$\mathbf{T} = C_{ijkl}n_j n_l \mathbf{e}_i \mathbf{e}_k, \tag{2.14}$$

with a normal vector $\mathbf{n} = n_i \mathbf{e}_i$, is positive definite irrespective of the choice of $\mathbf{n}$, then the existence of a solution for the boundary value problems is assured. Positive definiteness of $\mathbf{T}$ poses restrictions on the values of λ and μ:

$$\mu > 0 \quad \text{and} \quad \lambda + 2\mu > 0. \tag{2.15}$$

In addition it has been shown that any two solutions for the mixed problem are equal except for a rigid displacement part. For the other two types of boundary value problems the conditions for existence and uniqueness are slightly different.

A solution to the displacement, traction or mixed boundary value problem minimizes the elastic energy. This theorem is known as principle of minimum potential energy. If the potential energy is written defined as $\Pi(\boldsymbol{\epsilon})$,

$$\Pi(\boldsymbol{\epsilon}) = \frac{1}{2}\int_{\mathcal{D}} \boldsymbol{\epsilon} : \mathbf{C} : \boldsymbol{\epsilon}\, dV - \int_{\mathcal{D}} \mathbf{f} \cdot \mathbf{u}\, dV - \int_{\partial\Gamma} \mathbf{t} \cdot \mathbf{u}\, dA, \tag{2.16}$$

then the principle is written formally as

$$\Pi(\tilde{\boldsymbol{\epsilon}}) \leq \Pi(\boldsymbol{\epsilon}) \tag{2.17}$$

if $\tilde{\boldsymbol{\epsilon}}$ is a solution of the problem and $\boldsymbol{\epsilon}$ any other field that corresponds to a kinematically admissible state. An analogous theorem has been formulated for the elastic complementary

energy. These principles are the basis for several solution techniques either analytical or numerical.

Different mathematical representations of a solution to a given boundary value problem are possible, some of them are now represented:

Boussinesq-Papkovich-Neuber solution [61]: Let $\mu \neq 0$, $\nu \neq \frac{1}{2}$ and $\nu \neq 1$. If φ and $\boldsymbol{\psi}$ are fields whose restriction to $\mathcal{D}$ is at least three times differentiable, and that satisfy

$$\Delta\boldsymbol{\psi} = -\frac{1}{\mu}\mathbf{f} \quad \text{and} \quad \Delta\varphi = \frac{1}{\mu}\mathbf{p}\cdot\mathbf{f}, \tag{2.18}$$

then $\mathbf{u}$ with

$$\mathbf{u} = \boldsymbol{\psi} - \frac{1}{4(1-\nu)}\nabla(\mathbf{p}\cdot\boldsymbol{\psi} + \varphi) \tag{2.19}$$

is a solution to the partial differential equations (2.13). The representation (2.19) is complete, i.e. any elastic displacement field corresponding to external forces $\mathbf{f}$ can be represented this way.

Boussinesq-Somigliana-Galerkin solution [61]: Let $\mathbf{g}$ be a vector field that is at least four times differentiable at $\mathcal{D}$ and that satisfies

$$\Delta\Delta\mathbf{g} = -\frac{1}{\mu}\mathbf{f}. \tag{2.20}$$

Then $\mathbf{u}$ with

$$\mathbf{u} = \Delta\mathbf{g} - \frac{1}{2(1-\nu)}\nabla\text{div}\mathbf{g} \tag{2.21}$$

is a solution to the boundary value problem (2.13). Representation (2.20) is complete.

Kelvin's solution \ Green's function [61]: A solution can also be given for the case that a singular load $\mathbf{F} = F_i\mathbf{e}_i$ acts at position $\mathbf{y}$:

$$\mathbf{f} = \mathbf{F}\delta(\mathbf{x} - \mathbf{y}), \tag{2.22}$$

where

$$\delta(\mathbf{z}) = \begin{cases} 1 & \text{if} \quad \mathbf{z} = 0 \\ 0 & \text{if} \quad \mathbf{z} \neq 0 \end{cases}. \tag{2.23}$$

The displacement field corresponding to $\mathbf{F}$ is given as:

$$u_i(\mathbf{x}) = \frac{1}{16\pi\mu(1-\nu)}\left[\frac{(x_i - y_i)(x_j - y_j)F_j}{\|\mathbf{x} - \mathbf{y}\|^2} + (3 - 4\nu)F_i\right]. \tag{2.24}$$

If $\mathbf{F}$ is chosen as singular force of absolute value $\|\mathbf{F}\| = 1$, one arrives at the Green's Function for an infinite, homogeneous and isotropic body:

$$G_{ij}(\mathbf{x}) = \frac{1}{16\pi\mu(1-\nu)}\left[\frac{(x_i - y_i)(x_j - y_j)}{\|\mathbf{x} - \mathbf{y}\|^2} + (3 - 4\nu)\delta_{ij}\right]. \tag{2.25}$$

For any arbitrary body force field $\mathbf{f}(\mathbf{x})$ in an infinite, homogeneous isotropic body the displacement field can be formulated in an integral representation form by virtue of (2.25):

$$\mathbf{u}(\mathbf{x}) = -\int_{-\infty}^{\infty} \mathbf{G}(\mathbf{x} - \mathbf{y}) \cdot \mathbf{f}(\mathbf{y}) \, \mathrm{d}\mathbf{y}. \tag{2.26}$$

If the body under consideration is a bounded region, additional correction terms have to be added to (2.25). Naturally this is only possible for very simple shapes. Pan and Chou [116] give the Green's Function in explicit form for an infinite transversely isotropic Solid, but they have to pose certain restrictions on the components of the stiffness tensor. Via application of the Stroh-formalism [143] Ting obtained an explicit representation of the Green's function for linear elastic materials of general anisotropy, see [142]. Solutions for special cases are given by Luco [94], Yuan et. al. [156] and Pan [115]. Some aspects of the numerical evaluation can be found in Barnett [12], for example. Among other applications the Green's function plays an important role in homogenization methods for materials with heterogeneous microstructure, see for example in Willis [154].

Instead of formulating the problem of elasticity in terms of displacements, as in (2.13), it can be formulated in terms of stresses. Combination of eqs. (2.5), (2.8) and (2.9) leads to the Beltrami-Michel compatibility equation of stresses, [62]:

$$\Delta\boldsymbol{\sigma} + \frac{1}{1+\nu}\nabla\nabla\left(\mathrm{tr}\boldsymbol{\sigma}\right) + \left(\nabla\sigma + \nabla\sigma^T\right) + \frac{\nu}{1-\nu}\left(\mathrm{div}\mathbf{f}\right)\mathbf{I} = 0. \tag{2.27}$$

Any stress field $\boldsymbol{\sigma}$ satisfying (2.27) is an elastic stress field. Beltrami found that in the absence of body forces any stress that can be expressed as

$$\boldsymbol{\sigma} = \nabla \times \mathbf{A} \times \nabla, \tag{2.28}$$

where $\mathbf{A} = \mathbf{A}^T$ is a symmtetric tensor function (stress function), satisfies (2.27). A special choice of $\mathbf{A}$ is

$$\mathbf{A} = \begin{pmatrix} 0 & 0 & 0 \\ 0 & 0 & 0 \\ 0 & 0 & \Phi \end{pmatrix} \tag{2.29}$$

the Airy stress function Φ, satisfying the biharmonic equation

$$\Delta\Delta\Phi = 0. \tag{2.30}$$

The stresses in cartesian coordinates are related to Φ as:

$$\sigma_{11} = \Phi_{,22}, \quad \sigma_{22} = \Phi_{,11}, \quad \sigma_{12} = -\Phi_{,12}, \quad \sigma_{13} = \sigma_{23} = \sigma_{33} = 0. \tag{2.31}$$

The above presented list of fundamental representations of elastic stress and displacement fields is by no means complete. Additional representations have been given by Love or Boussinesq, for example. Classical texts on the mathematical theory of linear elasticity are Love [93], Gurtin [61] and [62], Lekhnitski [87] or Timoshenko [141]. Monographs with special emphasis on anisotropic media have been written by Hearmon [66] and Ting [143].

2.2 Hooke's Law

The generalized Hooke's Law (2.9) reads in index notation:

$$\sigma_{ij} = C_{ijkl}\epsilon_{kl}. \tag{2.32}$$

The 81 components C_{ijkl} are not independent to each other. The fact that $\mathbf{C}$ is a linear mapping from one vector space of symmetric second order tensors into another vector space of symmetric second order tensors requires minor symmetry of $\mathbf{C}$ [62]:

$$C_{ijkl} = C_{jikl} = C_{jilk} = C_{ijlk}. \tag{2.33}$$

Major symmetry, i.e.:

$$C_{ijkl} = C_{klij}, \tag{2.34}$$

ensures the existence of the elastic potential ψ_0. The relationships (2.33) and (2.34) reduce the number of independent constants to 21 [143]. It is common practice in computational analysis to take advantage of that fact and to write down (2.32) in matrix form:

$$
\begin{pmatrix} \sigma_{11} \\ \sigma_{22} \\ \sigma_{33} \\ \sigma_{12} \\ \sigma_{23} \\ \sigma_{13} \end{pmatrix} =
\begin{pmatrix}
C_{1111} & C_{1122} & C_{1133} & C_{1112} & C_{1123} & C_{1113} \\
C_{1122} & C_{2222} & C_{2233} & C_{2212} & C_{2223} & C_{1223} \\
C_{1133} & C_{2233} & C_{3333} & C_{3312} & C_{3323} & C_{3313} \\
C_{1112} & C_{2212} & C_{3312} & C_{1212} & C_{1223} & C_{1213} \\
C_{1123} & C_{2223} & C_{3323} & C_{1223} & C_{2323} & C_{2313} \\
C_{1113} & C_{2213} & C_{3313} & C_{1213} & C_{2313} & C_{1313}
\end{pmatrix} \cdot
\begin{pmatrix} \epsilon_{11} \\ \epsilon_{22} \\ \epsilon_{33} \\ 2\epsilon_{12} \\ 2\epsilon_{23} \\ 2\epsilon_{13} \end{pmatrix}. \tag{2.35}
$$

By changing the indexes in (2.35) following the rule

$$11 \to 1, \quad 22 \to 2, \quad 33 \to 3, \quad 12 \to 4, \quad 23 \to 5, \quad 13 \to 6, \tag{2.36}$$

the Voigt notation is obtained that is frequently used in anisotropic elasticity [66, 143, 149]. The matrix in (2.35) does not have the properties of a tensor any more. A formulation of $\mathbf{C}$ as a six-dimensional second rank tensor can be found in [100] and reads:

$$
\mathbf{C}^{6\times6} =
\begin{pmatrix}
C_{1111} & C_{1122} & C_{1133} & \sqrt{2}C_{1112} & \sqrt{2}C_{1123} & \sqrt{2}C_{1113} \\
C_{1122} & C_{2222} & C_{2233} & \sqrt{2}C_{2212} & \sqrt{2}C_{2223} & \sqrt{2}C_{1223} \\
C_{1133} & C_{2233} & C_{3333} & \sqrt{2}C_{3312} & \sqrt{2}C_{3323} & \sqrt{2}C_{3313} \\
\sqrt{2}C_{1112} & \sqrt{2}C_{2212} & \sqrt{2}C_{3312} & 2C_{1212} & 2C_{1223} & 2C_{1213} \\
\sqrt{2}C_{1123} & \sqrt{2}C_{2223} & \sqrt{2}C_{3323} & 2C_{1223} & 2C_{2323} & 2C_{2313} \\
\sqrt{2}C_{1113} & \sqrt{2}C_{2213} & \sqrt{2}C_{3313} & 2C_{1213} & 2C_{2313} & 2C_{1313}
\end{pmatrix}. \tag{2.37}
$$

This operator is a linear mapping from the six-dimensional vector space into another, and stress and strains are represented as six-dimensional first order tensors:

$$
\boldsymbol{\sigma}^6 =
\begin{pmatrix} \sigma_{11} \\ \sigma_{22} \\ \sigma_{33} \\ \sqrt{2}\sigma_{12} \\ \sqrt{2}\sigma_{23} \\ \sqrt{2}\sigma_{13} \end{pmatrix}
\quad \text{and} \quad
\boldsymbol{\epsilon}^6 =
\begin{pmatrix} \epsilon_{11} \\ \epsilon_{22} \\ \epsilon_{33} \\ \sqrt{2}\epsilon_{12} \\ \sqrt{2}\epsilon_{23} \\ \sqrt{2}\epsilon_{13} \end{pmatrix}. \tag{2.38}
$$

Hooke's Law reads, consequently:

$$\boldsymbol{\sigma}^6 = \mathbf{C}^{6 \times 6} \cdot \boldsymbol{\epsilon}^6. \tag{2.39}$$

This notation is convenient if complex symbolic formula has to be transferred to computational analysis, as is the case in micromechanics, for example. For isotropic materials the C_{ijkl} are defined as in (2.40), and in six-dimensional tensor notation this reads:

$$\mathbf{C}_{\text{iso}}^{6 \times 6} = \begin{pmatrix} \lambda + 2\mu & \lambda & \lambda & 0 & 0 & 0 \\ \lambda & \lambda + 2\mu & \lambda & 0 & 0 & 0 \\ \lambda & \lambda & \lambda + 2\mu & 0 & 0 & 0 \\ 0 & 0 & 0 & 2\mu & 0 & 0 \\ 0 & 0 & 0 & 0 & 2\mu & 0 \\ 0 & 0 & 0 & 0 & 0 & 2\mu \end{pmatrix}. \tag{2.40}$$

2.3 Special Solutions

2.3.1 Eshelby's Solution

We consider the problem of an infinite, homogeneous body not subjected to any external loading. The region is denoted with D. A given subregion Ω of D undergoes a stress-free transformation in shape that is homogeneous throughout D, described by the constant transformation strain $\boldsymbol{\epsilon}^{\text{T}}$. $\boldsymbol{\epsilon}^{\text{T}}$ is the strain in D an observer would measure if the surrounding material was absent. D is called an inclusion and the region $D - \Omega$ is called matrix. Since the transformation of Ω is constrained by the matrix, internal stresses and strains are induced in the matrix as well as in the inclusion. The elastic strains (i.e. strains that are not stress free) can be expressed in terms of the fundamental solution (2.26), see [108]:

$$\epsilon_{ij}(\mathbf{x}) = \int_{\Omega} \left[G_{ik,jl}(\mathbf{x} - \mathbf{y}) - G_{ij,kl}(\mathbf{x} - \mathbf{y}) \right] C_{klmn} \epsilon_{mn}^{\text{T}} \, \mathrm{d}\mathbf{y}. \tag{2.41}$$

One has to remember that one of the opening assumptions was the homogeneity of the body. In case of inhomogeneous bodies ($\mathbf{C} = \mathbf{C}(\boldsymbol{x})$) the expression gets more involved. A tensorial quantity $\mathbf{S}$ is defined,

$$S_{ijmn} = \int_{\Omega} \left[G_{ik,jl}(\mathbf{x} - \mathbf{y}) - G_{ij,kl}(\mathbf{x} - \mathbf{y}) \right] C_{klmn} \, \mathrm{d}\mathbf{y}, \tag{2.42}$$

called Eshelbytensor in honor to J.D. Eshelby, who developed a solution strategy and derived formulas for the problems of spherical and inhomogeneous solutions [44]. Thus (2.41) reads:

$$\epsilon_{ij} = S_{ijkl} \epsilon_{kl}^{\text{T}}. \tag{2.43}$$

$\mathbf{S}$ and accordingly $\boldsymbol{\varepsilon}$ is constant throughout the inclusion if its shape matches an ellipsoid, a basic result obtained in [44]. This conclusion also holds for a spherical inclusion as special case of ellipsoidal inclusions and this phenomenon is sometimes called Eshelby property, e.g. in [96] and [97]. The actual strain within the inclusion is only partly stress free, and Hooke's law reads for points within Ω:

$$\sigma_{ij} = C_{ijkl} \left(\epsilon_{kl} - \epsilon_{kl}^{\text{T}} \right). \tag{2.44}$$

The solution for points outside of Ω is not uniform, although the relation between transformation strain and actual strain can still be expressed as in (2.43), only that $\mathbf{S} = \mathbf{S}(x)$ is dependant on space coordinates. To avoid any confusion: $\mathbf{S}$ always refers to the interior point solution throughout this section. For the exterior point Eshelby tensor refer to [74] or [108]. In [44] Eshelby gave the components of $\mathbf{S}$ for spherical inclusions as:

$$S_{1111} = S_{2222} = S_{3333} = \frac{7 - 5\nu}{15(1 - \nu)},$$

$$S_{1122} = S_{2233} = S_{1133} = S_{3311} = S_{2211} = S_{3322} = \frac{5\nu - 1}{15(1 - \nu)}, \tag{2.45}$$

$$S_{1212} = S_{2323} = S_{3131} = \frac{4 - 5\nu}{15(1 - \nu)}.$$

The parameter ν refers to the Poisson ratio of the elastic material. All components of $\mathbf{S}$ linking shear strains to normal strains in (2.43) are zero, as well as components linking ϵ_{ij} to ϵ_{kl} with $i \neq k$ and $j \neq l$. For ellipsoidal inclusions the solution can be expressed in terms of elliptic integrals, see [44] or [108]:

$$S_{1111} = \frac{3}{8\pi(1 - \nu)} a_1^2 I_{11} + \frac{1 - 2\nu}{8\pi(1 - \nu)} I_1,$$

$$S_{1122} = \frac{1}{8\pi(1 - \nu)} a_2^2 I_{12} - \frac{1 - 2\nu}{8\pi(1 - \nu)} I_1,$$

$$S_{1133} = \frac{1}{8\pi(1 - \nu)} a_3^2 I_{13} - \frac{1 - 2\nu}{8\pi(1 - \nu)} I_1, \tag{2.46}$$

$$S_{1212} = \frac{a_1^2 + a_2^2}{16\pi(1 - \nu)} I_{12} + \frac{1 - 2\nu}{16\pi(1 - \nu)} (I_1 + I_2),$$

with

$$I_1 = \frac{4\pi a_1 a_2 a_3}{(a_1^2 - a_2^2)(a_1^2 - a_3^2)} \left\{ F(\theta, k) - E(\theta, k) \right\}, \tag{2.47}$$

$$I_3 = \frac{4\pi a_1 a_2 a_3}{(a_2^2 - a_3^2)(a_1^2 - a_3^2)} \left\{ \frac{a_2\sqrt{a_1^2 - a_3^2}}{a_1 a_3} - E(\theta, k) \right\},$$

where

$$F(\theta, k) = \int_0^\infty \frac{1}{\sqrt{1 - k^2 \sin^2 w}} \, dw, \quad E(\theta, k) = \int_0^\infty \sqrt{1 - k^2 \sin^2 w} \, dw, \tag{2.48}$$

$$\theta = \sin^{-1}\sqrt{1 - \frac{a_3^2}{a_1^2}}, \qquad k = \sqrt{\frac{a_1^2 - a_2^2}{a_1^2 - a_3^2}}.$$

Relationships between the I_i and tne I_{ij} are the following:

$$I_1 + I_2 + I_3 = 4\pi,$$

$$3I_{11} + I_{12} + I_{13} = \frac{4\pi}{a_1^2}, \tag{2.49}$$

$$3a_1^2 I_{11} + a_2^2 I_{12} + a_3^2 I_{13} = 3I_1,$$

$$I_{12} = \frac{I_2 - I_1}{a_1^2 - a_2^2}.$$

The elliptic integrals F and E in (2.48) have to be computed numerically, but implementations with sufficient accuracy are available in many computer algebra systems and for

programming languages. Cyclic permutation of the indices in equations (2.47) to (2.50) gives the other components of **S**, and the components that are zero for spherical inclusions are zero for ellipsoidal inclusions, too. Mura [108] gives explicit expressions for the cases of penny-shape, oblates, flat ellipsoid and cylindrical inclusions, which alltogether are limiting cases of (2.47) when one or more of the a_i approaches towards 0 or ∞.

The Eshelby tensor has been calculated for different problems, e.g. for inclusions of cuboidal shape by Faivre [47], Sankaran and Laird [129] and Lee, Barnett and Aaronson [86]. Rodin [126] gave the Eshelby tensor in closed form for polyhedral inclusions and proofed that the Eshelby property does not hold for any polyhedron. Further analysis was taken out by Markenscoff [96] and Markenscoff and Lubanda [97] who showed that any inclusion bounded by planes or more generally bounded by non-convex surfaces does not have the Eshelby property.

What makes this solution important is the fact that another problem can be reduced to the already solved inclusion problem: consider an infinite, homogeneous elastic, body D with stiffness $\mathbf{C}^{\mathrm{D}}$ subjected to a constant stress $\boldsymbol{\sigma}^0$. A subdomain of D, again called Ω is occupied by a different material with stiffness $\mathbf{C}^{\mathrm{I}}$. The presence of this inhomogeneity causes a local disturbance of internal stresses, such that the actual stress $\boldsymbol{\sigma} = \boldsymbol{\sigma}(\mathbf{x})$ is not constant anymore. For $\mathbf{x} \to \infty$ the stress will approach $\boldsymbol{\sigma} \to \boldsymbol{\sigma}^0$.

Starting point is again the inclusion problem from the beginning of this section, only that the stiffness of the infinite, homogeneous body is $\mathbf{C}^{\mathrm{D}}$. The strain within the inclusion is given by (2.43) . Adding a constant stress field

$$\sigma_{ij}^0 = C_{ijkl}^{\mathrm{D}} \epsilon_{kl}^0 \tag{2.50}$$

means that the total stress field is now $\sigma_{ij}^0 + \sigma_{ij}$ and the total strain is $\epsilon_{ij}^0 + \epsilon_{ij}$. But within the inclusion Ω they do not comply with Hooke's law, since with (2.44)

$$\sigma_{ij}^0 + \sigma_{ij} = C_{ijkl}^{\mathrm{D}} \left(\epsilon_{kl}^0 + \epsilon_{kl} - \epsilon_{kl}^{\mathrm{T}} \right). \tag{2.51}$$

Now imagine the inclusion to be replaced with another material, that has a stiffness $\mathbf{C}^I$ such that stresses and strains are connected by Hooke's law again:

$$\sigma_{ij}^0 + \sigma_{ij} = C_{ijkl}^{\mathrm{I}} \left(\epsilon_{kl}^0 + \epsilon_{kl} \right). \tag{2.52}$$

Then it follows from (2.51) and (2.52) that

$$C_{ijkl}^{\mathrm{D}} \left(\epsilon_{kl}^0 + \epsilon_{kl} - \epsilon_{kl}^{\mathrm{T}} \right) = C_{ijkl}^{\mathrm{I}} \left(\epsilon_{kl}^0 + \epsilon_{kl} \right). \tag{2.53}$$

Of course, the inhomogeneity problem assumes the stiffness $\mathbf{C}^{\mathrm{I}}$ to be known, but (2.53) allows the inhomogeneity problem to be reduced to the inclusion problem with unknown transformation strain $\epsilon_{ij}^{\mathrm{T}}$. (2.53) carries two unknowns, namely ϵ_{ij} and $\epsilon_{ij}^{\mathrm{T}}$, and together with (2.43) one has two equations to determine them. The strains and stresses can be given, here in symbolic form:

$$\boldsymbol{\varepsilon}^0 + \boldsymbol{\varepsilon} = \left[\mathbf{S} : \mathbf{M}^D : \left(\mathbf{C}^{\mathrm{T}} - \mathbf{C}^0 \right) + \mathbf{I} \right]^{-1} : \boldsymbol{\varepsilon}^0, \tag{2.54}$$

$$\boldsymbol{\sigma}^0 + \boldsymbol{\sigma} = \mathbf{C}^I : \left[\mathbf{S} : \mathbf{M}^D : \left(\mathbf{C}^I - \mathbf{C}^0 \right) + \mathbf{I} \right]^{-1} : \boldsymbol{\varepsilon}^0 \quad \text{within } \Omega, \tag{2.55}$$

$$\boldsymbol{\sigma}^0 + \boldsymbol{\sigma} = \mathbf{C}^D : \left[\mathbf{S} : \mathbf{M}^D : \left(\mathbf{C}^I - \mathbf{C}^0 \right) + \mathbf{I} \right]^{-1} : \boldsymbol{\varepsilon}^0 \quad \text{outside } \Omega. \tag{2.56}$$

S dependes on the shape of the inhomogeneity. One has to remember that it always belongs to the inclusion problem of the matrix material. For example, in case of spherical inclusions the Poisson's ratio of the matrix material has to be chosen when calculating the constants of **S** with (2.45).

2.3.2 William's Solution for cracked half-space

The next section is devoted to a brief review of the important field of fracture mechanics. Although most of this research area goes well beyond the limits of linear elasticity theory, it is grounded on stress analysis within the frame of the latter one. Textbooks on fracture mechanics usually start from linear elasticity, thereby following the historical line of development [7]. The basic assumption in fracture mechanics is the existence of pores or sharp cracks in all natural materials. Therefore stress and strain distribution as well as displacement fields in the vicinity of those is of interest to researchers. Inglis [71] probably was the first who investigated such situations rigorously with the methods of linear elasticity. He investigated elliptic holes in plane stress where one half axis is very large compared to the other. In 1956 Williams [153] investigated a sharp crack in an infinite half space under plane stress conditions. Figure 2.1 illustrates the configuration. Polar coordinates are used, the origin lies on the crack tip. This time a formulation in terms of the Beltrami solution is chosen. Williams postulates the following stress function for the problem:

$$\Phi = r^{\eta+1}\left[c_1 \sin 2\pi(\eta+1) + c_2 \cos 2\pi(\eta+1) + c_3 \sin 2\pi(\eta-1)\right. \tag{2.57}$$
$$\left. + c_4 \cos 2\pi(\eta-1)\right]. \tag{2.58}$$

The quantities η, c_1, c_2, c_3 and c_4 are constants yet to be determined. The crack faces must be traction free, thus the boundary conditions for stress fields are:

$$\sigma_{\theta\theta}(0) = \sigma_{\theta\theta}(2\pi) = \sigma_{r\theta}(0) = \sigma_{r\theta}(2\pi) = 0. \tag{2.59}$$

From (2.58) the stress fields have to be computed:

$$\sigma_{rr} = \frac{1}{r^2}\frac{\partial^2\Phi}{\partial\theta^2} + \frac{1}{r}\frac{\partial\Phi}{\partial r} \tag{2.60}$$

$$\sigma_{\theta\theta} = \frac{\partial^2\Phi}{\partial r^2} \tag{2.61}$$

$$\sigma_{r\theta} = -\frac{1}{r}\frac{\partial^2\Phi}{\partial r\partial\theta} + \frac{1}{r^2}\frac{\partial\Phi}{\partial\theta}. \tag{2.62}$$

Inspection of (2.58) and (2.59) reveal that η must be an integer to satisfy the boundary conditions (2.59). There are infinitely many possibilities for η, thus the solution can be represented as a series expansion:

$$\sigma_{ij} = \frac{\Gamma_{ij}\left(-\frac{1}{2}\right)}{\sqrt{r}} + \sum_{m=0}^{\infty}\left(r^{m/2}\Gamma_{ij}(m)\right), \tag{2.63}$$

where Γ_{ij} is a function that depends on Φ and its derivatives. Detailed calculation of the higher order terms is usually omitted in literature, because the important property of representation (2.63) is the fact that the leading term depends on $1/\sqrt{r}$ and thus diverges to infinity for $r \to 0$, while the others have finite limiting values at the crack tip. There can always be found a zone close enough around the crack tip where the stress field is dominated by the leading term, and stresses are higher within that zone than anywhere else in the body. The stress fields near the crack tip are given explicitly as:

$$\sigma_{rr} = \frac{K_I}{\sqrt{2\pi r}}\left[\frac{5}{4}\cos\left(\frac{\theta}{2}\right) - \frac{1}{4}\cos\left(\frac{3\theta}{2}\right)\right]$$

$$\sigma_{\theta\theta} = \frac{K_I}{\sqrt{2\pi r}}\left[\frac{3}{4}\cos\left(\frac{\theta}{2}\right) + \frac{1}{4}\cos\left(\frac{3\theta}{2}\right)\right] \tag{2.64}$$

$$\sigma_{r\theta} = \frac{K_I}{\sqrt{2\pi r}}\left[\frac{1}{4}\cos\left(\frac{\theta}{2}\right) + \frac{1}{4}\cos\left(\frac{3\theta}{2}\right)\right].$$
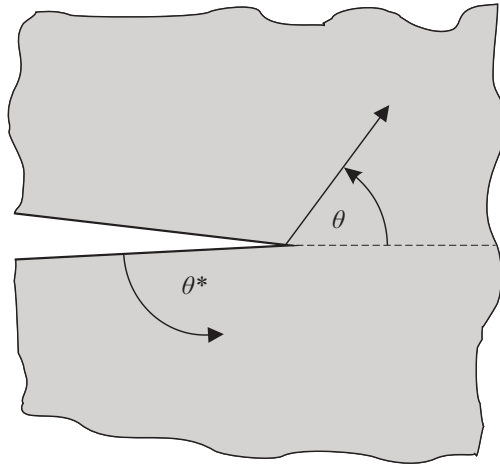
Fig. 2.1: Edge-crack configuration analyzed by Williams

The quantity K_I is the well known stress intensity factor, which is

$$K_I = \sigma\sqrt{\pi a} \tag{2.65}$$

for the present configuration.

2.4 Non-Local Continuum Theories

The classical theory of linear elasticity presented above rests on two intuitive assumptions, apart from Newtons Fundamental Laws: the idea of continuous mass density and the idea that all forces appearing are contact forces with zero range effect. Both assumptions are independent of each other [81]. There are situations where zero-range forces are not a good approximation of nature, e.g. on small scale elasticity where atomic lattice effects play a role in deformation processes, or in big stellar bodies where gravitational force is not only visible as external on the body but also acting between inner mass points of the body itself. Hooke's law (2.9) is local in the sense that local stresses in an infinitely small region are only dependent on strains within the same region. Constitutive laws in non-local continuum theories also depend on deformations in neighboring points.

The physical foundations for non-local theories have been laid out by Toupin in 1962 [144], who based his discussion on atomistic arguments. Early work on that topic has also been done by Mindlin [102, 103] and Green and Rivlin [58]. In 1968 Kröner [81] presented an integral theory for non-local elasticity. The three-dimensional, non-local elastic energy is reformulated as

$$E = \frac{1}{2}\sum_{\mathbf{x},\mathbf{x}'} \Phi_{ik}\left(\mathbf{r} - \mathbf{r}'\right)\left(u_i' - u_i\right)\left(u_k' - u_k\right). \tag{2.66}$$

The quantity $\Phi_{ik}\left(\mathbf{r} - \mathbf{r}'\right)$, with $\Phi_{ik} = \Phi_{ki}$ induces finite range effects and has to be derived from physical arguments (van-der-Waals forces, etc.). The stress tensor σ_{ij} as variational

derivative $\delta E / \delta \epsilon_{ij}$ of E reads

$$\sigma_{ij}(\mathbf{r}) = C_{ijkl}\epsilon_{kl} + \int_{\mathcal{D}} c_{ijkl} \left(\mathbf{r} - \mathbf{r}' \right) \, \mathrm{d}V. \qquad (2.67)$$

The two-point tensor $c_{ijkl} \left(\mathbf{r} - \mathbf{r}' \right)$ has to be calculated as the solution of a system of inhomogeneous, linear partial differential equations where the inhomogeneous parts depend on the Φ_{ik}.

Dillon [33] presented in 1970 a theory of plasticity that incorporates first order and second order strain gradients. His model accounts for inhomogeneous deformations at small scale. The small scale behavior influences the macroscopic behavior, thus thermodynamic considerations and concepts of linear elastic fracture mechanics can be included. It simulates dislocation interactions with non-nearest neighbors, thus coming to a non-local model at a macroscopic scale. Another, thermodynamically motivated constitutive theory for non-linear elasticity has been presented by Eringer in 1972 [43] in a widely respected article. The non-local elasticity models are of little relevance to the work presented here and thus are not discussed in more detail. Non-local approaches have later been applied to damage mechanics models for several reasons, and that is why this very brief overview is given.

2.5 Micromechanics and Homogenization

The theory presented in sec. 2.1 so far is based on the assumption of continuous and homogeneous distribution of matter, i.e. the properties relevant to the formulation, elastic parameters and mass density do not depend on the position within the body. These assumptions fail to hold in any realistic material on a small (atomistic) scale, but may approximate the situation at scales large compared to distances between atoms and molecules, as discussed previously. For the sake of clarity it is pointed out that the theory itself does not impede inhomogeneous material parameters, one simply may substitute the coordinate dependent expressions $\lambda(\mathbf{x})$ and $\mu(\mathbf{x})$ to (2.13), but the results presented from (2.18) to (2.28) are no longer valid in that case. One special case is encountered, when the mechanical properties are distributed heterogeneously on a length scale where the assumption of continuous mass distribution holds, and are observed as homogeneous at a scale still larger than the intermediate one. The general concept is illustrated in fig. 2.2. The whole theory collapses at atomistic level, but at the intermediate level it applies everywhere. It is further assumed that on a macroscopic level a formulation of a boundary value problem with homogeneous constants may be applied, and the solutions in stresses and strains represent the local fields at the microscale in an averaged manner. The constant parameters are called effective or apparent parameters, because they are observed and measured in experiments with macroscopic specimens. An obvious, necessary condition for such an approach is that the characteristic dimension of heterogeneities be much smaller than the dimensions of the body. This is called the concept of separable scales [78]. In addition it is assumed that the heterogeneous structure repeats periodically with period-length much smaller than the global scale. In [78] it is mentioned that in computational analysis the weaker assumption that the heterogeneities are periodic in the vicinity of the analyzed material point, and globally non-periodical behavior may be allowed. The scientific field concerned with the overall, homogenized representation of materials with actually non-homogeneous microstructure is
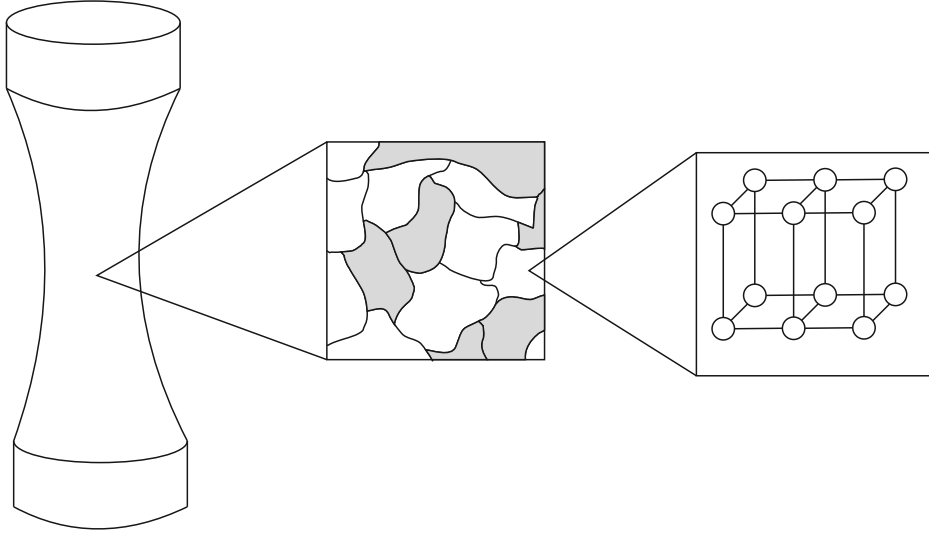
Fig. 2.2: Schematic visualization of the multiple scale concept

called Micromechanics [108]. The substitution of the non-homogeneous mechanical parameters with constant, averaged parameters is called Homogenization. Mathematically, this problem can be termed as finding a solution to partial differential equations with fast varying parameters and subjected to boundary conditions. Fortunately, in the case of linear elastic solids, estimates of the homogenized parameters can be found based on physical arguments rather than the exact solution of the underlying mathematical problem. In cases where non-linear behavior is assumed, numerical techniques usually have to be applied.

In linear elasticity the effective parameters are defined via the averaged Hooke's law [108]. When all the constituents behave linearly elastic, stresses and strain fields are averaged over the whole body:

$$\langle \boldsymbol{\epsilon} \rangle = \frac{1}{V_D} \int_{\mathcal{D}} \boldsymbol{\epsilon}(\mathbf{x}) \, d\mathbf{x} \tag{2.68}$$

and

$$\langle \boldsymbol{\sigma} \rangle = \frac{1}{V_D} \int_{\mathcal{D}} \boldsymbol{\sigma}(\mathbf{x}) \, d\mathbf{x}. \tag{2.69}$$

The effective stiffness tensor $\mathbf{C}_{\mathrm{eff}}$ is a linear mapping of the volume averaged strain onto the volume averaged stress:

$$\langle \boldsymbol{\sigma} \rangle = \mathbf{C}_{\mathrm{eff}} : \langle \boldsymbol{\sigma} \rangle. \tag{2.70}$$

The components of $\mathbf{C}_{\mathrm{eff}}$ are denoted with $C_{ijkl,\mathrm{eff}}$. The task of finding effective elastic parameters is reduced to calculating the averaged stress and strain fields. In most cases it is not possible to obtain exact results for them. Several attempts have been made to estimate them. Two simple estimates, the Voigt- and the Reuss-limit, have been identified as upper and lower bounds to the exact effective stiffness, respectively. This was done by Hill in 1963 [67]. The Voigt estimate is based on the assumption that the strain $\boldsymbol{\epsilon}$ is constant throughout the different phases, which means $\langle \boldsymbol{\epsilon} \rangle = \boldsymbol{\epsilon}$. The stress average can be computed

straight ahead:

$$\langle \boldsymbol{\sigma} \rangle = \sum_{r=1}^{n} c_r \mathbf{C}_r : \boldsymbol{\epsilon} \tag{2.71}$$

where the index r labels different phases, c_r are the volume fractions corresponding to different phases and $\mathbf{C}_r$ are the elastic stiffness tensors related to phases r, when there are n different phases present in the material. The Voigt estimate for effective elastic constants is [148]

$$\mathbf{C}_{\mathrm{V}} = \sum_{r=1}^{n} c_r \mathbf{C}_r. \tag{2.72}$$

The Reuss estimate approximates the stresses throughout the material as constant, and analogous analysis yields for the effective stiffness [124]:

$$\mathbf{C}_{\mathrm{R}} = \left(\sum_{r=1}^{n} c_r \mathbf{M}_r \right)^{-1} \tag{2.73}$$

where $\mathbf{M}_r = \mathbf{C}_r^{-1}$ is the inverse of the elastic stiffness tensor, called compliance tensor. When the material under investigation has a matrix-particulate microstructure, and the particulates have spherical or ellipsoidal shape, more precise estimates have been obtained by the use of Eshelby's solution, presented in sec. 2.3.1. In (2.54) the strains within a spherical or ellipsoidal inclusion is given in dependence on a far field strain $\boldsymbol{\epsilon}^0$. A new symbol $\mathbf{A}$ is introduced,

$$\mathbf{A} = \left[\mathbf{S} : \mathbf{M}_0 : (\mathbf{C}_1 - \mathbf{C}_0) + \mathbf{I} \right]^{-1}, \tag{2.74}$$

where $\mathbf{C}_0$ represents the elastic stiffness of the matrix, $\mathbf{M}_0 = \mathbf{C}_0^{-1}$ and $\mathbf{C}_1$ is the stiffness of the material in the inhomogeneity. The Eshelby estimate reads [108]:

$$\mathbf{C}_{\mathrm{eff,E}} = \mathbf{C}_0 + c_1 (\mathbf{C}_1 - \mathbf{C}_0) : \mathbf{A}_1. \tag{2.75}$$

The volume average of stress and strain is obtained by the use of the Eshelby property, the assumption that inclusions do not interact with each other (dilute dispersion assumption) and the Mori-Tanaka theorem, [139]. For details on the calculation see [108]. Exact results can be obtained for isotropic phases and spherical, ellipsoidal and polygonal inclusion shapes. Sevostianov et al. [130] found a closed form formulation for spherical inclusions and transversely-isotropic phases. If the volume fraction of the particles is too high to maintain the non-interaction assumption, a better estimate is obtained with the self-consistent or effective field method, proposed by Kröner [80] and by Budiansky [24]. A representative inhomogeneity is placed within a matrix that consists of the effective material. The underlying idea is that the inhomogeneity 'sees' the effective fields due to the presence of the other inhomogeneities. Analysis is carried out as in sec. 2.3.1 and analogously to (2.74) a result for the strain concentration tensor is found:

$$\mathbf{A}_{\mathrm{SC}} = \left[\mathbf{S}_{\mathrm{eff}} : \mathbf{M}_{\mathrm{eff}} : (\mathbf{C}_1 - \mathbf{C}_{\mathrm{eff}}) + \mathbf{I} \right]^{-1}. \tag{2.76}$$

This has to be substituted into (2.75). An implicit formula for $\mathbf{C}_{\mathrm{eff}}$ is encountered, and a solution has to be found via fixed point iteration. Since the Eshelby tensor $\mathbf{S}_{\mathrm{eff}}$ has to be calculated for the effective material, closed form solutions are available only for cases where the effective stiffness is isotropic or transversely-isotropic, e.g. not for inhomogeneities of

general ellipsoidal shape. The self consistent approach is therefore less flexible compared to the Eshelby method. In general cases the Eshelby tensor has to be calculated numerically, but it is rather difficult to achieve numerical convergence (for details see for example [53]). The Mori-Tanaka estimate is the third approach [104]:

$$\mathbf{C}_{\text{eff,MT}} = \mathbf{C}_0 + c_1 \left(\mathbf{C}_1 - \mathbf{C}_0 \right) \left[(1 - c_1)\mathbf{I} + c_1 \mathbf{A}. \right]^{-1} \tag{2.77}$$

$\mathbf{A}$ in (2.77) is the same as in (2.74). The Mori-Tanaka Method usually gives better results than (2.75) but does not pose the limitations of (2.76). Therefore, the Mori-Tanaka approach was chosen in this project when effective elastic constants obtained from numerical procedures needed to be checked. The two limits (2.72) and (2.73) are also used as a first control of the numerical results. For comprehensive discussion of these three theories see [108] or [110].

A generalization of the equivalent inclusion method used by Eshelby (see sec. 2.3.1 again) is the introduction of the polarization stress proposed by Hashin and Shtrikman [64]. This approach is applicable to composites with elastic heterogeneities of arbitrary shape and also to completely irregular microstructures. The numerical algorithm presented in [106] that was the basis for the algorithm developed for this work is based on this concept, which is the reason why it is discussed at this point. The problem is a body $\mathcal{D}$ with a heterogeneous elastic stiffness tensor $\mathbf{C}(\mathbf{x})$ subjected to a constant prescribed strain $\mathbf{E}$. A solution for the elastic fields $\boldsymbol{\sigma}(\mathbf{x})$ and $\boldsymbol{\epsilon}(\mathbf{x}) = \mathbf{E} + \boldsymbol{\epsilon}'(\mathbf{x})$ is looked for. For these two fields the equation of motion and Hooke's law must hold in every point $\mathbf{x}$:

$$\left. \begin{array}{l} \text{div}\boldsymbol{\sigma}(\mathbf{x}) = 0 \\ \boldsymbol{\sigma}(\mathbf{x}) = \mathbf{C}(\mathbf{x}) : \boldsymbol{\epsilon}(\mathbf{x}). \end{array} \right\} \tag{2.78}$$

But instead of analyzing the original problem, a problem with equivalent elastic fields is formulated: a homogeneous body $\bar{\mathcal{D}}$, called reference body, with elastic stiffness $\mathbf{C}_0$ with the same boundary conditions as $\mathcal{D}$ but in addition subjected to a body force field $\mathbf{f}(\mathbf{x})$. $\mathbf{f}(\mathbf{x})$ shall be chosen in such a way that the resulting stress field $\boldsymbol{\sigma}_0(\mathbf{x})$ in $\bar{\mathcal{D}}$ is identical to the stress field in $\mathcal{D}$:

$$\boldsymbol{\sigma}_0(\mathbf{x}) = \boldsymbol{\sigma}(\mathbf{x}) \qquad \forall \mathbf{x} \in \mathcal{D}. \tag{2.79}$$

The same is required to be true for the strain fields $\boldsymbol{\epsilon}$ and $\boldsymbol{\epsilon}_0$. The body $\bar{\mathcal{D}}$ may be isotropic with Lamé parameters λ_0 and μ_0, but the idea is not restricted to that choice. The stress polarization tensor $\boldsymbol{\tau}$ is introduced:

$$\boldsymbol{\tau}(\mathbf{x}) = (\mathbf{C}(\mathbf{x}) - \mathbf{C}_0) : \boldsymbol{\epsilon}(\mathbf{x}). \tag{2.80}$$

The stresses can be decomposed into two parts accordingly:

$$\boldsymbol{\sigma}(\mathbf{x}) = \mathbf{C}_0 : \boldsymbol{\epsilon}(\mathbf{x}) + \boldsymbol{\tau}(\mathbf{x}). \tag{2.81}$$

Substitution into (2.78) yields:

$$\text{div} \left(\mathbf{C}_0 : \boldsymbol{\epsilon}(\mathbf{x}) \right) + \text{div}\boldsymbol{\tau}(\mathbf{x}) = 0. \tag{2.82}$$

A body force is defined as

$$\mathbf{f}(\mathbf{x}) = \text{div}\boldsymbol{\tau}(\mathbf{x}) \tag{2.83}$$

and (2.82) is rewritten as

$$\left.\begin{array}{c} \text{div}\boldsymbol{\sigma}_0(\mathbf{x}) = -\mathbf{f} \\ \boldsymbol{\sigma}_0(\mathbf{x}) = \mathbf{C}_0 : \boldsymbol{\epsilon}(\mathbf{x}). \end{array}\right\} \tag{2.84}$$

These are the governing equations of the homogeneous body with stiffness $\mathbf{C}_0$ subjected to the body force field $\text{div}\boldsymbol{\tau}(\mathbf{x})$. According to (2.26) the solution in terms of displacement field can be written as

$$\mathbf{u}(\mathbf{x}) = \mathbf{E} - \int_{\mathcal{D}} \mathbf{G}_0(\mathbf{x} - \mathbf{y})\text{div}\boldsymbol{\tau}(\mathbf{y})\,\mathrm{d}\mathbf{y} \tag{2.85}$$

where $\mathbf{G}_0(\mathbf{x})$ is the Greens function of the homogeneous reference material (corresponding to λ_0 and μ_0 in the case of isotropic $\mathbf{C}_0$). Following the notation of Willis [154] (2.85) is rewritten in symbolic form:

$$\boldsymbol{\epsilon}(\mathbf{x}) = \mathbf{E} - \boldsymbol{\Gamma}_0(\mathbf{x}) * \boldsymbol{\tau}(\mathbf{x}) = \mathbf{E} - \boldsymbol{\Gamma}_0(\mathbf{x}) * (\mathbf{C}(\mathbf{x}) - \mathbf{C}_0) : \boldsymbol{\epsilon}. \tag{2.86}$$

The integral operator $\boldsymbol{\Gamma}_0$ has the dimension of a fourth order tensor. (2.86) represents an integral equation with $\boldsymbol{\epsilon}(\mathbf{x})$ as variable. The advantage about this approach is that the Green's function for a homogeneous isotropic material may be used rather than the Green's function of the heterogeneous material, which is not available in closed form for most micro-geometries. Nonetheless numerical techniques have to be employed to find a solution of (2.86). Kröner [82] suggest to expand (2.86) into a series, and calculate the truncated result. He gives a proof that the series expansion converges. Kröner also reports that (2.86) is an equation of the Lippmann-Schwinger kind which is well known from statistical quantum mechanics. This means all results and properties obtained for this equation can be adopted for (2.86). An expression for $\boldsymbol{\Gamma}_0$ that is used within this work is given in a later section.

Practically all cases of heterogeneous media involving non-linear behavior need to be investigated with numerical techniques [78]. The most prominent method used in continuum theories (continuum mechanics, heat conduction, electrical current) is the finite element method. The macroscopic body is idealized as homogeneous, and discretized with a finite element mesh. The solution of this global problem gives the macroscopic strains $\boldsymbol{\epsilon}_{\mathrm{M}}$ on the integration points, and they are imposed as boundary conditions to a representative volume element (RVE) that is a detailed model of the microstructure. A choice has to be made about the size of the representative volume element. It has to be large enough to include all the statistical features of the heterogeneities, to avoid for example anisotropic behavior because the RVE contains too few inhomogeneities of a certain shape. On the other hand the RVE must not be to big with respect to the macroscopic dimension of the body under consideration. These two limitations reflect the scale separating property mentioned above. When the boundary condition following from the global displacment field is applied an additional boundary value problem is obtained. This has to be solved, also with numerical techniques in most cases, and from the solution the average stress response $\langle\boldsymbol{\sigma}(\mathbf{x})\rangle$ to $\boldsymbol{\epsilon}_{\mathrm{M}}$ and the material tangent are calculated. The analyst is free in the choice of the method applied, but most common practice is the use of the Finite Element Method for the submodel as well. The terms Multiscale Finite Element Method or FE^2 have been coined for this procedure [78]. The macroscopic volume average of the variation of the internal work has to be equal to the variation of the local work at macroscale [68]:

$$\frac{1}{V_0}\int_{V_0} \boldsymbol{\sigma}(\mathbf{x}) : \delta\boldsymbol{\epsilon}(\mathbf{x})\,\mathrm{d}V_0 = \langle\boldsymbol{\sigma}(\mathbf{x})\rangle : \delta\langle\boldsymbol{\epsilon}\rangle \quad \forall\mathbf{x} \in V_0. \tag{2.87}$$

(2.87) is known as Hill-Mandel theorem [78]. This theorem is satisfied when the boundary conditions meet certain requirements. The applied strains have to be periodic and the applied traction has to be anti-periodic:

$$\boldsymbol{\epsilon}(\mathbf{x}^+) = \boldsymbol{\epsilon}(\mathbf{x}^+) \quad \text{and} \quad \mathbf{n}(\mathbf{x}^+) \cdot \boldsymbol{\sigma}(\mathbf{x}^+) = -\mathbf{n}(\mathbf{x}^-) \cdot \boldsymbol{\sigma}(\mathbf{x}^-). \tag{2.88}$$

The labeling of position vectors $\mathbf{x}^+$ and $\mathbf{x}^-$ indicates that they belong to opposite surfaces of the RVE. Apart from satisfying (2.87) these boundary conditions preserve the periodicity of the elastic fields as well as the geometry after deformation. To make sense of the multiple scale approach it is of course required that the boundary conditions are such that the macroscopic stresses and strains have to be incorporated, and the volume average of the strains has to be equal to $\boldsymbol{\epsilon}_\mathrm{M}$.

During this work the boundary value problem corresponding to the submodel at the integration points is not solved with the Finite Element Method but with an algorithm based on discrete Fourier transform.

2.6 Fracture and Damage Mechanics

In many engineering applications the dimensioning of members, either belonging to structures or machines, is carried out by stress analysis withing the framework of linear elasticity. Three dimensional stress states are converted into scalar equivalent stresses, which are compared to the maximum load capacity of the construction material. Exceeding the maximum load capacity would lead to immediate failure. In the beginning of the 20th century experience showed that in a huge number of failure incidents, many of them catastrophic events causing casualties and high costs, parts of a structure failed although the maximum loads in service had still been far below the maximum load capacity of the material. This issue appears especially in cases where service loads were time-dependent and repetitive. The explanation of these failures can be found by results as the one presented in section 2.3.2. In classical stress analysis a structure is considered to be a perfect continuum. This is an incorrect assumption, of course, since any real material shows heterogeneities at least when inspected on a microscopic level, showing pores, sharp crack and other discontinuities. Analyses as the one by Williams [153] revealed that (theoretically infinite) stresses exceed the stress levels observed macroscopically and thus have to be included in safety analysis. Of course it is undesirable and in most cases impossible to model the part with the entire microstructure. Rules have to be found to estimate the effects of flaws on the macroscopic behavior. That is essentially the motivation behind the theory of fracture mechanics.

Natural as well as artificially designed materials can be categorized according to their fracture behavior. Many materials, e.g. Glass, hardly can sustain even small deformation without fracturing immediately. Cracks appear without visible advanced notice and propagate at very high velocities. Such materials are called brittle. Contrary to that most metals show a different behavior at room temperature, called ductile behavior: High plastic deformation accompanies crack propagation. Ductile metals show higher resistance against crack growth than brittle materials since a big part of the energy is dissipated into plastic deformation. Both classes of material reveal their difference in classical tension tests. In figure 2.3 representative stress-displacement curves are shown to illustrate the difference. Whereas the curve of brittle materials is dominated by the linear branch that ends abruptly when failure
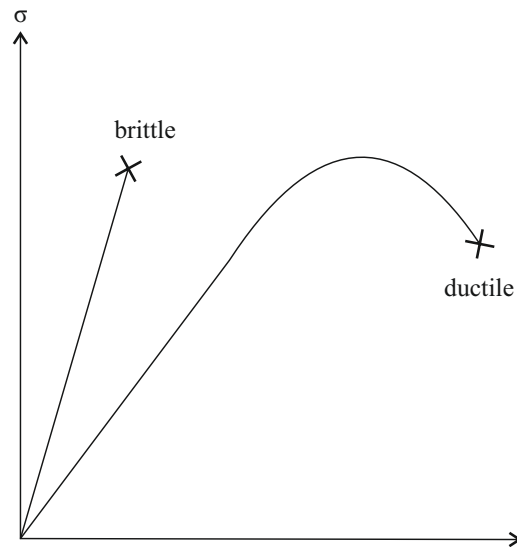
Fig. 2.3: Schematically drawn stress-displacement curves to illustrate different fracture behavior

occurs, the curve of ductile materials has a big non-linear branch that shows a peak stress after which the slope of the curve gets negative. This part is called strain-softening behavior in literature. For real materials no sharp border between brittle and ductile behavior can be drawn. Additionally, the behavior is often temperature dependent. Many metals that behave in a ductile manner at room temperature become brittle at a temperature far below zero. Another class of materials are called quasi-brittle: Little or no visible plastic deformation can be sustained, nevertheless a strong non-linear part of the stress-displacement curves is observed in tension test under appropriate conditions. A prominent example for such behavior is concrete. The algorithm formulated within this work is aimed at modeling this particular class of materials, thus a detailed review on experimental data and simulation techniques is given later in this section. To start with, the basic aspects of fracture mechanics are discussed here.

Stress analyses as the one presented in 2.3.2 can be performed for a variety of crack configurations. The stress singularity near the crack tip is considered to be the decisive phenomenon. This is called stress concentration effect of sharp cracks. Infinite stresses, as suggested by (2.63) cannot be sustained by any real material. However, in many cases it is assumed that the results obtained with the linear elastic theory are valid except for a small, finite zone around the crack tip. Within this zone the material behavior cannot be considered to be purely elastic. For metals, for example, the maximum stress in the material is bounded by the yield limit, and plastic deformation occurs in a zone near the crack tip. Crack propagation is governed by elastic stresses if this zone of plastic deformation is smaller than the zone where the stress field is dominated by the singular term in (2.63). Within this zone where the singular stress term is dominant, the stresses are proportional to K_I, the so-called stress intensity factor. In the literature on fracture mechanics three different modes of stress concentration at crack tips are distinguished, according to three linearly independent loading conditions for the cracked, infinite half plane in fig. 2.1: mode I refers to the loading situation discussed in sec. 2.3.2, mode II refers to in-plane shear and mode III to outer plane shear of the crack faces [7]. All three loading conditions lead to singular stress concentration at the crack tip, and all are proportional to stress intensity factors K_I, K_{II} or K_{III}, respectively, where the subscript denotes the fracture mode to which the factor belongs.

When a crack as the one depicted in fig. 2.1 propagates into the material, new surfaces are formed, or in different words, the existing surfaces are extended. From a thermodynamical point of view this is a change of state, and energy is consumed within the process. On the other hand, the elastic stress and strain fields within the material are changed as the zone dominated by the stress singularity moves with the propagating crack tip. This means that the amount of elastic energy stored in the deformed material and the potential energy supplied by the external forces alters. The first law of thermodynamics now states that there is always a net decrease in energy when a body changes from a non-equilibrium state to an equilibrium state. Thus new crack surfaces can only be formed when the net surface energy consumed in the process is less than the elastic energy that is released. If Π denotes the elastic potential and A the total amount of crack surfaces, than the energy release rate $\mathcal{G}$ is defined as (see Irwin, [72]):

$$\mathcal{G} = -\frac{\mathrm{d}\,\Pi}{\mathrm{d}\,A}. \tag{2.89}$$

Another term sometimes used for G is crack driving force, since it is expressed as derivative of a potential. The net change in total energy $\mathcal{E}$ during a crack propagation process is:

$$\frac{\mathrm{d}\,\mathcal{E}}{\mathrm{d}\,A} = \frac{\mathrm{d}\,\mathcal{W}_s}{\mathrm{d}\,A} - \mathcal{G}, \tag{2.90}$$

where $\mathcal{W}_s$ is the work needed to create new surfaces. Crack propagation can only take place when $\frac{\mathrm{d}\mathcal{E}}{\mathrm{d}A}$ is negative (net decrease in energy), or in other words, when $\mathcal{G}$ exceeds a certain critical value, e.g. denoted with $\mathcal{G}_{cr}$. It is not necessary to give absolute values for $\mathcal{W}_s$, the important consequence of these considerations is the existence of a critical elastic energy release rate. This makes this concept accessible to experimental verification, since $\mathcal{G}$ can be determined exactly for simple configurations as in fig. 2.1. It was already mentioned that the stress fields, and consequently also the elastic energy, are proportional to the stress intensity factor, which means that $\mathcal{G}$ is uniquely related to the stress intensity factor K_I, K_{II} or K_{III}, or a combination of them.

Griffith [59] had developed a similar yet less general approach earlier than Irwin. He related the energetic argument to the applied stress, and gave a stress level critical for the onset of crack propagation in the example presented in sec. 2.3.2:

$$\sigma_f = \left(\frac{2E\gamma_s}{\pi a}\right), \tag{2.91}$$

where E denotes the Young's modulus of elasticity, a is the crack length and γ_s is the specific surface energy of the material. The unique relation of the critical state to the applied stress σ is completely analogues to the unique relation between $\mathcal{G}$ and K. In the literature the critical energy release rate is sometimes replaced by the material resistance to crack propagation, R:

$$\mathcal{G} = R, \tag{2.92}$$

$$\mathcal{G} = \mathcal{G}(\alpha). \tag{2.93}$$

For simple configurations as the one presented in fig. 2.4 an explicit formula can be given for $\mathcal{G}(\alpha)$. Stress analysis for 2D-problems shows that $\mathcal{G}(\alpha)$ has a unique maximum for a given α' (which depends on the configuration, obviously), [7]. It is assumed that the crack extends into direction α' since the decrease in total energy becomes maximal in that
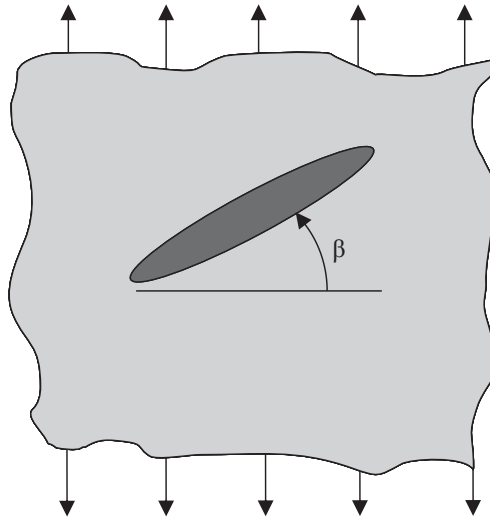
Fig. 2.4: Mixed-mode crack problem

case [42]. In homogeneous materials cracks tend to propagate into the direction normal to the first principal axis of stress [7].

The concepts and analysis presented are entirely based on the theory of linear elasticity. Hence, their applicability is restricted to brittle materials, since these show little or next to no plastic deformation before material failure occurs. Critical stresses for glass specimens can be approximated very good by the K_I-criterion, but in the case of fracture of metals they cannot. In order to explain these differences care has to be taken when the stress field (2.63) is interpreted. Infinite stresses cannot be sustained by any material. The singularity is the result of the sharp crack tip assumed in the initial configuration. This can only be an approximation of real world problems: at atomistic length scales no sharp edge would be observed. For a better approximation of the real world problem the sharp line crack may be replaced by an elliptical hole with one axis much bigger than the other one, see fig. 2.5a. A closed form solution is also available for this case, e.g. given in [141], and the resulting stress and strain fields do not show singular behavior in this case. In ductile materials the stress is limited by the yield stress σ_y. Plastic flow will occur around the crack tip instead of infinite stresses. A first approximation of the region where plastic deformation takes place is simply obtained by calculating the von-Mises equivalent stresses from (2.64) and setting it equal to the yield stress:

$$\sigma_{\text{eq}}(r, \theta) = \sigma_Y. \tag{2.94}$$

Through (2.94) an approximation of the boundary of the plastic zone is given in implicit form. Within the plastic zone the stress is assumed to be everywhere equal to the yield stress σ_Y. This can only be an approximation because the obtained stress field is not in equilibrium. But nonetheless this approach is widely used in the literature to estimate the extension of the plastic zone around the crack tip. Although this problem is obviously not a purely linear elastic, analyses like the one in sec. 2.3.2 can still be applied under certain conditions. This comes from the fact that the single parameter K_I (or K_{II}, K_{III}, respectively) is sufficient to characterize the situation around the crack tip. It was mentioned in sec. 2.3.2 that a (circular) zone can be determined where the singular term in (2.64) dominates the whole stress field. As long as the plastic zone is considerably smaller than the singular-dominated zone, the situation within the latter one will be determined by the stress intensity
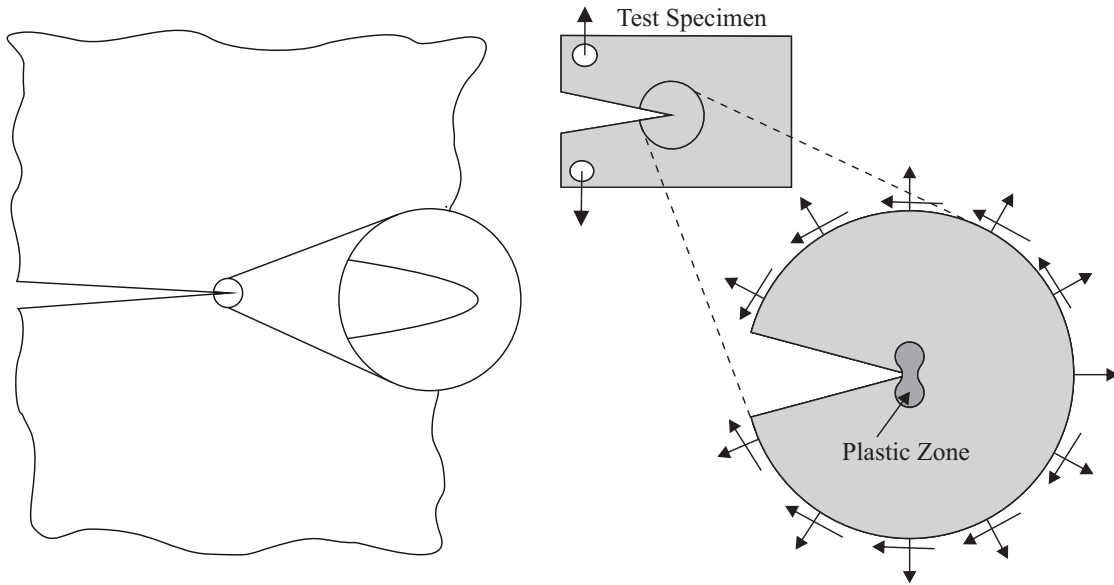
Fig. 2.5: Visualization of curved surfaces at the end of a crack (left side) and of plastic zone inside singularity dominated zone (right side)

factor, even if plastic deformation occurs locally. The stress near the crack tip will not be as in (2.64), but that is not of primary importance. This is the reason why the estimate in (2.94) is widely used. The designer usually is not interested in the local fields around the cracks but rather in properties that can be observed macroscopically. When a crack propagates into a ductile material, it is not only the formation of new surfaces that consumes energy, but also the additional plastic yield the happens around the relocated crack tip. Therefore material resistance to crack propagation is higher at temperatures where ductile behavior prevails than at lower temperatures, when the material behavior becomes brittle. Fracture resistance may increase with growing cracks.

In case of initiated crack propagation, an important question is whether the crack length will only increase a little bit, or will increase ever more once it was set in motion, and eventually lead to failure of the part. The latter situation is referred to as instable crack growth while the first one is labeled stable crack growth. Whether or not crack growth is stable depends on the evolution of fracture resistance and energy release rate. Their dependence on crack length can expressed via the derivatives

$$\frac{\mathrm{d}\mathcal{G}}{\mathrm{d}A} \quad \text{and} \quad \frac{\mathrm{d}R}{\mathrm{d}A}, \tag{2.95}$$

where A is the crack surface. In the case that crack propagation just onsets because $\mathcal{G} = R$ and

$$\frac{\mathrm{d}\mathcal{G}}{\mathrm{d}A} \leq \frac{\mathrm{d}R}{\mathrm{d}A}, \tag{2.96}$$

crack growth is stable because after A increased the energy release rate will be smaller than R. Contrary, if

$$\frac{\mathrm{d}\mathcal{G}}{\mathrm{d}A} > \frac{\mathrm{d}R}{\mathrm{d}A}, \tag{2.97}$$

energy release rate will ever be higher than the fracture resistance of the material causing the crack to further grow until the specimen or machine part fails completely. The evolution

of the relationship between $\mathcal{G}$ and R depends on the geometrical configuration, material properties and loading conditions. In rupture tests with the same material, it is easier to produce stable crack growth in displacement controlled tests than in load controlled tests.

In some materials, e.g. in many structural steels [7], the plastic zone around the crack tip is to big to adequately characterize the behavior by the stress intensity factors. The theory of elastic-plastic fracture mechanics has been developed to understand even such materials. Two additional parameters were introduced to characterize the situation around the crack tip: the crack-opening displacement (CTOD) and the J-integral. The crack-opening displacement δ was suggested by Wells in 1961 [152] as parameter, after he had observed that many steels were to tough to be investigated with LEFM. He observed that the crack surfaces had moved apart before the crack started propagating. Due to high plastic deformation in the vicinity of the crack tip, the former sharp crack gets blunted during the process, see fig. 2.6 for reference. For small scale yielding of an edge cracked plate, the CTOD can be related to the stress intensity factor,

$$\delta = \frac{4}{\pi} \frac{K_\mathrm{I}^2}{\sigma_\mathrm{Y} E},$$
(2.98)

and (consequently) to the energy release rate,

$$\delta = \frac{4}{\pi} \frac{\mathcal{G}}{\sigma_Y},$$
(2.99)

see [7]. Another parameter frequently used in elastic-plastic fracture mechanics is the J-integral. It was introduced by Rice in 1966 [125]. He idealized elasto-plastic materials as non-linear elastic materials. This makes sense because the general loading curve of both materials look the same if the load is increased monotonically (no unloading). The integral

$$J = \int_\Gamma \left(w \, \mathrm{d}y - t_i \frac{\partial u_i}{\partial x} \, \mathrm{d}s \right)$$
(2.100)

along a counterclockwise path Γ around the crack tip, form one crack face to the other, is path-independent. In (2.100) t_i is a component of the traction vector and w is the strain energy density:

$$w = \int_0^{\epsilon_{ij}} \sigma_{ij} \, \mathrm{d}\epsilon_{ij}.$$
(2.101)

J is related to the energy release rate:

$$J = -\frac{\mathrm{d}\,\Pi}{\mathrm{d}\,A}.$$
(2.102)

But care has to be taken with this interpretation, since it is not entirely the same as in (2.89), because in non-linear materials part of the energy is not released from the body but consumed in inelastic deformations. The J-integral was successfully applied to characterize fracture in metals. Explicit relations between J, geometry and loading configuration are usually not even available for simple cases, due to the non-linear nature of the concept. It was to be either calculated numerically or measured in experiment. Both, J and CTOD can be used as nearly size-independent parameters in situations involving cracks. It has been shown that a relationship exists between both [7].
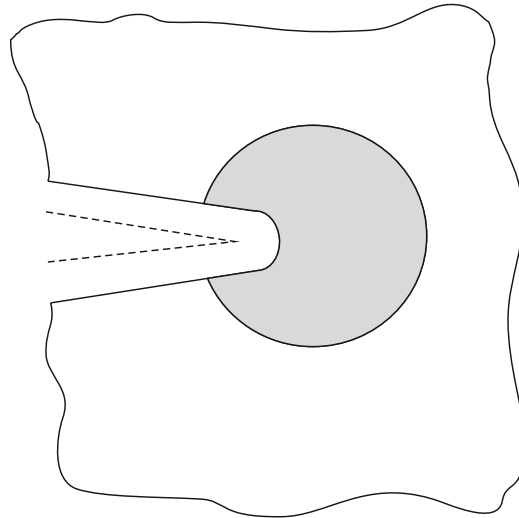
Fig. 2.6: Crack tip gets blunted during deformation

Until now a clear distinction between materials that behave in a brittle manner and materials referred to as ductile. Different concepts have been presented for both cases, though it has already been mentioned that the boundary between both classes cannot be drawn exactly. There is one prominent example where this distinction proofs very difficult, and that is concrete. At first glance concrete is observed as brittle material that shows no plastic deformation of any significant order before rupture. But already in 1968 it was shown by Evans that this was not the whole truth [45]. He performed unidirectional tension tests on concrete and showed that under certain circumstances elasto-plastic stress-strain curves are possible for concrete. However, it is not easy to obtain these in experiment. Evans reports that it is important that the main crack initiates within the area covered by the strain gauge. Furthermore, care has to be taken to avoid unstable crack growth at peak load. In a 1970 field study Popovics [122] gave a review over the available data about behavior of concrete in tension tests. He concluded that a typical stress-strain relationship starts with a linear section up to around 30% of the maximum load. He related the curved nature before the stress-peak to progressive microcrack propagation within the specimen. After that, a gradual deviation from linear behavior is observed, leading to a stress peak or critical load. This differs clearly from the standard model of brittle materials established previously (see fig. 2.3, and working satisfactorily for many of them, e.g. glass. Following peak stress the curve enters the descending part. A dependence of the curvature on aggregate size was identified in [122]. The author provides examples for empirical formulas to approximate the σ-δ-curve (δ being the CTDO) through curve fitting, and claimed that CTOD is a better parameter than K_I to characterize fracture of concrete. Remember that the CTOD had been introduced to analyse elasto-plastic materials. In order to describe this kind of fracture behavior the term *quasi-brittle* material has been coined. Popovics gave several examples for the standard tension test behavior, but also formulas adapted to special situations like flexural bending, concentric compression, etc.. The natural behavior of concrete under tension remained a topic for discussion for a long time. In 1985 Gopalaratnam [57] still reports on contradictory results obtained from tension tests found in the literature on the subject. He again points out that concrete shows post-crack resistance (contrary to ideal brittle materials) in tension tests, but this is often hidden by sudden failure due to inappropriate experimental setup. He performed tensile tests on his own and ascribed post-peak behavior of concrete to discontinuities on sub-microscopic level, e.g. bridging of cracked surfaces by aggre-

gates. In 1986 van Mier [147] examined the behavior of concrete subjected to multiaxial loading. He used hydraulic actors in a self-designed testing maching for that purpose. His main objective was to answer the question whether the strain-softening branch is a material property or rather a structure dependent characteristic. Although he could not find a clear answer, he stated that his results indicated the latter one. This is an important question to be answered before formulating numerical models. The same question was addressed by Ansari in 1987 [8], who observed crack propagation and crack opening displacements in tension tests by laser speckle interferometry. He detected an average crack opening width of 24 ± 2 microns as critical crack width (i.e., the crack width related to peak stress). Although he himself mentioned objections about the absolute number he emphasizes the fact that there *is* a determined crack width. An important observation by Ansari was the fact that strain localizes within a small band with an average width of 6 mm. Following Ansaris argument this width should be regarded as a material property. The observed strains were about two orders of magnitude higher within this band than outside. Foote [50] supported Popovics claim in 1986 that the relationship between load stress and crack opening displacement δ (the σ-δ curve) is the decisive property. He further posed the assumption that the σ-δ curve of a single crack analysed by means of linear elastic fracture mechanics is the most appropriate in case of concrete. Based on these arguments he derives a formula to calculate the crack resistance curve within linear elastic fracture mechanics theory. He applied his formula to the simple example of a double cantilever beam with good results. This idea was developed further by Li in 1987 [91] who used the J-integral to investigate stress-strain relationships analytically. Therefore he gave a formulation of the J-integral in terms of the crack opening displacement:

$$J(\delta) = \int\limits_0^S \sigma(\delta) \, \mathrm{d}\delta. \tag{2.103}$$

According to Li, standard K_I tests are inadequate for quasi-brittle materials due to the process zone being large in comparison with specimen size.

Parallel to experimental investigation of quasi-brittle materials in the 70ies and 80ies effort was spent to develop appropriate theoretical methods since classical models for brittle materials had proven to be inexact. When brittle materials like glass fail, a crack originates from a small zone where a network of microcracks appeared and propagates through the specimen. In contrast, quasi-brittle materials show an evolving network of microcracks usually confined to a small region or band, see [8] again. Macroscopically, a small region, usually a band, is observed where the elastic constants of the material are degraded. This follows e.g. from high strains in a small band observed by Ansari. Only during final rupture of a specimen a macrocrack occurs, possibly due to microscopical flaws forming together a bigger crack that propagates through the material, usually along the zones of prior degradation. It is not possible to model all microcracks individually when simulation of structural parts is needed. Instead, a continuum damage model may be used that simulates the local softening of the elastic behavior. Damage is treated as a smeared quantity similar to mass density. The field treating such theories is called damage mechanics in order to distinguish it from fracture mechanics, where single cracks are considered.

An early damage theory formulated especially for concrete but also for other quasi-brittle materials is the crack band model by Bazant [16, 19]. This model was developed analysis by the finite element method in mind. Fracture is modeled as a smeared, band like region across which microcracking occurs that affects material properties. This is modeled with a factor

that lowers elastic parameters element wise, thereby simulating strain-softening behavior. Each component from the stiffness tensor may be assigned an individual factor to model damage induced anisotropy. The crack band is the region of damage elements aligned in succession to each other. If propagation of the crack band is related to a strength criterion, the results are not objective. This is because any load can be made critical by choosing an element size small enough that the stress at the crack tip exceeds the limit [16]. Bazant proposed two different concepts to circumvent this problem. The first idea is to calculate the energy release rate for crack band extension calculated from strain-energy change and use this as a criterion. Second, the stress intensity factor can be determined from the stress in the element just ahead of the crack band front, and via relation to the element size determine an equivalent strength. In later publications on the topic Bazant preferred the energy criterion [17, 19].

In 1985 Rots presented a similar approach that he labeled smeared crack model [127]. His starting point is the decomposition of the strain field increments during increasing load into concrete strain increments and crack strain increments (resulting from displacement of the crack faces):

$$\Delta\boldsymbol{\epsilon} = \Delta\boldsymbol{\epsilon}^{\mathrm{conc}} + \Delta\boldsymbol{\epsilon}^{\mathrm{crack}}. \tag{2.104}$$

This allows for a more detailed treatment of the constitutive behavior, and the model can be enhanced with more complicated non-linear theories. Different crack modes may be combined in the crack strain to incorporate more detailed knowledge from fracture mechanics that is taken account for in the crack band model by Bazant [127]. In contrast to the crack band model no network of microcracks is considered but a single crack, however its softening influence is assumed to reach a small, finite zone around the crack, thus making the crack appear as 'smeared'.

Another possibility to model fracture of quasi-brittle materials is the crack layer theory proposed by Chudnovsky in [27], developed roughly at the same time as the crack band theory. The crack layer model also assumes a finite region around a single crack where microcracks originate. A further assumption is that the width of the crack layer depends on the J-integral as well as two other, path-independent integrals sometimes used in fracture mechanics [14]. The theory has been further elaborated by its originator, with results e.g. published in [28, 29].

These models are rather adapted to special situations and need to be configured for each discretization individually, e.g. via the element size. The most general and probably the most widely used approach is the introduction of a simple damage parameter as additional field variable. This is discussed by Chaboche, [26], and the idea was first introduced in 1968 by Rabotnov to model creep softening of metals at high temperatures [123].

Simo (see [132] and [131]) wrote two review articles about standard damage parameter models. Generally two approaches are possible: the effective stress concept or the effective strain concept. The basic idea in continuum damage models is to account for the progressive degradation experienced by mechanical properties of materials prior to initiation of macrocracks. For example, the local stress could be considered to be altered compared to stress in an undamaged solid by local flaws (e.g. cavities), because they cause the material to show a different elastic response to deformation. An effective stress is defined:

$$\boldsymbol{\sigma}_{\mathrm{eff}} = \mathbf{D}^{-1} : \boldsymbol{\sigma}. \tag{2.105}$$

In this equation $\boldsymbol{\sigma}$ is the stress in the undamaged material and $\boldsymbol{\sigma}_{\text{eff}}$ is the effective stress. $\mathbf{D}$ is a tensorial damage quantity. In the special case of isotropic damage the operator reads

$$\mathbf{D} = (1 - d)\mathbf{I}, \tag{2.106}$$

where d is a scalar valued damage variable describing the actual state of damage. Substituting (2.106) into (2.105) yields for the effective stress:

$$\boldsymbol{\sigma}_{\text{eff}} = \frac{1}{1 - d}\boldsymbol{\sigma}. \tag{2.107}$$

Thus for isotropic damage the tensorial description in (2.105) can be neglected, but if anisotropic effects of damage are important, the more general, tensor-based approach has to be used. The expression in (2.107) allows for a physical interpretation of d as the ratio of damage surface area over total surface area in an arbitrary cut through the body. This is made clear for a cylindrical body subjected to axial load, as illustrated in fig. 2.7. Normal traction on a cutting plane far from the ends of the cylinder can be assumed to be constant over the cross-section. The cross-section area of the undamaged cylinder is A, and thus

$$\sigma = \frac{F}{A}. \tag{2.108}$$

If flaws, e.g. pores or cracks, are present within the cylinder, they reduce the cross-sectional area if the plane of observation cuts through one or more of them. The reduced area is denoted with A_d, and $A_d < A$, of course. If stresses are still approximated as constant:

$$\sigma_d = \frac{F}{A_d} \tag{2.109}$$

and it follows that $\sigma_d > \sigma$. The same external load F may cause the damaged cylinder to fail while the undamaged is still able to sustain the induced stresses. This is a very simple analogue to the stress concentration effect discussed on page 23 for sharp cracks. Alternatively to the effective stress concept an effective strain could be defined also:

$$\boldsymbol{\epsilon}_{\text{eff}} = \mathbf{D} : \boldsymbol{\epsilon}, \tag{2.110}$$

and for isotropic damage:

$$\boldsymbol{\epsilon}_{\text{eff}} = (1 - d)\boldsymbol{\epsilon}. \tag{2.111}$$

The physical interpretation is analogue to the previous one: When subjected to a constant stress field, the damaged material locally deforms more than the undamaged solid would do, because local stresses are higher and induce higher deformation. Thus the choice is whether to consider locally reduced load bearing capacity or to study locally reduced stiffness. Hooke's law for the effective stress concept reads

$$\boldsymbol{\epsilon} = \mathbf{S} : \boldsymbol{\sigma}_{\text{eff}} = \left(\mathbf{S} : \mathbf{D}^{-1}\right) : \boldsymbol{\sigma} \tag{2.112}$$

and for the effective strain concept:

$$\boldsymbol{\sigma} = \mathbf{C} : \boldsymbol{\epsilon}_{\text{eff}} = (\mathbf{C} : \mathbf{D}) : \boldsymbol{\epsilon}. \tag{2.113}$$

Both concepts can be seen as equivalent, since the effect of both are altered elastic constants. However, if a model should be formulated based on physical assumption one or another approach may prove more convenient than its counterpart.
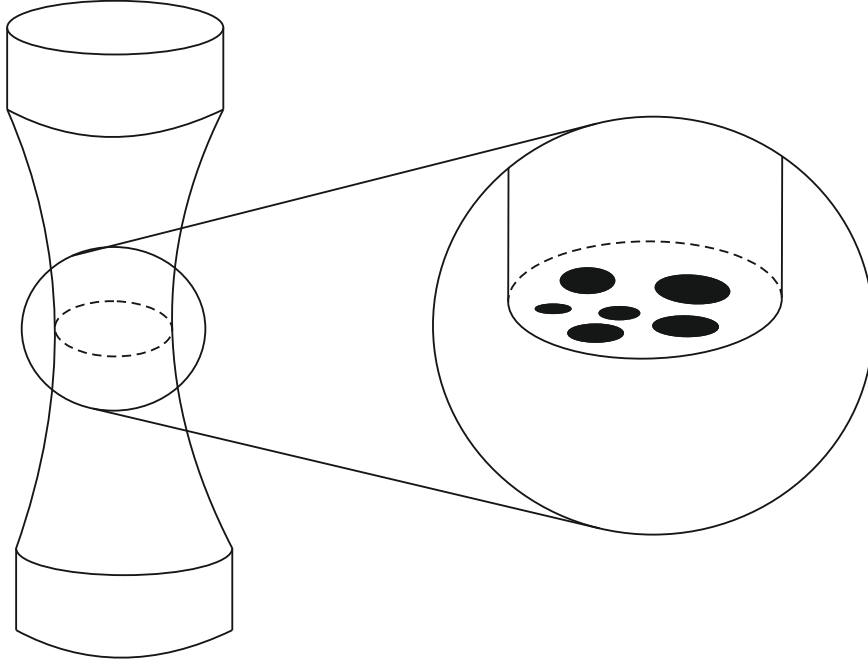
Fig. 2.7: illustration of effective stress concept

Since an isotropic (scalar valued) damage model has been formulated for this project the notion of a tensorial quantity $\mathbf{D}$ is omitted from now on. The only parameter related to damage is d. From (2.107) or (2.111) it is clear that an undamaged state of an elastic material $\mathbf{C}$ is associated with $d = 0$. When a body is loaded, damage initiates when the stresses locally exceed a critical value. This process comes along with the creation of pores, cracks or generally with a change of configuration that affects the effective elastic behavior. Energy is dissipated during this process, very much as in the case of a propagating crack. In damage mechanics the dissipative energy can be seen as more general and not restricted to the creation of new surfaces or plastic flow [88].

As in the case of a propagating sharp crack, stresses and strain fields vary when damage evolves in a loaded structure. So does the specific elastic deformation energy, called ψ_0:

$$\psi_0 = \frac{1}{2}\boldsymbol{\epsilon} : \mathbf{C} : \boldsymbol{\epsilon}. \tag{2.114}$$

If ψ_0 is referred to as a function dependent on d, the change in elastic energy may formally be written:

$$Y = -\frac{\mathrm{d}\psi_0(d)}{\mathrm{d}d}. \tag{2.115}$$

The analogy to $\mathcal{G}$ from fracture mechanics is obvious, and Y accordingly is named damage energy release rate [99]. The negative sign is a matter of definition and owed to the fact that the change in elastic energy has to be negative (and thus $Y > 0$) when damage evolves. If temperature effects and other irreversible processes are omitted from analysis the free energy potential is

$$\psi = \psi_0 + r\left|\dot{d}\right|, \tag{2.116}$$

see [99] or [88]. The quantity $\dot{d}$ is the damage evolution rate, but the dot-symbol must not be confused with a time derivative. The global thermodynamic potential [55] is written

$$\Pi(\mathbf{u}, d) = \int_{\mathcal{D}} \psi_0 + r \left| \dot{d} \right| \, \mathrm{d}V + \int_{\mathcal{D}} \mathbf{u} \cdot (\rho \mathbf{f}) \, \mathrm{d}V - \int_{\partial \mathcal{D}} \mathbf{u} \cdot \mathbf{t} \, \mathrm{d}A. \qquad (2.117)$$

This is the same as 2.16 only that the term $\int_{\mathcal{D}} r \left| \dot{d} \right| \, \mathrm{d}V$ has been added to account for dissipative effects. The solution $\tilde{d}$ and $\tilde{\mathbf{u}}$ for a given boundary value problem minimize (3.1) with respect to all admissible fields d with $\forall \, \mathbf{x} \in \mathcal{D} : d \geq 0$ and $\mathbf{u}$, [55, 155].

The approach in (2.116) appears to be very natural. However, it has a serious drawback in numerical applications. The results obtained show a strong dependency on the analysts choice of discretization. The simulated damaged zone will always be as wide as the distance between two sampling points, e.g. nodes in Finite Element Analyses or others. Apart from the implications this has when the results should be interpreted at a microscale-level, this also affects macroscopic behavior of a model. Peak stress, pre- and post-peak slope of the stress strain relationship vary with changing mesh resolution. Bazant pointed out in [14] that homogeneous continuum models with strain-softening behavior in a single location show an instability at the peak of the $\sigma - \epsilon$-curve, thus such a material cannot be realized in simulation. The existence of strain softening in a negligible portion of a body is an incorrect assumption. In Finite Element Analysis this instability will be disguised by the chosen discretization, since single elements with a finite length will decrease their stiffness and results can be obtained. But there are multiple solutions possible and apart from the difficulty of deciding which solution is the appropriate one, the whole instability may remain undetected by the analyst [14]. Localized strain softening behavior in general implies a loss a ellipticity of the governing equations, thus causing the instability at the peak [117]. Thus evolution equations should be non-local to avoid these problems. In [119] different concept of non-local models are compared to each other.

Some of the damage models described on page 30 can be adapted to avoid mesh dependency, but this increases computational complexity considerably. This was criticized by Pijaudier-Cabot [121], and he suggested a model where the damage evolution does not depend on the local elastic energy ψ_0 but on the average of ψ_0 over a representative volume element V_r centered around the point subject to inspection:

$$\langle \psi \rangle = \frac{1}{V_r} \int_{V_r} \psi \, \mathrm{d}V. \qquad (2.118)$$

This is a combination of damage mechanics with nonlocal continuum models, that had been developed earlier and are briefly presented in sec. 2.4. Pijaudier-Cabot mentioned the possibility to introduce a weight-function but does not yet apply this idea. This was done by later authors, for example Jirasek in [73], who compared different approaches of non-local continuum models. They all are based on the definition of a weight function $\alpha(\mathbf{x} - \mathbf{y})$ that determines the range of nonlocal effects. Different choices are possible, however Jirasek advocated use of the expression

$$\alpha(\mathbf{x} - \mathbf{y}) = \exp\left(-\frac{||\mathbf{x} - \mathbf{y}||^2}{2l^2}\right), \qquad (2.119)$$

where l is a parameter that has to be identified from experiments. In constitutive equations

a weighted volume average of the elastic energy is used :

$$\langle\psi_0\rangle = \int\limits_{V_r} \alpha(\mathbf{x} - \mathbf{y})\psi_0(\mathbf{y})\,\mathrm{d}\mathbf{y}. \tag{2.120}$$

Other quantities, e.g. averaged strain gradients, might be used as well.

As a last example for non-local damage models a formulation proposed by Peerlings [117, 118] is given here. The weighted volume average of the von-Mises equivalent strain

$$\langle\epsilon_{\mathrm{eq}}\rangle(\mathbf{x}) = \int\limits_{V_r} \alpha(\mathbf{x} - \mathbf{y})\epsilon_{\mathrm{eq}}(\mathbf{y})\,\mathrm{d}V \tag{2.121}$$

is approximated by a differential equation:

$$\langle\epsilon_{\mathrm{eq}}\rangle - c\Delta\langle\epsilon_{\mathrm{eq}}\rangle = \epsilon_{\mathrm{eq}}. \tag{2.122}$$

The so called natural boundary condition is applied:

$$\nabla\langle\epsilon_{\mathrm{eq}}\rangle\cdot\mathbf{n} = 0. \tag{2.123}$$

The effective stress concept (2.105) is used and a rather complex evolution equation is given for d:

$$d(\kappa) = 1 - \frac{\kappa_0}{\kappa}\left((1 - \alpha) + \alpha\exp\left[-\beta(\kappa - \kappa_0)\right]\right). \tag{2.124}$$

The parameters α and β have to be determined to fit experiments and κ is called historical variable in the publication, and defined by the Kuhn-Tucker relations:

$$\dot{\kappa} \geq 0,\ \langle\epsilon_{\mathrm{eq}}\rangle - \kappa \leq 0,\ \dot{\kappa}\left(\langle\epsilon_{\mathrm{eq}}\rangle - \kappa\right) = 0. \tag{2.125}$$

A mesh study is provided in [117] to demonstrate mesh objectivity, and a four point bending test is modeled as an example of application.

The theory of fracture mechanics is well suited for the analysis of propagation of existing cracks, but cannot predict the origination of initial defects in an otherwise homogeneous continuum. Damage mechanics in turn model the initial degradation of material points, as well as further propagation of the damaged zone. Mazars [99] reported in 1996 on theoretical considerations about the transition from fracture mechanics to damage mechanics and vice versa. This may be useful in cases where data from fracture tests, e.g. three-point bending tests, shall be used for large scale simulation, where it is desirable to employ a damage mechanics model. The connection between both formulations is possible via the conditions for propagation. As discussed above, in both theories propagation is related to an energetic quantity: the energy release rate $\mathcal{G}$ in fracture mechanics, see (2.89), and the damage energy release rate Y, (2.115). If both theories are needed to produce equivalent results for a certain configuration, the total energy release per time unit associated with crack or damage propagation should be equal. It follows that

$$\int\limits_{\mathcal{D}} -Y\dot{d} = -\mathcal{G}\dot{A}. \tag{2.126}$$

Mazars [99] gives further details on the efficient estimation of the corresponding properties.

One characteristic phenomenon in tests where material resistance against fracture (or damage) is investigated is the dependence of the results on the specimen size, called size effect. Size effects are known from many physical disciplines, e.g. turbulent flow in [60, 133]. In tests it is generally observed that bigger specimens show less resistance against fracture, and this is especially true for quasi-brittle materials like concrete [15, 20]. There two main origins of this effect. One is caused by the increased probability of bigger specimens to contain cracks of critical length that start early to propagate and reach a state of instable growth. This is called statistical size effect [18]. The other origin lies in the ratio of characteristic dimensions. The rupture strength of brittle materials, where LEFM applies, depends on the ratio of a crack to specimen size. Scaling laws that translate critical quantities belonging to one specimen size into others are needed. In some cases, where a theory includes size effects, formulas can be derived in closed form. This is true for example for LEFM, and the corresponding scaling law is [7, 15]:

$$\bar{\sigma}_f = \frac{\sigma_f}{\sqrt{\text{size}}}. \tag{2.127}$$

Generally, scaling laws are of empirical nature. For quasi-brittle materials an asymptotic expansion is usually used as ansatz,

$$\sigma_f = C_0 \left(\lambda + 1 + b_1\lambda^{-1} + b_2\lambda^{-2} + b_3\lambda^{-3} + ...\right)^{-1/2}, \tag{2.128}$$

where the b_i are constants to be determined from experimental data. In practice the ansatz is usually truncated after the second term when the description of the size effect of concrete is envisaged.

2.7 Discrete Fourier Transform and Fast Fourier Transform

Fourier Analysis is a tool commonly used in the context of partial differential equations. The numerical algorithm developed during this project is based on discrete Fourier transforms, thus the principles that are fundamental to this branch of analysis are outlined here. A Fourier series $S_f(t, n)$ is a trigonometric polynomial:

$$S_f(t, n) = \sum_{j=-\infty}^{\infty} c_j e^{j\omega it} \tag{2.129}$$

$$= \frac{a_0}{2} + \sum_{j=-1}^{\infty} \left(a_j \cos(j\omega t) + b_j \sin(j\omega t)\right), \tag{2.130}$$

where $i = \sqrt{-1}$ is the imaginary unit. For a piecewise smooth and continuous function $f(t)$ the Fourier series with the coefficients

$$c_j = \frac{1}{T} \int_0^T f(t)e^{-j\omega it}\, \mathrm{d}t, \qquad j = -n, \cdots, n \tag{2.131}$$

$$a_j = \frac{2}{T} \int_0^T f(t)\cos(j\omega it)\, \mathrm{d}t, \qquad j = 0, \cdots, n \tag{2.132}$$

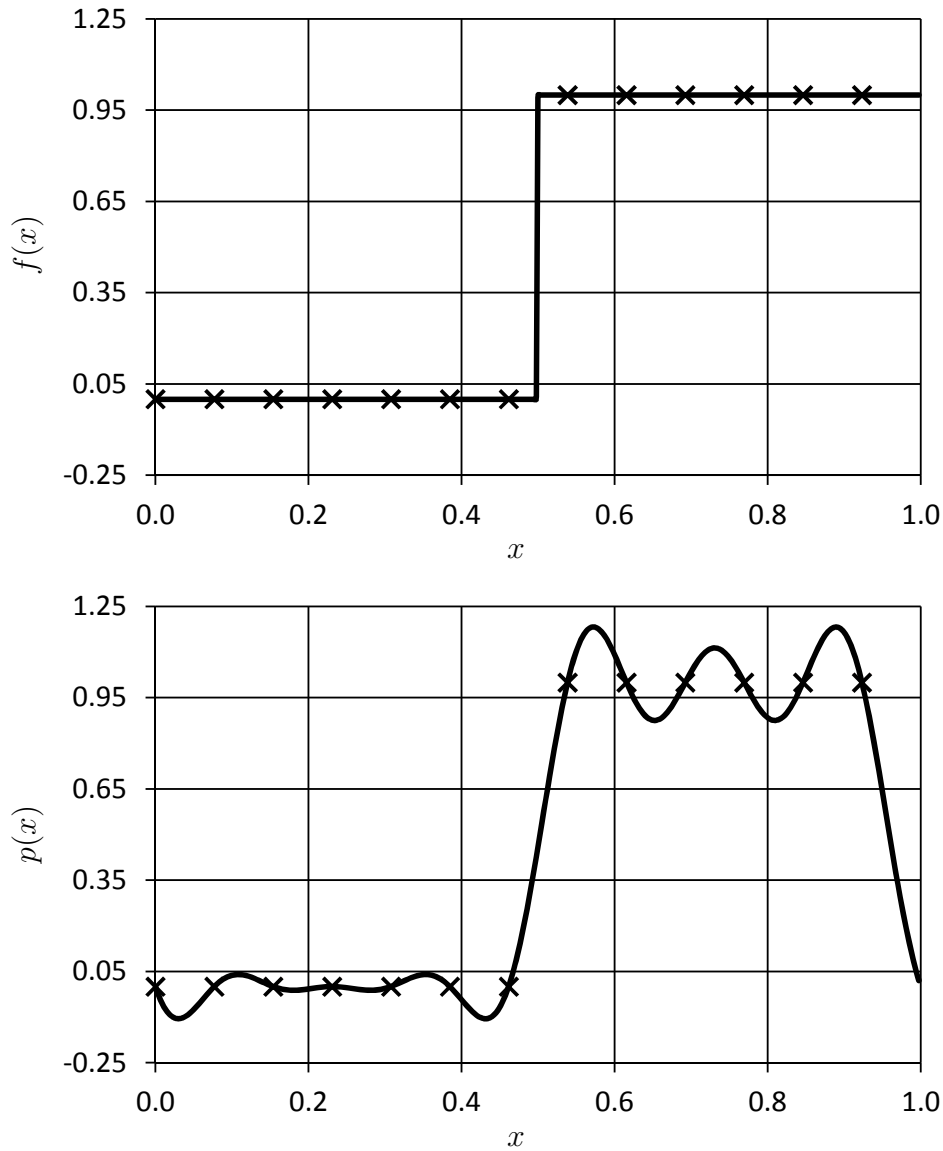$$b_J = \frac{2}{T} \int_0^T f(t)\sin(j\omega it)\, \mathrm{d}t, \qquad j = 1, \cdots, n \tag{2.133}$$

Fig. 2.8: Example for trigonometric interpolation of the Heaviside Stepfuntion Distribution. Top: Original function with sample points. Bottom: Trigonometric interpolation polynomial $p(x)$. $p(x)$ is exact in the sample points and oscillates in between them.

converges uniformly towards the function $f(t)$:

$$f(t) = \lim_{n \to \infty} \sum_{j=-n}^{n} c_j e^{j\omega it}. \tag{2.134}$$

This means that any function that satisfies the above mentioned requirements can be represented as a superposition of harmonic oscillations.

A finite sequence of data points $x(k)$ with $0 \leq k \leq N - 1$ is considered now. In one dimension this could be Young's modulus Y of a bar of length L that is dependent on the position of the cross section, for example. Instead of a continuous function Y is given for N equally spaced positions k along the axis of the bar. The discrete Fourier transform (DFT) generates a new data sequence $X(l)$, according to the transformation rule [111]:

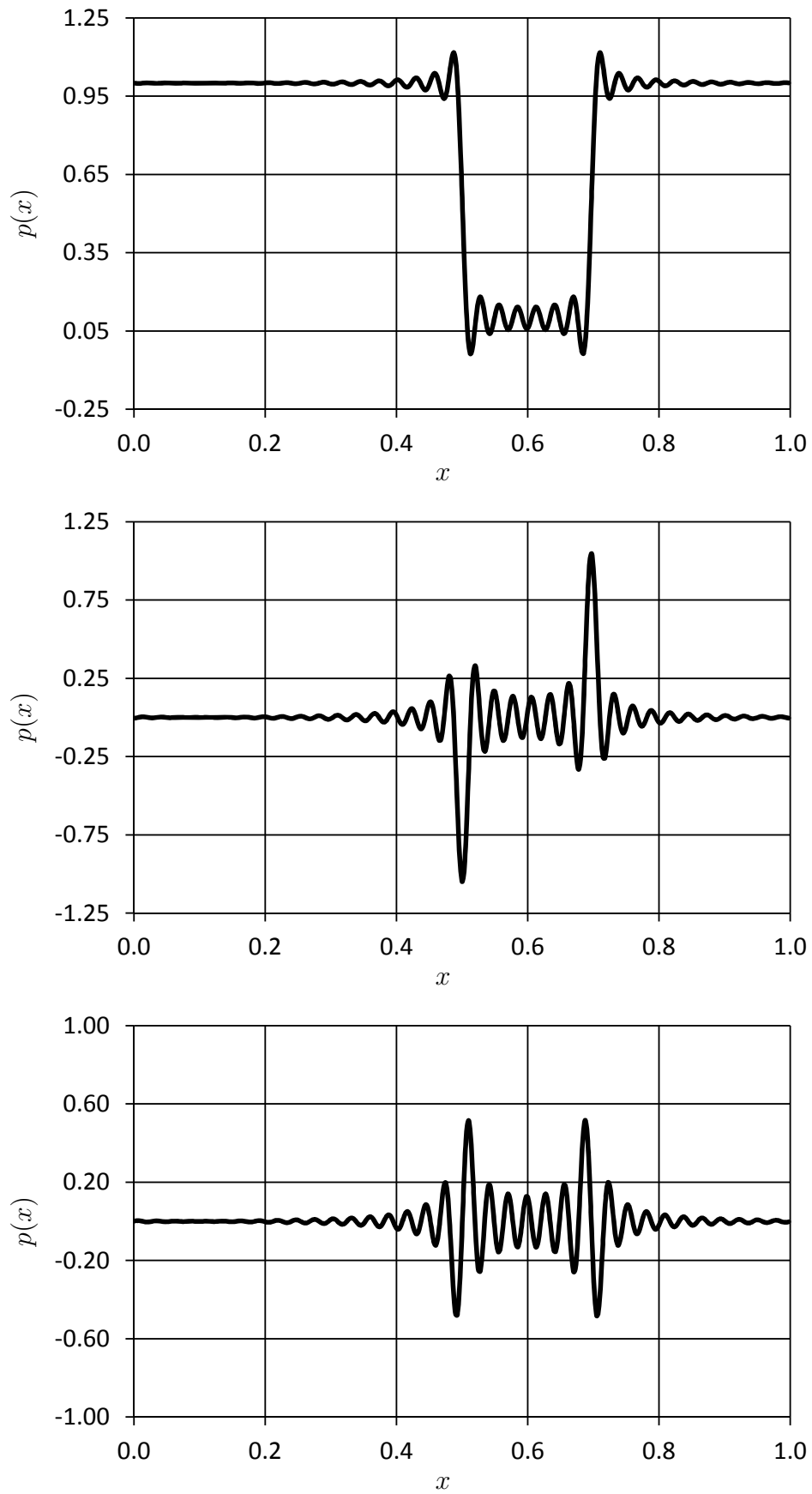$$X(l) = \sum_{k=0}^{N-1} x(k) \exp\left(-i2\pi \frac{kl}{N}\right). \tag{2.135}$$

Fig. 2.9: Trigonometric interpolation of a periodic step signal and its first and second derivative.

Generally the $X(l)$ are complex even if the original sequence is real valued. The frequencies l have to be understood with respect to the sample length, with periodic length:

$$\Lambda_l = \frac{l}{L}.$$

(2.136)

Symbolically, the transformation is written:

$$X(l) = \mathcal{DFT}(x(k))$$

(2.137)

A unique inverse transform also exists [111]:

$$x(k) = \frac{1}{N} \sum_{l=0}^{N-1} X(l) \exp\left(i2\pi \frac{kl}{N}\right).$$

(2.138)

Both the DFT and the inverse DFT are periodic:

$$X(l + N) = X(l)$$

(2.139)

$$x(k + N) = x(k).$$

(2.140)

An interpretation of the DFT is possible as coefficients for a trigonometric interpolation polynomial that approximates the original function. If a trigonometric interpolation is a polynomial of the kind

$$p(\xi) = \sum_{m=-N/2}^{N/2} c_m \exp\left(i2\pi m \frac{\xi}{N}\right)$$

(2.141)

is taken as ansatz, and there are N equally spaced sampling points of the original, there exists a unique solution for the coefficients c_m, which are the $X(l)$ of the DFT. In fig. 2.8 an example is given for interpolation of a polynomial.

The interpolation is also used to obtain formulas to calculate derivatives with respect to ξ of the original function. From 2.141 the first and second derivative for $p(x)$ read:

$$p'(x) = \sum_{m=-N/2}^{N/2} i2\pi \frac{m}{N} c_m \exp\left(i2\pi m \frac{\xi}{N}\right) \tag{2.142}$$

$$p''(x) = \sum_{m=-N/2}^{N/2} 4\pi^2 \frac{m^2}{N} c_m \exp\left(i2\pi m \frac{\xi}{N}\right). \tag{2.143}$$

Since $p'(x)$ and $p''(x)$ are trigonometric interpolations of the derivatives, it is clear that the DFT of the derivatives are:

$$\mathcal{DFT}(x'(k)) = \frac{2\pi l}{N} i X(l) \tag{2.144}$$

$$\mathcal{DFT}(x''(k)) = -\frac{4\pi^2 l^2}{N^2} X(l). \tag{2.145}$$

The Nyquist frequency is defined as half of the highest sampling frequency [23]:

$$f_{Ny} \frac{N}{2}. \tag{2.146}$$

It is known from signal processing that the Nyquist frequency should be equal or higher than the highest frequency present in the original signal or data set, in order to guarantee a complete reconstruction of the original data from the frequency spectrum (via inverse DFT). This poses a problem when the DFT of step functions is needed. Infinite frequencies are contained in the step function, and the trigonometric interpolation, as well as any other, over- and undershoots the original function at the points of discontinuity [23]. This behavior cannot be controlled by choice of larger samples with high frequencies. A consequence from this is that if the derivatives are calculated using (2.145) the results get rougher with increasing number of differentiations, and again this behavior cannot be controlled with higher sampling rates. The Derivative should be zero everywhere except for the discontinuities where it is not defined. Fig. 2.9 illustrates this problem. The step function is important for this work, since heterogeneous microstructures usually consist of different phases separated by surfaces across which a jump in elastic parameters occurs. In those cases jumps always occur in some stress and strain components.

Direct computation of the DFT is computationally expensive: For a sequence of N sample points there are

$$N^2 - N \quad \text{complex additions, and} \tag{2.147}$$

$$N^2 \quad \text{complex multiplications} \tag{2.148}$$

to be performed. Thus the amount of resources consumed in the transformation grows quadratically with increasing N [111]. But with the Fast Fourier transform (FFT) algorithms developed in the middle of the last century, the time consumed can be reduced considerably. If the original sequence $x(k)$ is decomposed into a sequence containing all evenly indexed and one containing all oddly indexed entries,

$$x'(k) = x(2k) \tag{2.149}$$

$$x''(k) = x(2k+1), \tag{2.150}$$

then the DFT can be rewritten as

$$X(l) = \sum_{k=0}^{N/2-1} x(2k)w_N^{2kl} + \sum_{k=0}^{N/2-1} x(2k+1)w_N^{(2k+1)l} \tag{2.151}$$

$$= \sum_{k=0}^{N/2-1} x'(k)w_N^{2kl} + w_N^l \sum_{k=0}^{N/2-1} x''(k)w_N^{2kl}. \tag{2.152}$$

In (2.152) the DFT of a sequence of N sample points has been reduced to two DFT's of $N/2$-point sequences either. The cost has been reduced to

$$\frac{N^2 - N}{2} \qquad \text{complex additions, and} \tag{2.153}$$

$$\frac{N^2}{2} \qquad \text{complex multiplications,} \tag{2.154}$$

thus by a factor of 2. The two DFT's in (2.152) can each be further reduced and a nested scheme is achieved that is considerably more economic than the original DFT. Generally, the computational cost grows with $N \log_2 N$ for increasing N when FFT algorithms are applied. Examples for different algorithms have been proposed in [30, 54, 140], for example.

3 Physical Model and Numerical Algorithm

When a multiscale ansatz for non-linear material models (e.g. quasi-brittle damage mechanics) is to be treated numerically, a multiscale finite element method is usually applied. This means that in addition to the global boundary value problem, secondary boundary value problems have to be solved for each integration point (Gauss point). Although the FE^2 method (see sec. 2.5) is probably the one preferred by most authors of scientific publications, there is no restriction in general on the choice of the numerical method used for the sub-models, as long as it is appropriate to approximate the solution of the problem at hand. In this work a nonlocal quasi-brittle damage model based on the effective stress concept (see p. 31) is applied on the microstructure. Only two-phase composites are considered, although the quantity of different phases is not limited by the methods employed. A very prominent example for two-phase composites where at least one phase exhibits quasi-brittle behavior are steel-reinforced concrete parts, and results for some corresponding examples will be shown later on. A linear elastic model (small deformations, generalized Hooke's law, see sec. 2.1) is chosen as basis. The basic mathematical problem is formulated on p. 33 and repeated here (for a comfortable reading experience):

$$\Pi(\mathbf{u}, d) = \int_{\mathcal{D}} \psi_0 + r \left| \dot{d} \right| \, \mathrm{d}V + \int_{\mathcal{D}} \mathbf{u} \cdot (\rho \mathbf{b}) \, \mathrm{d}V - \int_{\partial \mathcal{D}} \mathbf{u} \cdot \mathbf{t} \, \mathrm{d}A. \tag{3.1}$$

A further field variable φ will be introduced, and additional terms including the gradient (with respect to space coordinates $\mathbf{x}$) of φ and the difference between $f(d)$ and φ are added to the free energy formulation, which gives the model a non-local character. Details on that are given in sec. 3.2. Instead of the Finite Element Method an FFT-based iterative procedure is employed. The formulation of this algorithm is based on a method developed in the nineties by Moulinec and Suquet [105, 106]. Some notes on their proposal are given in sec. 3.1. In sec. 3.2 the model developed for this work is presented, and in sec. 3.3.2 and 3.3.1 the sources of numerical uncertainties and the overall accuracy are discussed.

3.1 FFT based algorithm by Moulinec and Suquet

Instead of starting from (2.16) Moulinec and Suquet considered the Lippmann-Schwinger type integral equation (2.86) for boundary value problems with non-homogeneous distribution of elastic properties. When (2.86) is transformed into Fourier space, the convolution integral is transformed into an inner product, which is much easier to evaluate:

$$\hat{\boldsymbol{\epsilon}}(\mathbf{l}) = -\hat{\boldsymbol{\Gamma}}^0 : \boldsymbol{\tau}(\mathbf{l}) \qquad \forall \mathbf{l} \neq 0, \, \hat{\boldsymbol{\epsilon}}(0) = \mathbf{E}. \tag{3.2}$$

The hat in this equation refers to the Fourier transform of a given quantity:

$$\hat{\mathbf{v}} = \mathcal{F}(\mathbf{v}). \tag{3.3}$$

Since the boundary conditions imply periodic stress and strain fields, and the periodicity of the microstructure is given by definition of the representative volume element (RVE), the discrete Fourier transform is applicable. When a cubic RVE of sidelength L is discretized by an array of $N \times N \times N$ sample points $\mathbf{x}_r$ (with $r = 1, ..., N^3$), the integral equation becomes:

$$\boldsymbol{\epsilon}(\mathbf{x}_r) = -\boldsymbol{\Gamma}^0(\mathbf{x}_r) * \boldsymbol{\tau}(\mathbf{x}_r) + \mathbf{E}, \tag{3.4}$$

then the discrete Fourier transform reads:

$$\hat{\boldsymbol{\epsilon}}(\mathbf{l}_d) = -\hat{\boldsymbol{\Gamma}}^0(\mathbf{l}_d) : \hat{\boldsymbol{\tau}}(\mathbf{l}_d) \qquad \forall \mathbf{l}_d \neq 0, \widehat{\boldsymbol{\epsilon}}(0) = \mathbf{E}. \tag{3.5}$$

The Greens operator in discrete Fourier space reads:

$$\Gamma^0_{ijkh}(\boldsymbol{\xi}) = \frac{1}{4\mu^0|\boldsymbol{\xi}|^2} \left(\delta_{ki}\xi_h\xi_j + \delta_{hi}\xi_k\xi_j + \delta_{kj}\xi_h\xi_i + \delta_{hk}\xi_j\xi_i \right)$$
$$- \frac{\lambda^0 + \mu^0}{\mu^0(\lambda^0 + 2\mu^0)} \frac{\xi_i\xi_j\xi_k\xi_h}{|\boldsymbol{\xi}|^4}. \tag{3.6}$$

Moulinec and Suquet suggested to use the fixpoint iteration method with the starting point $\boldsymbol{\epsilon}^0 = \mathbf{E}$ to find solution $\boldsymbol{\epsilon}(\mathbf{x})$ and $\boldsymbol{\sigma}(\mathbf{x})$. By exploiting the relationship

$$\boldsymbol{\Gamma}^0 * (\mathbf{C}^0 : \boldsymbol{\epsilon}) = \boldsymbol{\epsilon} \tag{3.7}$$

the scheme for the algorithm is:

$$
\left.
\begin{aligned}
&\text{Initialization:} \quad \boldsymbol{\epsilon}^0(\boldsymbol{x}_d) = \boldsymbol{E}, \quad \forall \boldsymbol{x}_d \in V, \\
&\qquad\qquad \boldsymbol{\sigma}^0(\boldsymbol{x}_d) = \mathbb{C}(\boldsymbol{x}_d) : \boldsymbol{\epsilon}^0(\boldsymbol{x}_d), \forall \boldsymbol{x}_d \in V, \\
&\text{Iterate } i+1: \quad \boldsymbol{\epsilon}^i \quad \text{and} \quad \boldsymbol{\sigma}^i \quad \text{known at every} \quad \boldsymbol{x}_d \\
&\quad (a) \quad \widehat{\boldsymbol{\sigma}}^i = \mathscr{F}\mathscr{F}\mathscr{T}(\boldsymbol{\sigma}^i) \\
&\quad (b) \quad \text{convergence test} \\
&\quad (c) \quad \widehat{\boldsymbol{\epsilon}}^{i+1}(\boldsymbol{\xi}_d) = \widehat{\boldsymbol{\epsilon}}^i(\boldsymbol{\xi}_d) - \widehat{\Gamma}^0(\boldsymbol{\xi}_d) : \widehat{\boldsymbol{\sigma}}^i(\boldsymbol{\xi}_d) \, \forall \boldsymbol{\xi}_d \neq 0, \widehat{\boldsymbol{\epsilon}}(0) = \boldsymbol{E}, \\
&\quad (d) \quad \boldsymbol{\epsilon}^{i+1} = \mathscr{F}\mathscr{F}\mathscr{T}^{-1}(\widehat{\boldsymbol{\epsilon}}^{i+1}), \\
&\quad (e) \quad \boldsymbol{\sigma}^{i+1}(x_d) = \mathbb{C}(x_d) : \boldsymbol{\epsilon}^{i+1}(x_d), \quad \forall \boldsymbol{x}_d \in V.
\end{aligned}
\right\} \tag{3.8}
$$

Convergence is reached when $\boldsymbol{\sigma}^{i+1}$ is in equilibrium [106], thus the convergence is checked with the error:

$$e^i = \frac{(\|\text{div}\boldsymbol{\sigma}^i\|)^{1/2}}{\|\langle\boldsymbol{\sigma}^i\rangle\|} \tag{3.9}$$

which in discrete Fourier space reads:

$$\widehat{e}^i = \frac{1}{\|\widehat{\boldsymbol{\sigma}}^i(0)\|} \sqrt{\frac{1}{N^3} \sum_{j=1}^{N^3} \left(\frac{2\pi}{L} \|\mathbf{l}_j \cdot \widehat{\boldsymbol{\sigma}}^i(\mathbf{l}_j)\| \right)^2}. \tag{3.10}$$

The original motivation for the development of this method came from the idea to calculate the efficient non-linear properties from data obtained from digital images of the microstructure that can be read in pixel-wise easily. In case of complex microstructures, like

matrix-precipitation type alloys, the difficulties due to the meshing of the geometry for Finite Element Analysis is avoided. In addition, no assembly of a global stiffness matrix is necessary and thus the problem is partly reduced. $\mathcal{FFT}$ algorithms can be used and the computation time varies with $N \cdot \log_2 N$. On SMP computer systems there is a high potential for parallelization, which lies in the $\mathcal{FFT}$ itself and in the fact that the operations in steps c and d in (3.8) can be done in parallel for each component. The algorithm convergence is fast (usually below ten iterations), but it has to be said that the convergence rate depends on the ratio between the elastic properties of different phases. A high contrast in the properties decreases the convergence rate.

Moulinec and Suquet also gave an algorithm for strain-hardening plasticity and thereby demonstrated the suitability of their method for non-linear materials. They further developed their ideas and published results in [107] for example. Eyre and Milton discuss the adaption of discretization in [46] and Lebensohn gave examples for application of the described concept in [83] and [84].

3.2 Nonlocal Damage Model

In order to formulate a damage model, a thermodynamic potential similar to the one in (2.116) has to be proposed. To avoid the pathological mesh dependency discussed on page 33 additional gradient terms are added. Contrary to the idea of Peerlings and others [117–119], the gradient of the strain field $\epsilon(\mathbf{x})$ or of the elastic energy ψ^0 are not used, because calculation of these quantities is computationally expensive and is a source of numerical errors. Instead, an additional scalar field variable φ is introduced and linked to the damage variable field.

We use a scalar damage model similar to that proposed in [34–36], with small adaption to our purpose. The basic idea is that local damage, like spontaneous crack initiation, lowers the macroscopic properties of the material, i.e. the elastic stiffness. Thus a scalar factor $f(d)$ is addmultiplied by the elastic energy,

$$\tilde{\psi} = f(d)\psi_0 = \frac{1}{2} f(d)\,\epsilon : \mathbf{C} : \epsilon \tag{3.11}$$

that simulates the drop in elastic properties. Here the parameter d refers to the scalar damage of the material, and f determines the effect of d on the physical property $\mathbb{C}$. Different choices are possible for f, but all of them have to maintain the following properties:

$$f(0) = 1 \qquad \text{and} \qquad \lim_{d \to \infty} f(d) = 0\,. \tag{3.12}$$

From that pure elastic behavior for $d = 0$ is inferred, since a factor $f(0) = 1$ will not influence the elastic energy. The classical ansatz for $f(d)$ is given in (2.107), but this choice poses numerical problems, since big round off errors have to be expected for $d \to 1$, and there is a risk of numerical instabilities when the nominator $1 - d$ assumes values near the machine precision of 10^{-16}. From the several alternative possibilities for $f(d)$ presented in [35], the function

$$f(d) = e^{-d} \tag{3.13}$$

was chosen for the present implementation. Compliance with conditions (3.12) is easily verified, and because of

$$f'(d) = -e^{-d} = -f(d) \tag{3.14}$$

there is no need to operate directly on the scalar field d, as will be seen, thus it is sufficient to consider the data of $f(d)$ when implementing the model. Additionally, this formulation avoids the numerical difficulties mentioned for the classical ansatz.

The enhanced free energy is then given as:

$$\psi = f(d)\psi_0 + \frac{\alpha}{2}(f(d) - \varphi(\boldsymbol{x}))^2 + \frac{\beta}{2}\left|\nabla\varphi(\boldsymbol{x})\right|^2, \tag{3.15}$$

and the dissipation potential is

$$\Delta_D = r\left|\dot{d}_+\right|, \tag{3.16}$$

where the index d is used to distinguish the symbol for the dissipation potential from the symbol of the Laplacian operator. The variable d of course also depends on $\boldsymbol{x}$ but for the

sake of clarity the argument is omitted in (3.15). The parameter r can be interpreted as an energy rate dissipated in damage evolution. Damage evolution starts when the reduction of elastic energy in the first term in (3.15) is at least equal to the energy dissipated in the process. The second and third terms put an additional restriction on damage evolution, since they increase the dissipative energy needed when the stiffness deteriorates only in a locally confined area. Parameter α determines the difference that is allowed between $f(d)$ and $\varphi(\boldsymbol{x})$. Both fields tend to be the same for $\alpha \to \infty$ in order to minimize (3.15). In the same way parameter β influences the gradient of $\varphi(\boldsymbol{x})$, or better, the absolute value of the gradient, because a high β suppresses high gradients of $\varphi(\boldsymbol{x})$. This means that β controls the effective range that a locally existing damage has, and α determines how strong these effects are. Both quantities are material parameters and have to be determined from experiments. The quantity φ describes the non-local area of influence of existing damage.

The principle of the minimum of the dissipation potential is applied [63], which reads in symbolic notation:

$$\dot{\psi} + \Delta_d \leftarrow \min_{d, \dot{d}_+}. \tag{3.17}$$

and the potential 3.15 has to be minimized with respect to the arguments $\mathbf{u}(\mathbf{x})$ and $\varphi(\mathbf{x})$. A standard variational argument yields the conditions:

$$\int_{\mathcal{D}} \frac{\partial \psi}{\partial \boldsymbol{\epsilon}} : \delta \boldsymbol{\epsilon} \, \mathrm{d}V - \int_{\mathcal{D}} \delta \mathbf{u} \cdot (\rho \mathbf{b}) \, \mathrm{d}V - \int_{\partial \mathcal{D}} \delta \mathbf{u} \cdot \mathbf{t} \, \mathrm{d}A = 0, \quad \forall \delta \boldsymbol{\epsilon} \tag{3.18}$$

$$\int_{\mathcal{D}} \left\{ f'\psi_0 + \alpha(f - \varphi)f' + r \, \mathrm{sign}(\dot{d}_+) \right\} \delta d \, \mathrm{d}V = 0, \quad \forall \delta d, \, \dot{d}_+ \neq 0 \tag{3.19}$$

$$\int_{\mathcal{D}} -\alpha(f - \phi)\delta\phi + \beta\nabla\phi\nabla\delta\phi \, \mathrm{d}V = 0, \quad \forall \delta\varphi \tag{3.20}$$

see for example in [137]. The symbol 'sign' stands for the signum function:

$$\mathrm{sign}(x) = \begin{cases} -1 & \text{for } x < 0 \\ 1 & \text{for } x > 0 \end{cases}. \tag{3.21}$$

The solution of the integral equation (3.19) is the elastic state of the material body under the given boundary conditions. A solution algorithm for the elastic part is already available with the one discussed in sec. 3.1, and further discussion focuses on evaluation of (3.19) and (3.20). The factor $\nabla\delta\varphi$ in (3.20) can be eliminated. The integral is reformulated by the use of Gauss's theorem:

$$\int_{\mathcal{D}} \left\{ -\alpha(f - \varphi) \right\} \delta\varphi + \beta\nabla\varphi\nabla\delta\varphi \, \mathrm{d}V$$

$$= \int_{\mathcal{D}} -\alpha(f - \varphi)\delta\varphi \mathrm{d}V - \int_{\mathcal{D}} \beta\nabla^2\varphi\delta\varphi \, \mathrm{d}V + \int_{\partial \mathcal{D}} \beta\nabla\varphi \cdot \mathbf{n}\delta\varphi \, \mathrm{d}A. \tag{3.22}$$

Vanishing flux across boundaries for the non-local variable has been called a natural boundary condition, e.g. discussed in [32, 92, 117–119]:

$$\nabla\varphi \cdot \mathbf{n} = 0 \quad \forall \mathbf{x} \in \partial \mathcal{D}. \tag{3.23}$$

Thus, the last term in (3.22) vanishes and (3.20) can finally be written as:

$$\int_{\mathcal{D}} \{-\alpha(f-\varphi)\}\,\delta\varphi + \beta\nabla\varphi\nabla\delta\varphi\,\mathrm{d}V$$

$$= \int_{\mathcal{D}} \{-\alpha(f-\varphi) - \beta\Delta\varphi\}\,\delta\varphi\,\mathrm{d}V = 0 \quad \forall\delta\varphi. \tag{3.24}$$

The integral in (3.24) can only vanish if the integrand is identical to zero for every $\mathbf{x}$ in $\mathcal{D}$. Thus a scalar partial differential equation of the Helmholtz kind with an inhomogeneous term is encountered:

$$\varphi - \frac{\beta}{\alpha}\Delta\varphi = f. \tag{3.25}$$

This equation relates φ to f, and it is obvious that the ratio $\frac{\beta}{\alpha}$ determines the form of the solution φ.

(3.19) yields, following the same argument as above, that the integrand is identical to zero:

$$\frac{\partial\psi}{\partial d} = f'\psi_0 + \alpha(f-\varphi)f' + r\,\mathrm{sign}(\dot{d}_+)\,\mathrm{for}\,\dot{d}_+ \neq 0. \tag{3.26}$$

The energy has a discontinuity at $\dot{d}_+ = 0$ because of the function $\left|\dot{d}_+\right|$, thus the derivative in its classical sense does not exist. However, since $\left|\dot{d}_+\right|$ is a convex function a subdifferential exists at this point, which is the set of slopes of possible tangents on the graph of the function. The tangent with zero slope is also included:

$$0 \in f'\psi_0 + \alpha(f-\varphi)f' + r\,\mathrm{sign}(\dot{d}_+), \quad \dot{d}_+ = 0. \tag{3.27}$$

The case $\dot{d}_+ = 0$ naturally is of particular interest for the proposed model, since it indicates the onset of damage evolution. With (3.27) it can be included into further analysis. This is a standard argument in thermodynamically motivated nonlinear material modeling, see for example [75] for another example. From the mathematical perspective the concept of the subdifferential or subderivative is a generalization of the classical derivative. Details can be found in textbooks on convex analysis, e.g. [69]. (3.26) is rewritten as

$$r\,\mathrm{sign}(\dot{d}_+) = -f'\psi_0 - \alpha(f-\varphi)f', \tag{3.28}$$

and because of the property

$$r \geq r\,\mathrm{sign}(\dot{d}_+) \tag{3.29}$$

and using the property (3.14):

$$r \geq \alpha f^2 + (\psi_0 - \varphi\alpha)f. \tag{3.30}$$

(3.30) can be interpreted as equivalent to the yield function in classical plasticity. It is a scalar function that is valid for every $\mathbf{x}$ in $\mathcal{D}$. For a given damage distribution d and elastic strain energy ψ_0 (3.30) must always hold. If ψ_0 increases (because of increasing macroscopic strain) such that (3.30) is no longer satisfied, then the damage parameter d has

to increase such that $f(d) = e^{-d}$ decreases, and (3.30) is satisfied again. The equation to determine a new value f^{n+1} in the case that f^n no longer satisfies (3.30) is

$$r = \alpha f^2 + (\psi_0 - \varphi \alpha) f, \tag{3.31}$$

which is a quadratic function that reads in normalized form:

$$f^2 + \frac{1}{\alpha} (\psi_0 - \varphi \alpha) f - \frac{r}{\alpha} = 0. \tag{3.32}$$

Two solutions are available:

$$f_{1/2} = \frac{1}{2\alpha} (\varphi \alpha - \psi_0) \pm \frac{1}{2\alpha} \sqrt{(\varphi \alpha - \psi_0)^2 + 4r^2}. \tag{3.33}$$

The function f cannot be smaller than zero, and because of

$$\sqrt{(\varphi \alpha - \psi_0)^2 + 4r^2} > (\varphi \alpha - \psi_0) \tag{3.34}$$

only one solution is admissible:

$$f^{n+1} = \frac{1}{2\alpha} (\varphi \alpha - \psi_0) + \frac{1}{2\alpha} \sqrt{(\varphi \alpha - \psi_0)^2 + 4r^2}. \tag{3.35}$$

With (3.25) and (3.35) two equations are available to determine φ and f. What makes this approach suitable to be formulated as an algorithm similar to the one presented in [106] is the fact that the differential operator in (3.25) becomes a local operator in Fourier space,

$$\widehat{\varphi}(\boldsymbol{\xi}) = \frac{1}{1 + \frac{\beta}{\alpha} |\boldsymbol{\xi}|^2} \widehat{f}(\boldsymbol{\xi}), \tag{3.36}$$

or, applying discrete fourier transform,

$$\widehat{\varphi}(\boldsymbol{\xi}_i) = \frac{1}{1 + \frac{\beta}{\alpha} \frac{4\pi^2}{L^2} |\boldsymbol{\xi}_i|^2} \widehat{f}(\boldsymbol{\xi}_i), \tag{3.37}$$

where L is the phase-length of the periodic microstructure, and $\boldsymbol{\xi}_i$ is the coordinate vector in discrete frequency space. Hooke's law is obtained from (3.15) via differentiation with respect to $\boldsymbol{\epsilon}$:

$$\frac{\partial \psi}{\partial \boldsymbol{\epsilon}} = f(d) \, \mathbf{C} : \boldsymbol{\epsilon}. \tag{3.38}$$

Given equations (3.37), (3.35) and (3.38), the necessary modifications of the original algorithm presented in sec. 3.1 are now clear. Hooke's law has to be rewritten according to (3.38) and equations (3.37) and (3.35) have to be inserted in the correct positions. Equation (3.39) gives the modified algorithm. Each step that comes from the original algorithm is marked with a single letter, whereas the steps that have been added are marked with indexed

letters (e.g. (a_1)):

$$
\left.
\begin{aligned}
&\text{Initialization}: \quad \boldsymbol{\epsilon}^0(\mathbf{x}_d) = \mathbf{E}^n, \, \forall \mathbf{x}_d \in V, \, \text{loadstep } n \\
&\qquad\qquad\qquad \boldsymbol{\sigma}^0(\mathbf{x}_d) = f^{n,0}(\mathbf{x}_d)\,\mathbb{C}(\mathbf{x}_d) : \boldsymbol{\epsilon}^0(\mathbf{x}_d), \forall \mathbf{x}_d \in V, \\
&\text{Iterate } i+1: \quad \boldsymbol{\epsilon}^i \quad \text{and} \quad \boldsymbol{\sigma}^i \quad \text{known at every} \quad \mathbf{x}_d \\
&\qquad (a) \quad \widehat{\boldsymbol{\sigma}}^i = \mathscr{F}\mathscr{F}\mathscr{T}(\boldsymbol{\sigma}^i) \\
&\qquad (a_1) \quad \widehat{f}(\boldsymbol{\xi}_d) = \mathscr{F}\mathscr{F}\mathscr{T}(f^i) \\
&\qquad (b) \quad \text{convergence test} \\
&\qquad (c) \quad \widehat{\boldsymbol{\epsilon}}^{i+1}(\boldsymbol{\xi}_d) = \widehat{\boldsymbol{\epsilon}}^i(\boldsymbol{\xi}_d) - \widehat{\Gamma}^0(\boldsymbol{\xi}_d) : \widehat{\boldsymbol{\sigma}}^i(\boldsymbol{\xi}_d) \quad \forall \boldsymbol{\xi}_d \neq 0, \widehat{\boldsymbol{\epsilon}}(0) = \mathbf{E}, \\
&\qquad (c_1) \quad \widehat{\varphi}^{i+1}(\boldsymbol{\xi}_d) = \frac{1}{1 + \frac{\beta}{\alpha}\frac{4\pi^2}{L^2}|\boldsymbol{\xi}|_d^2}\widehat{f}(\boldsymbol{\xi}_d) \\
&\qquad (d) \quad \boldsymbol{\epsilon}^{i+1} = \mathscr{F}\mathscr{F}\mathscr{T}^{-1}(\widehat{\boldsymbol{\epsilon}}^{i+1}), \\
&\qquad (d_1) \quad \varphi^{i+1}(\mathbf{x}_d) = \mathscr{F}\mathscr{F}\mathscr{T}^{-1}(\widehat{\varphi}^{i+1}) \\
&\qquad\qquad\quad f^{i+1}(\mathbf{x}_d) = \mathscr{F}\mathscr{F}\mathscr{T}^{-1}\left(\widehat{f}^{i+1}\right) \\
&\qquad (d_2) \quad f^{i+1} = \min\left\{ f^n, \right. \\
&\qquad\qquad \left. \frac{1}{2\alpha}\left(\alpha\varphi^{i+1} - \psi_0^{i+1}\right) + \frac{1}{2\alpha}\sqrt{\left(\alpha\varphi^{i+1} - \psi_0^{i+1}\right)^2 + 4r^2} \right\} \\
&\qquad (e) \quad \boldsymbol{\sigma}^{i+1}(\mathbf{x}_d) = f^{i+1}(\mathbf{x}_d)\,\mathbf{C}(\mathbf{x}_d) : \boldsymbol{\epsilon}^{i+1}(\mathbf{x}_d), \quad \forall \mathbf{x}_d \in V
\end{aligned}
\right\} \quad (3.39)
$$

To check convergence in step (b) the same criterion that was used in the original publication is applied, see (3.10). Since damage mechanics models are nonlinear by nature, it is usually not possible to apply the overall load at once and expect good results. The loadpath has to be discretized into N steps, and the index to label a certain loadstep is n throughout this work. Thus the index i in (3.39) refers to the iterative procedure to find the fix-point of (3.5) under the constraints imposed by (3.37) and (3.30). The structure of the nested iterative procedure for an RVE is presented in fig. 3.1. A remark has to be made about step (d_2). Instead of checking compliance with (3.30) for every point in every loadstep, the value for f is calculated each time, and if the new one f^{i+1} is smaller than the result f^n from the previous loadstep it is used for the next iteration. It is important to compare f^{i+1} to f^n from the previous loadstep in each iteration, since this way it is assured that the old value for f can be restored by the algorithm in case that it was underestimated in the first iteration. A consequence of (3.14) is that only f appears in (3.39) and no mentioning of the damage parameter d is needed. Thus from the computational point of view it is economically favorable to only store values of the field variable f rather than storing d and calculating $f(d) = e^{-d}$ every time it is needed.

Start

$\underline{\varepsilon}=0$
$\underline{E}=0$
$f=1$
$\varphi=1$

$n\leq1000$

yes

$n=n+1$
$\underline{E}^{n}=\underline{E}^{n-1}+\Delta\underline{E}$

FFT-Algorithm
(counting variable i)

$\underline{\varepsilon}^{n}=\underline{\varepsilon}^{i}$
$f^{n}=f^{I}$
$\varphi^{n}=\varphi^{i}$

$\underline{\varepsilon}^{1000}, \underline{\sigma}^{1000}$
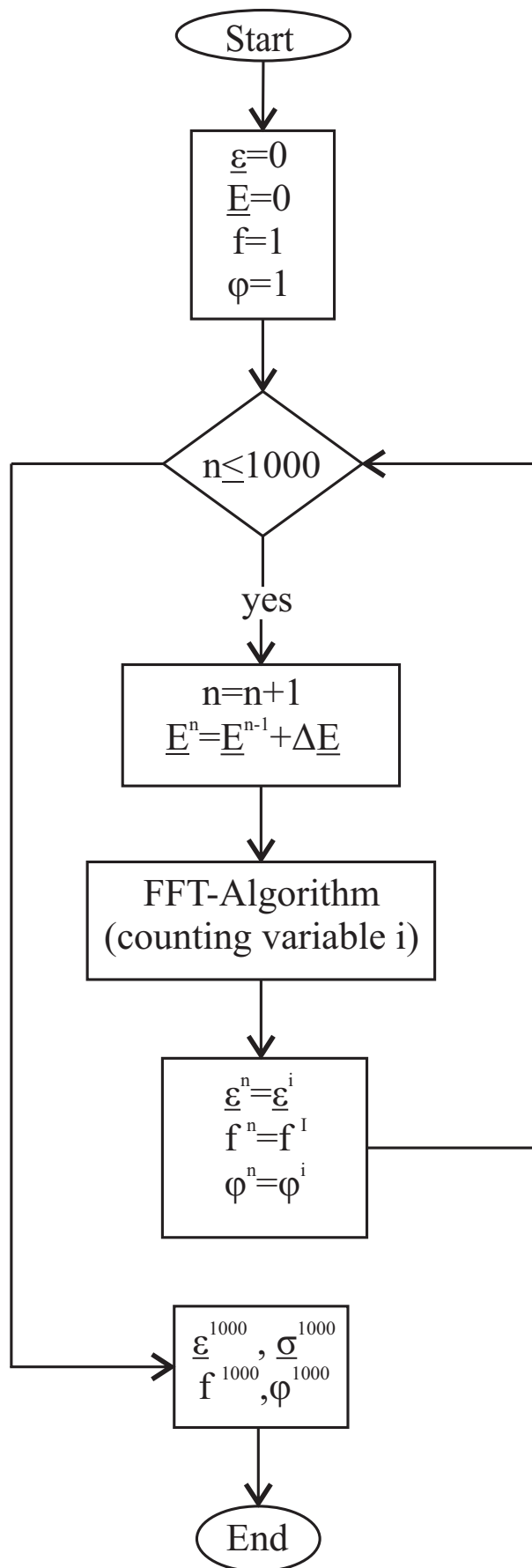f^{1000}, φ^{1000}

End

Fig. 3.1: Structure of the nested iterative procedure

3.3 Numerical Uncertainties

For the computational algorithm presented in (3.39) the question of numerical accuracy naturally arises. For the Finite Element Method, especially in the linear case, there is much literature available that discusses reliability, convergence and error estimates. For a broad discussion see for example [11]. The algorithm (3.39) is based, as outlined in the previous section, on the idea of Suquet and Moulinec, reviewed in (3.8), which they published in 1998 [106]. Since this idea is relatively new compared to other numerical methods, and also because it is a rather specialized method restricted to problems with periodic boundary conditions, there is not much information available studying the accuracy of the method. The confidence in the reliability of the algorithm (3.8) has been established by experience, as the high number of publications based on it testify. Despite this fact a study about the numerical errors that might occur has been conducted to get a feeling for possible sources of uncertainties. Three main sources can be identified. The first are round off errors that are inherent to any calculation on a machine because of finite processor word length and thus a finite number of digits available to represent each number. The second error is typical to numerical approximations of physical problems and is often called discretization error. In the case studied here discretization means the representation of continuous real world fields like stress, strain and also elastic properties and the damage state of the material by a finite number of equidistant points distributed over space. A choice is made about the resolution of the sampling mesh, and the real world phenomenon can only be approximated to a certain degree with the given choice. A third source of error is the convergence criterion (3.9). For the exact solution the criterion has to be $e^i = 0$, but in any simulation non-zero albeit small limit has to be taken as indicator to stop the iteration. The quality of the numerical solution depends on how small the criterion is chosen and on how good the numerical calculation of e^i is. In the next three sections some arguments about these three sources are given and it will be tried to give a rough estimate about the uncertainty. It is pointed out here that the uncertainty has not been studied in a mathematically rigorous manner except for some simple parts, but in a rather more pragmatic way by analyzing the results of computations.

3.3.1 Round-Off Errors

Round off errors are inherent to any machine-based arithmetic. This is due to the fact that in every machine only a limited number of digits is available to represent a floating point number. The machine representation is flawed with a round off error compared to the exact number, and the error is at least equal to the number represented by the digits that are left out. The last digit in a machine number may also be erroneous because of the rounding up in the process. The algorithm (3.39) is implemented in FORTRAN code, and 8 byte floating point numbers are always used. 8 byte means 15 digits are available, and the relative error of a single number compared to the exact one is the machine precision:

$$\text{eps} = 5 \cdot 10^{-16}. \tag{3.40}$$

It is important to realize that the machine precision is not the actual error of any number, but the uncertainty, which means that the actual error that is made is somewhere between zero and eps. It is well known that the uncertainty increases in arithmetic calculation because the relative errors may add or multiply each other while propagating through the process. The

uncertainty in addition of two machine numbers x^* and y^* is:

$$x^* + y^* = (x + y)(1 + 2\text{eps}),\tag{3.41}$$

and for multiplication the situation gets even worse:

$$x^*y^* = (xy)(1 + 3\text{eps}),\tag{3.42}$$

see [135]. The relative uncertainty of the result, which again is a machine number, is higher than the uncertainty of each of the original numbers, and the error may be higher multiplication than after adding. It is immediately understandable that the uncertainty is further increased in consecutive operations on the numbers, and may eventually spoil the results to the point where they are useless. A prominent example for this situation is the Gauss algorithm for linear systems of equations, that may lead to results totally off the exact solution when the matrix of coefficients is not well conditioned [10].

In case of division of machine numbers the relative uncertainty is not that clear in advance, because division is not a direct operation at the binary level, as addition and multiplication are. Several algorithms are available, e.g. Newton-Raphson or Goldschmitd method [113]. It depends on the chosen compiler software which one is applied.

By inspection of (3.8) the relevant sources of round off errors in the purely elastic algorithm can be identified:

- A fast Fourier transform of the stress components is performed in each iteration (step (a)),

- an inverse Fourier transform of the strain components is performed in each iteration (step (d)),

- Hooke's law and the convolution with the Gamma operator are performed (step (e) and (c), respectively) in each iteration. These represent relatively simple addition and multiplication cases, and

- the operator $\mathbf{\Gamma}(\mathbf{\xi}_i)$ has to be calculated once before the iteration starts

The relative error of $\mathbf{\Gamma}^0$ is denoted by Δ_Γ:

$$\mathbf{\Gamma}^{0*} = \mathbf{\Gamma}^0(1 + \Delta_\Gamma),\tag{3.43}$$

and the relative error after consecutive fast Fourier transform and inverse fast Fourier transform with Δ_{FFT}:

$$\mathscr{F}\mathscr{F}\mathscr{T}^{-1}\left(\mathscr{F}\mathscr{F}\mathscr{T}(\mathbf{\sigma})\right) = \mathbf{\sigma}(1 + \Delta_{\text{FFT}}).\tag{3.44}$$

It is assumed that the relative error after one transform (without inverse transform thereafter) is roughly half of the error after both operations:

$$\mathscr{F}\mathscr{F}\mathscr{T}(\mathbf{\sigma}) = \widehat{\mathbf{\sigma}}\left(1 + \frac{\Delta_{\text{FFT}}}{2}\right).\tag{3.45}$$

This assumption is certainly a simplification but the deviation from the truth should not be too big. In order to analyze the propagation of round off errors through the course of one

iteration it is assumed that $\boldsymbol{\sigma}^i$ and $\boldsymbol{\epsilon}^i$ are given and not flawed with errors. The first step in (3.8) consist of a fast Fourier transform, thus:

$$\mathscr{F}\mathscr{F}\mathscr{T}\left(\boldsymbol{\sigma}^i\right) = \widehat{\boldsymbol{\sigma}}^i \left(1 + \frac{\Delta_{\mathrm{FFT}}}{2}\right). \qquad (3.46)$$

The interpretation of (3.46) is that the result of the machine computation is off by a factor of $\left(1 + \frac{\Delta_{\mathrm{FFT}}}{2}\right)$. Next comes the operation:

$$\widehat{\boldsymbol{\epsilon}}^{i+1} = \widehat{\boldsymbol{\epsilon}}^i - \boldsymbol{\Gamma}^0(\boldsymbol{\xi}_i) : \widehat{\boldsymbol{\sigma}}^i(\boldsymbol{\xi}_i), \qquad (3.47)$$

consisting of six multiplications and six additions for each component:

$$\widehat{\epsilon}_{ij}^{i+1} = \widehat{\epsilon}_{ij}^i - \Gamma_{ij11}^0\widehat{\sigma}_{11} - \Gamma_{ij22}^0\widehat{\sigma}_{22} - \Gamma_{ij33}^0\widehat{\sigma}_{33} - \Gamma_{ij12}^0\widehat{\sigma}_{12} - \Gamma_{ij23}^0\widehat{\sigma}_{23} - \Gamma_{ij13}^0\widehat{\sigma}_{13}. \quad (3.48)$$

The uncertainty after one multiplication of this type is then with (3.45) and (3.43):

$$\left[\Gamma_{ij11}^0\left(1 + \Delta_\Gamma\right) \cdot \widehat{\sigma}_{11}\left(1 + \frac{\Delta_{\mathrm{FFT}}}{2}\right)\right]\left(1 + \mathrm{eps}\right)$$

$$= \Gamma_{ij11}^0 \cdot \widehat{\sigma}_{11}\left(1 + \frac{\Delta_{\mathrm{FFT}}}{2}\right)\left(1 + \Delta_\Gamma\right)\left(1 + \mathrm{eps}\right)$$

$$= \Gamma_{ij11}^0 \cdot \widehat{\sigma}_{11}\left(1 + \Delta_\Gamma + \frac{\Delta_{\mathrm{FFT}}}{2} + \mathrm{eps}\right). \qquad (3.49)$$

The term $(1 + \mathrm{eps})$ after the brackets in the left hand side of (3.49) comes from the fact that not the exact result of the product of two non exact numbers is stored but a round off representation [10, 135]. Square terms of the kind Δ^2 or $\Delta \cdot \mathrm{eps}$ are negligible and dropped in the last step. For the sake of clarity the symbol

$$\Delta_1 = \left(1 + \Delta_\Gamma + \frac{\Delta_{\mathrm{FFT}}}{2} + \mathrm{eps}\right) \qquad (3.50)$$

is introduced. (3.49) is rewritten as

$$\widehat{\epsilon}_{ij}^{i+1} = \widehat{\epsilon}_{ij}^i + T_{11}\Delta_1 + T_{22}\Delta_1 + T_{33}\Delta_1 + T_{12}\Delta_1 + T_{23}\Delta_1 + T_{13}\Delta_1, \qquad (3.51)$$

where the T_{kl} stands for the respective summand $\Gamma_{ijkl}^0\widehat{\sigma}_{kl}$ in (3.49). The first two $T_{ij}-$terms are added and rounded:

$$[T_{11}\Delta_1 + T_{22}\Delta_1]\left(1 + \mathrm{eps}\right) = T_{11}\Delta_1(1 + \mathrm{eps}) + T_{22}\Delta_1(1 + \mathrm{eps}). \qquad (3.52)$$

When the third term is added, the overall result is flawed again:

$$[T_{11}\Delta_1(1 + \mathrm{eps}) + T_{22}\Delta_1(1 + \mathrm{eps}) + T_{33}\Delta_1]\left(1 + \mathrm{eps}\right)$$
$$= (T_{11} + T_{22})\Delta_1(1 + \mathrm{eps})^2 + T_{33}\Delta_1(1 + \mathrm{eps}), \qquad (3.53)$$

and finally the result

$$\widehat{\epsilon}_{ij}^i(1 + \mathrm{eps}) + (T_{11} + T_{22})\Delta_1(1 + \mathrm{eps})^6 + T_{33}\Delta_1(1 + \mathrm{eps})^5$$
$$+ T_{12}\Delta_1(1 + \mathrm{eps})^4 + T_{23}\Delta_1(1 + \mathrm{eps})^3 + T_{13}\Delta_1(1 + \mathrm{eps})^2$$
$$< (T_{11} + T_{22} + T_{33} + T_{12} + T_{23} + T_{13})\Delta_1(1 + \mathrm{eps})^6 \qquad (3.54)$$

is obtained. Thus the relative uncertainty at this point is (square terms dropped out again):

$$\Delta_2 < \Delta_1(1 + \mathrm{eps})^6 = (1 + \Delta_\Gamma + \frac{\Delta_{\mathrm{FFT}}}{2} + 7\,\mathrm{eps}). \qquad (3.55)$$

The inverse Fourier transform yields:

$$\mathscr{F}\mathscr{F}\mathscr{T}^{-1}\left(\epsilon_{ij}\widehat{(1+\Delta_2)}\right) = \epsilon_{ij}(1+\Delta_2)(1+\frac{\Delta_{\text{FFT}}}{2})$$
$$= \epsilon_{ij}(1+\Delta_\Gamma+\Delta_{\text{FFT}}+7\,\text{eps}). \tag{3.56}$$

The last step in (3.8) is the evaluation of Hooke's law, again a double inner product. The argument goes along the same line as in (3.48) to (3.54), thus:

$$\mathbf{C}:\boldsymbol{\epsilon}^{i+1}(1+\Delta_\Gamma+\Delta_{\text{FFT}}+7\,\text{eps})(1+\text{eps})^5$$
$$= \mathbf{C}:\boldsymbol{\epsilon}^{i+1}(1+\Delta_\Gamma+\Delta_{\text{FFT}}+12\,\text{eps}), \tag{3.57}$$

and the overall relative uncertainty in the stress field after one iteration in (3.8) is:

$$\Delta_{\text{iter}} = \Delta_\Gamma + \Delta_{\text{FFT}} + 12\,\text{eps}. \tag{3.58}$$

After a second iteration the uncertainty factor is

$$(1+\Delta_{\text{iter}})^2 = (1+2\Delta_{\text{iter}}) \tag{3.59}$$

and the calculation of the error after n iterations is straight forward:

$$(1+\Delta_{\text{iter}})^n = (1+n\Delta_{\text{iter}}),$$
$$n\Delta_{\text{iter}} = n\Delta_\Gamma + n\Delta_{\text{FFT}} + 12n\,\text{eps}. \tag{3.60}$$

The value of eps is given in (3.40), and the values of Δ_Γ and Δ_{FFT} are yet to be determined.

The formula for the discrete Fourier transform has been given in (2.135) for a data set of N^3 sample points. For each sample $\widehat{x}(\boldsymbol{\xi}_i)$ in the Fourier space N^3 multiplications and N^3 additions have to be carried out, and having (3.41) and (3.42) in mind it is clear that it is very likely to produce high relative errors for increasing N. In the case of the Fast Fourier transform the number of operations to calculate $\widehat{x}(\boldsymbol{\xi}_i)$ is reduced considerably. It depends on N and on the applied algorithm how many operations are necessary for each sample point. For the current project a library subroutine published by the Numerical Algorithms Group (NAG) has been used to carry out the $\mathscr{F}\mathscr{F}\mathscr{T}$. Although information is given about the underlying algorithm, it is very sparse and without any details. Therefore it is not achievable to directly calculate the relative uncertainty of the results. A more pragmatic approach has been used here: a data set $\zeta(\mathbf{x}_i)$ is produced, transformed into Fourier space and then back into physical space. An exact arithmetic should return the original data. The digital machine returns erroneous data, and the error can be calculated:

$$\mathscr{F}\mathscr{F}\mathscr{T}^{-1}\left(\mathscr{F}\mathscr{F}\mathscr{T}\left(\zeta\right)\right) = \zeta^*, \tag{3.61}$$
$$\Delta_{\text{FFT}} = \frac{|\zeta^* - \zeta|}{\zeta}. \tag{3.62}$$

Since a closed form analysis of the expected uncertainty is not at hand, a simulation based estimate was chosen. Three different kinds of data sets are produced: All in a cubic volume of edge length one with a cartesian coordinate system located at the center of the cube. $\mathbf{x}_i$ and $\mathbf{y}_i$ denote position vectors within the reference system. The first one with a constant distribution $\zeta_i = 1.0 \cdot 10^0$, the second one with a spherical inhomogeneity centered at the reference system's origin whose distribution function reads:

$$\boldsymbol{\zeta}_i(\mathbf{x}_i) = \begin{cases} 107051.0 & \text{for} \quad \left\{\mathbf{x}_i \in V | \sqrt{y_{i1}^2 + y_{i2}^2 + y_{i3}^2} \leq 0.2\right\} \\ 9722.0 & \text{for} \quad \left\{\mathbf{x}_i \in V | \sqrt{y_{i1}^2 + y_{i2}^2 + y_{i3}^2} > 0.2\right\}. \end{cases} \tag{3.63}$$

	30	60	120
sph.	$82 \cdot 10^{-15}$	$122 \cdot 10^{-15}$	$95 \cdot 10^{-15}$
cyl.	$122 \cdot 10^{-15}$	$136 \cdot 10^{-15}$	$81 \cdot 10^{-15}$

Tab. 3.1: Δ_{FFT} for spherical and cylindrical inhomogeneity and different number af sample points in one direction.

The third one with a cylindrical inhomogeneity aligned along the x_3-direction and a distribution function:

$$
\boldsymbol{\zeta}_i(\mathbf{x}_i) = \begin{cases} 107051.0 & \text{for} \quad \left\{ \mathbf{x}_i \in V \,|\, \sqrt{y_{i1}^2 + y_{i2}^2} \leq 0.2 \right\} \\ 9722.0 & \text{for} \quad \left\{ \mathbf{x}_i \in V \,|\, \sqrt{y_{i1}^2 + y_{i2}^2} > 0.2 \right\}. \end{cases} \tag{3.64}
$$

The values 107051.0 and 9722.0 are typical values for the Lamé coefficient λ for steel and for concrete, respectively, and later on are used in simulations. The spherical and cylindrical inhomogeneity are also typical examples used in later simulations, and therefore have been chosen here. Each of the three distribution functions is evaluated at N^3 sample points, and sets are produced for $N = \rho \cdot 10$ with $\rho \in [1, 25]$. The operation (3.61) is called transformation cycle from now on. Each of the produced data sets is subjected to n subsequent transformation cycles, and the error is checked after $n = 1$, $n = 2$, $n = 5$ and $n = 10$ cycles. The diagrams in figs. 3.2 to 3.4 show the average relative error

$$
e_{\text{av}} = \frac{1}{N} \sum_{i=1}^{N^3} \frac{|\zeta_i^* - \zeta_i|}{\zeta_i} \tag{3.65}
$$

and the maximum relative error in each data set

$$
e_{\text{max}} = \max \left\{ |\zeta_i^* - \zeta_i| / \zeta_i \,|\, i \in \left[1, N^3\right] \right\}. \tag{3.66}
$$

Comparing fig. 3.2 with fig. 3.3 and fig. 3.4 it is seen that the relative error for the constant function is approximately lower by a factor of 100, which is not surprising because of the simplicity of the problem. The constant function has been evaluated in order to serve as a first reference. The relative errors for the cylindrical inhomogeneity (fig. 3.4) are slightly lower than for the spherical one (fig. 3.3), but both are of the same order of magnitude. Although the relative error oscillates with increasing N, the overall trend from all three cases is clearly an increasing error for increasing N. The irregularities in the global trend may be due to rearrangement of the algorithm for certain N, but more probably this is simply the natural oscillation in error propagation. It has to be remembered that in (3.41), (3.42) and (3.60) the uncertainty is estimated, and not the actual error which may be considerably lower. The general pattern of data distribution is similar irrespective of the number of subsequent transformations, only the scale on the abscissa changes. In fig. 3.5 the relative error is plotted against the number of transformations for two given N. Linear regression shows a correlation of more than 99% in both cases, and this behaviour is observed for all choices of N. This shows that the error propagation is almost linear, and the assumption in (3.62) is justified. In tab. 3.1 some exemplary values for the error after on transformation cycle are given in numeric form. They serve as basis to calculate the error that occurs after more than one iteration.
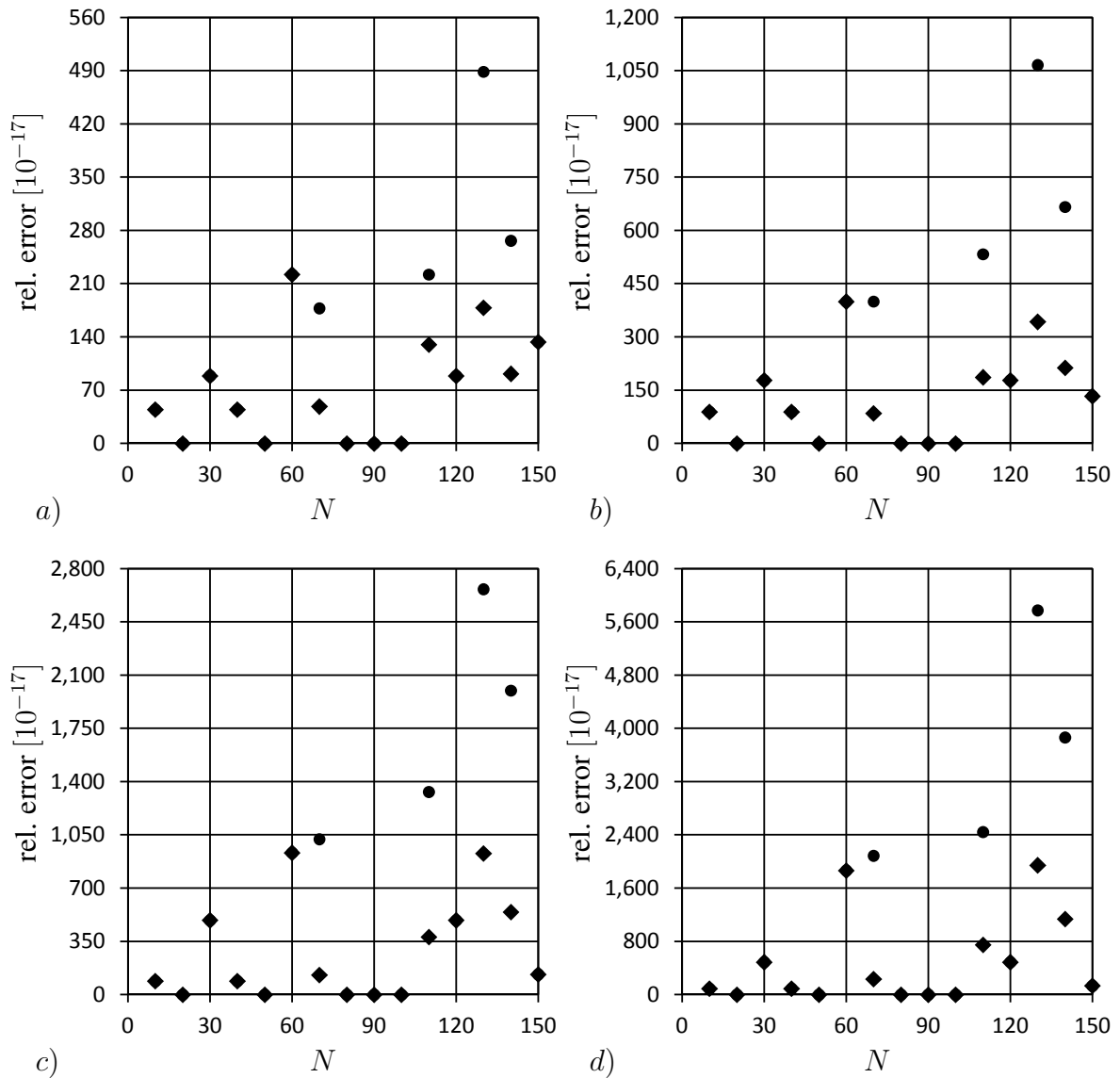
Fig. 3.2: Relative error $|\zeta^* - \zeta|/\zeta$ versus number of sample points for a constant function $\zeta = 1.0 \cdot 10^0$. One transformation cycle corresponds to one $\mathscr{FFT}$ and one $\mathscr{FFT}^{-1}$ transform. *a)* 1 transformation cycle *b)* 2 transformation cycles *c)* 5 transformation cycles *d)* 10 transformation cycles. The diamond points correspond to the average relative error and the points to the maximum relative error in the data set.
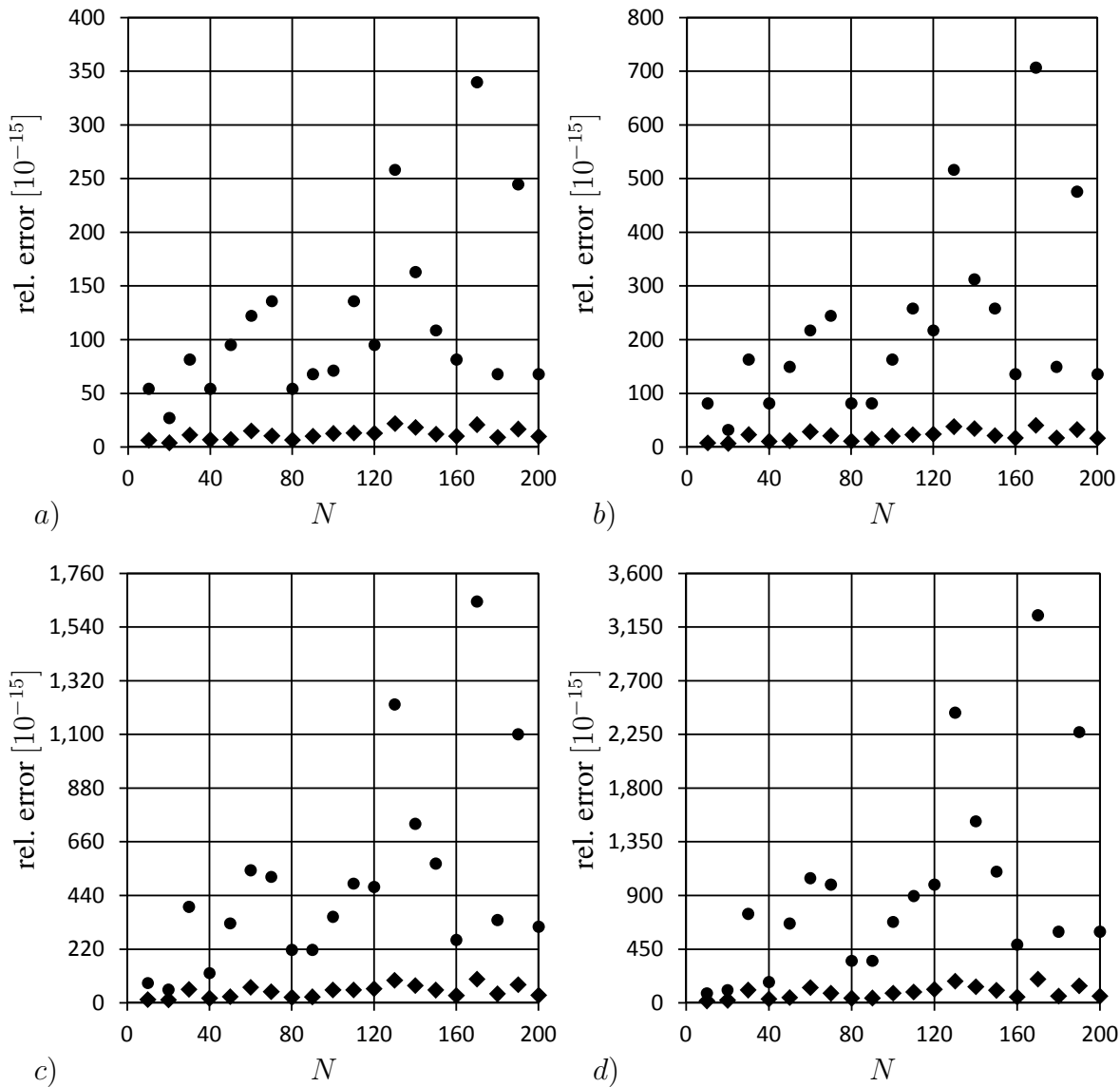
Fig. 3.3: Relative error $|\zeta^* - \zeta|/\zeta$ versus number of sample points for a spherical inhomogeneity. One transformation cycle corresponds to one $\mathscr{FFT}$ and one $\mathscr{FFT}^{-1}$ transform. $a)$ 1 transformation cycle $b)$ 2 transformation cycles $c)$ 5 transformation cycles $d)$ 10 transformation cycles. The diamond points correspond to the average relative error and the points to the maximum relative error in the data set.
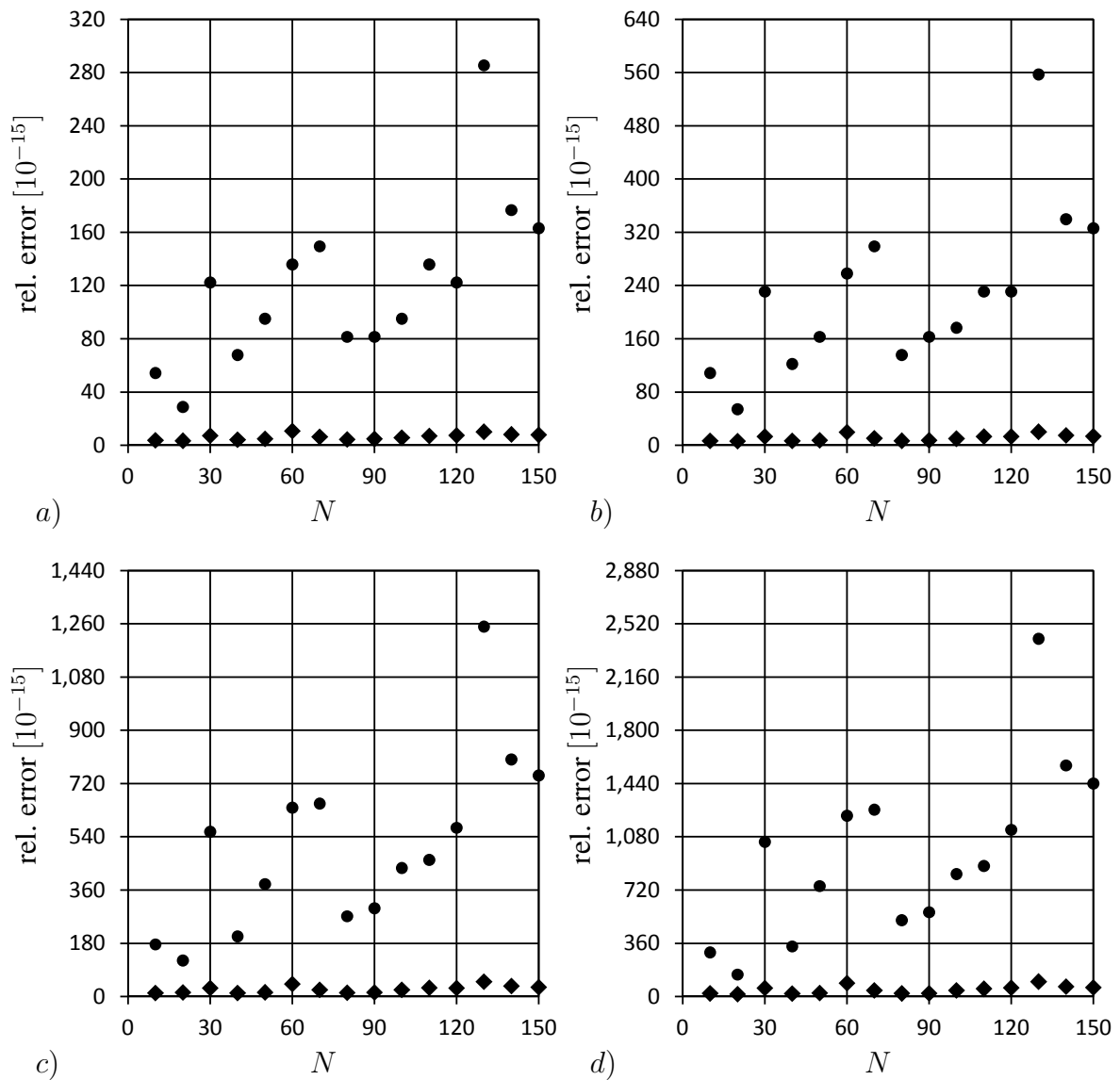
Fig. 3.4: Relative error $|\zeta^* - \zeta|/\zeta$ versus number of sample points for a cyclindrical inhomogeneity. One transformation cycle corresponds to one $\mathscr{FFT}$ and one $\mathscr{FFT}^{-1}$ transform. $a)$ 1 transformation cycle $b)$ 2 transformation cycles $c)$ 5 transformation cycles $d)$ 10 transformation cycles. The diamond points correspond to the average relative error and the points to the maximum relative error in the data set.
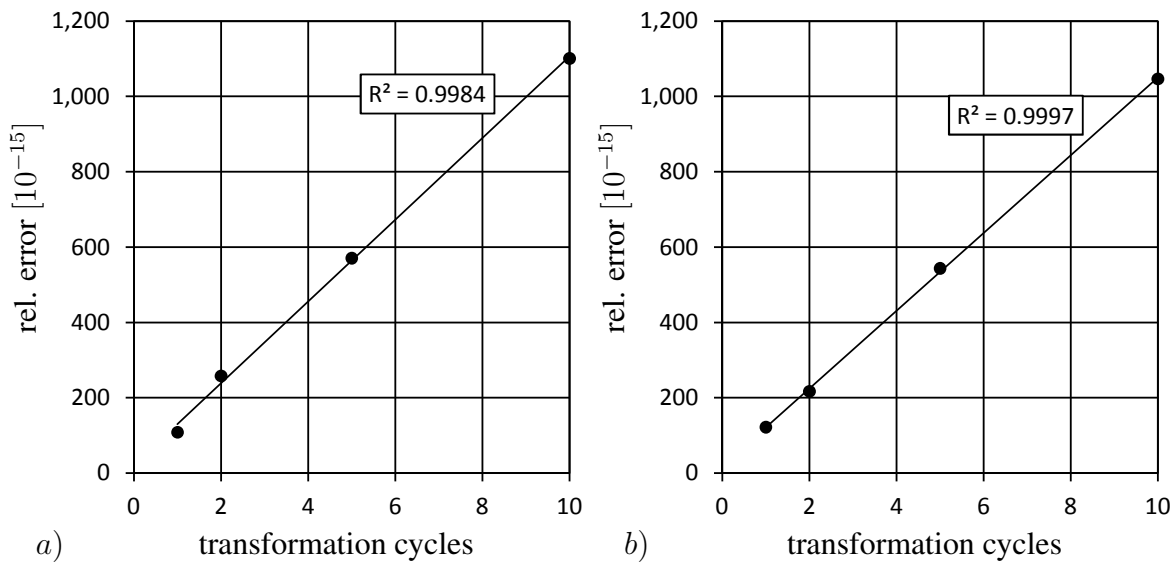
Fig. 3.5: Maximum relative error versus number of transformation cycles, for a cylindrical inclusion (see fig. 3.4, also). Solid line represents linear regression curve, R^2 is the correlation factor. $a)$ $N = 60$, $b)$ $N = 150$

The operator $\boldsymbol{\Gamma}^0(\boldsymbol{\xi})$ has to be calculated according to formula (3.6). The terms of the kind $\delta_{ij}\xi_k\xi_h$ in the brackets are not problematic, because they are products of integer numbers and the results should be exact. But the terms $\frac{1}{4\mu^0|\boldsymbol{\xi}|^2}$ and $\frac{\lambda^0+\mu^0}{\mu^0(2\mu^0+\lambda^0)}\frac{\xi_i\xi_j\xi_k\xi_l}{|\boldsymbol{\xi}|^4}$ are prone to yield considerable errors because they consist of complex operations on real numbers. As mentioned earlier, no information is available about the applied internal algorithm for the division of real numbers, thus again a numerical simulation is chosen to determine the uncertainty. For this purpose $\boldsymbol{\Gamma}^0$ is once calculated with 8 byte accuracy (the result labeled with Γ_8) and once with 16 byte accuracy (Γ_{16}), which means 32 digits available. Both results are compared and the relative difference between both is calculated:

$$e_{max} = \frac{\Gamma_8 - \Gamma_{16}}{\Gamma_{16}}. \tag{3.67}$$

The results may depend on the number of sample points in one direction N, because more terms to calculate give higher chance of errors, but the error may as well be lower for all high frequency terms.

Several simulations have been executed with different settings for λ^0 and μ^0. The results are plotted in figs. 3.6 and 3.7. It becomes clear immediately that below $N = 200$ the relative error remains nearly constant. It stays in the same order of magnitude (10^{-16}) which is very close to 8 byte accuracy. But for a resolution higher than $N = 200$ the error increases rapidly, for as much as four orders of magnitude in one case. This means that the high frequency terms in $\boldsymbol{\Gamma}^0$ are considerably flawed. In trial runs of algorithm (3.8) it is observed that the iteration becomes instable for a resolution close to $N = 200$, expressing itself through the fact that convergence is lost and the fixed point starts to act repulsive. It is very likely that the origin for this instability lies in the inaccurate calculation of $\boldsymbol{\Gamma}^0$. High values for μ^0 are beneficial, as can be seen from figs. 3.7c) and 3.7d), which have been given as linear rather than logarithmic plots. The error for high N is considerably smaller than in the other cases, yet still the sudden increase at $N = 200$ is observed. The uncertainty for $\lambda^0 = 100000$ and $\mu^0 = 75000$ at different sample rates is given in tab. 3.2. Comparison of table 3.2 with table 3.1 reveals that the uncertainty in $\boldsymbol{\Gamma}^0$ is far smaller than the uncertainty of the fast Fourier transform in the range of sample numbers $N < 128$ that is relevant to our simulations.

	30	60	120
Δ_Γ	$0.11 \cdot 10^{-15}$	$0.11 \cdot 10^{-15}$	$0.11 \cdot 10^{-15}$

Tab. 3.2: Δ_Γ for different number of sample points in one direction.

With the results from table 3.1, table 3.2, (3.58) and (3.40) the uncertainty for one iteration of an example with spherical inclusion, and a sample rate $N = 60$ can be estimated as

$$\Delta_{60} = 1.23 \cdot 10^{-13}. \tag{3.68}$$

After ten and hundred iterations, respectively:

$$10 \cdot \Delta_{60} = 1.23 \cdot 10^{-12}, \tag{3.69}$$
$$100 \cdot \Delta_{60} = 1.23 \cdot 10^{-11}. \tag{3.70}$$

Even after 100 iterations the relative error should be below 10^{-10}. In almost all cases of purely elastic behavior it was observed that less than ten iterations are necessary. However,

this depends on the choice of the convergence criterion (3.10). Typical choices for this parameter are 10^{-4} or 10^{-3}, thus far away still from the precision that is allowed by numerical uncertainty. It has to be pointed out that in the above analysis actual errors for certain examples have been calculated, and the uncertainty has simply been chosen to be the same. This is not true in an exact sense, since the actual error may well underestimate the overall uncertainty, and usually this is the case. Additionally, only a limited number of examples could be analyzed. However, the uncertainty usually should be of the same order of magnitude as the actual errors that occur, especially when several tests are considered. The data available so far suggests that the discrete Fourier transform is the dominant source of round off errors (order of magnitude is 10^{-13} compared to 10^{-15} for the other sources), and that a high sample point frequency N leads to numerical instabilities. These conclusions match well with the observation made with numerous examples where the proposed algorithm was used. For applications where a high number of sample points is used, e.g. when data from micrography is obtained, tabulated values for Γ_0 might be used to increase the stability of the algorithm.
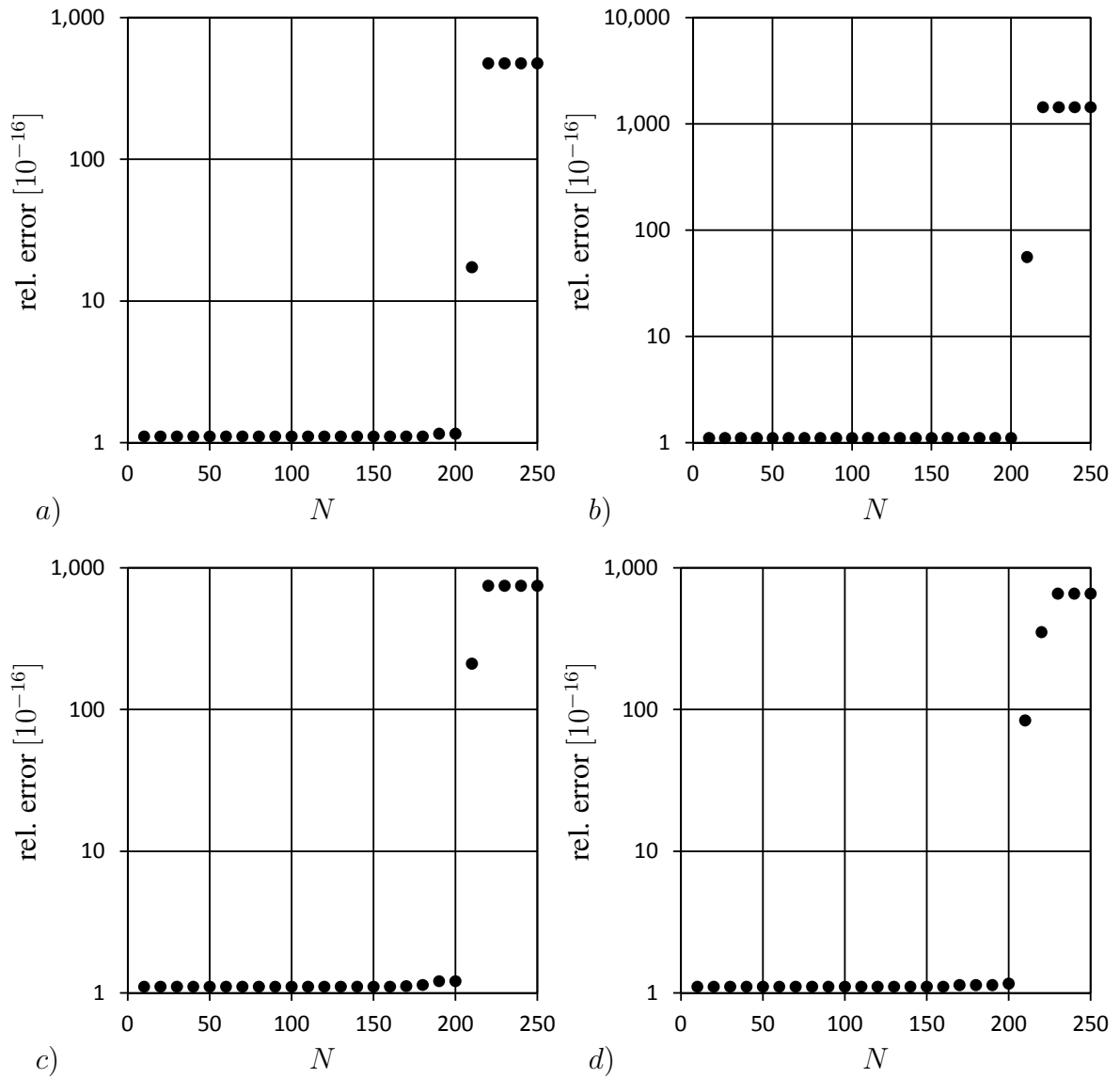
Fig. 3.6: Relative difference between results for $\mathbf{\Gamma}^0$ calculated with 8 byte and with 16 byte arithmetic, respectively. Settings for reference parameters: $a)\lambda^0 = 100000$, $\mu^0 = 75000$, $b)\lambda^0 = 64000$, $\mu^0 = 48000$, $c)\lambda^0 = 51200$, $\mu^0 = 38400$, $d)\lambda^0 = 40960$, $\mu^0 = 30720$
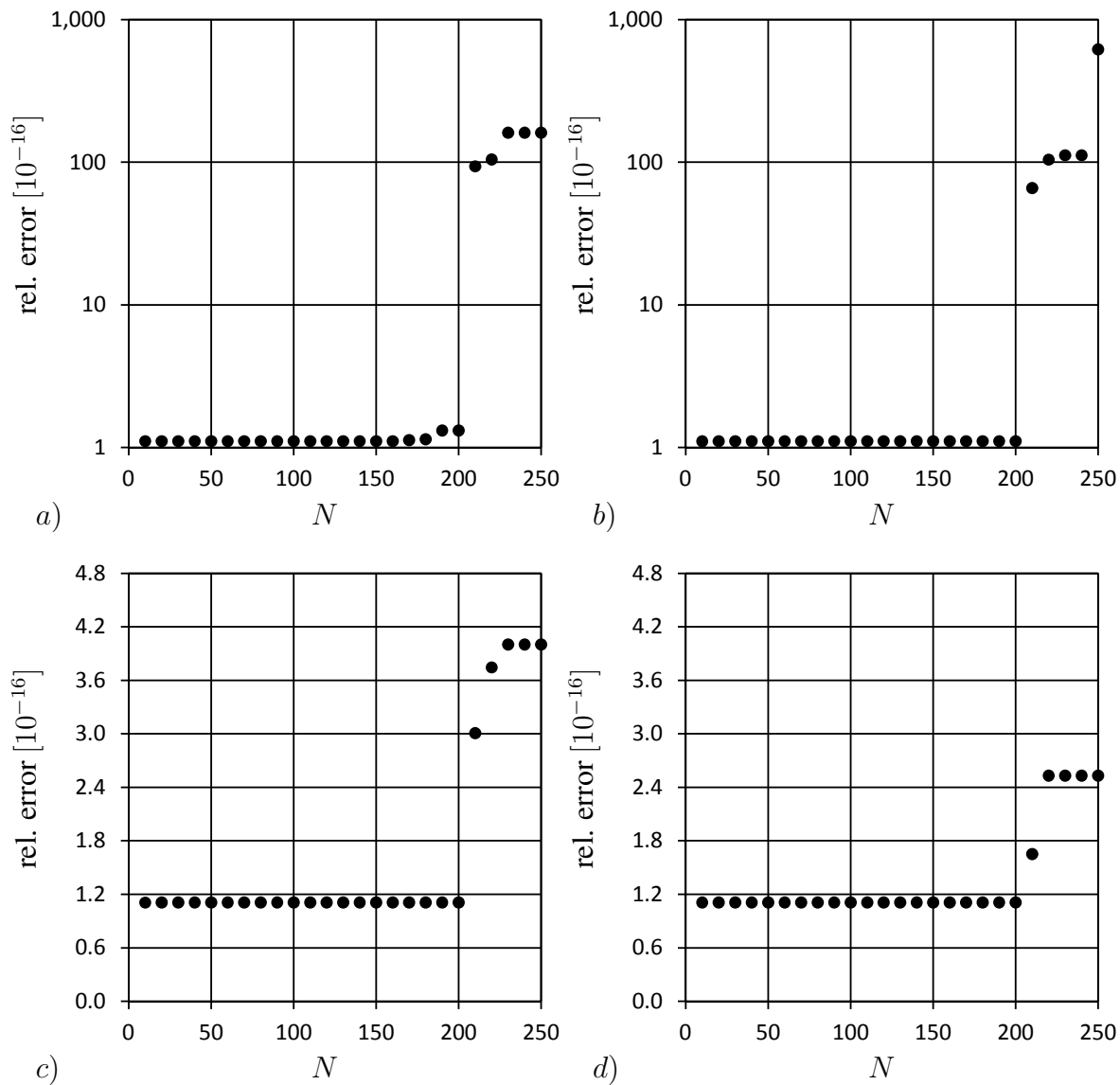
Fig. 3.7: Relative difference between results for $\mathbf{\Gamma}^0$ calculated with 8 byte and with 16 byte arithmetic, respectively. Settings for reference parameters: $a)\lambda^0 = 100000$, $\mu^0 = 25000$, $b)\lambda^0 = 100000$, $\mu^0 = 50000$, $c)\lambda^0 = 100000$, $\mu^0 = 100000$, $d)\lambda^0 = 100000$, $\mu^0 = 125000$

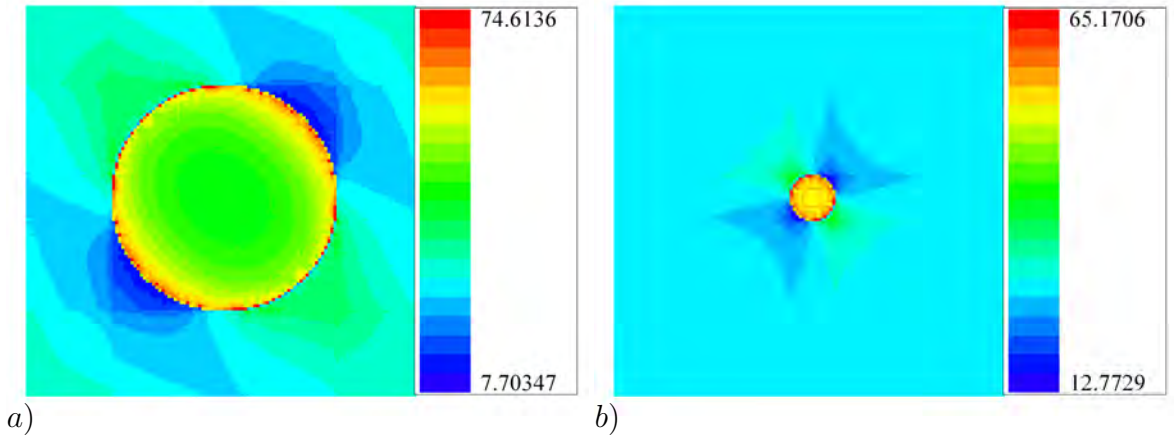### 3.3.2 Error Resulting From Discretisation and Truncation

Fig. 3.8: Results for shear stress σ_{12} for inhomogeneities with different radii. The normal vector to view plane is $(0, 0, -1)^{\mathrm{T}}$

A general issue in numerical treatment of partial differential equations is the error that originates in the discretization of the problem: the geometry, and in time-dependent problems also the time, are represented by a system of discrete objects, either the elements in Finite Element of Boundary Element Methods, or sample points in Finite Difference of FFT based methods. The discrete system can only be an approximation of the problem at hand, and the solution of the numerical problem at best approximates the original solution. The problem is two-fold: first, an error may come from the non-exact representation of the geometry, second, the discrete system may not be able to adequately interpolate the solution. In fig. 3.8 two examples with similar geometry are shown. A sphere is embedded in a matrix with softer material. The representative volume element is subjected to periodic strain boundary conditions with an average strain of:

$$\langle \boldsymbol{\epsilon} \rangle = 1\mathbf{e}_i \otimes \mathbf{e}_j. \tag{3.71}$$

The microstructure is sampled with $N = 128$ points in each direction, and the elastic response is calculated with the original Suquet algorithm (3.8). This is an approximation of the Eshelby problem discussed in sec. 2.3.1. More details on these simulations follow in sec. 4.1. In fig. 3.8 the shear stress σ_{12} is shown for two examples with different sphere radii. The view-plane is perpendicular to the normal vector $\mathbf{n} = (0, 0, 1)^T$, i.e. perpendicular to the x_3-axis. The equidistant sample points are not able to completely incorporate the curved geometry of the sphere, and the numerical algorithm cannot distinguish the curved geometry from a polygon geometry. In the exact solution stress singularities may occur at these edges, which cannot be interpolated by the numerical solution either. Nevertheless stress peaks occur at the edges. These can be observed in fig. 3.8 as the red zone close to the border between sphere and matrix. The smaller the radius of the sphere, the higher the influence of this error on the overall solution. The error can be mitigated with an increased sampling rate compared to the sphere radius, which is what happens also if the sphere radius is increased. A higher sample rate can better approximate the solution, but comes along with an increased number of edges in the geometric representation. A break-even may occur where the error resulting from the increased number of edges outweighs the accuracy gained with a better approximation of the geometry. For regular geometries with curved phase boundaries more degrees of freedom are necessary in the FFT based method than in Finite Element Methods. This was also reported by Moulinec and Suquet [106]. The strength of this algorithm lies

in the ability to model complex, irregular microstructures with less degrees of freedom than the FEM.

The second problem, i.e. the insufficiency of the discrete system to interpolate the solution, is especially inherent to the use of FFT based algorithms to simulate micro structural behavior. As pointed out in sec. 2.7, the frequency of the sample rate has to be twice as high as the highest frequency present in the original data, but discontinuous jumps do not have such a cut off frequency. Jumps in the spatial distribution of material constants are a natural feature of two or multiple phase composites. Thus this kind of error is not avoidable, in contrast to other methods, e.g. the FEM. In fig. 3.9 the problem is visualized again for the sphere in matrix geometry, for different sample rates. The original sampled data is displayed next to the two dimensional graph of the trigonometric interpolation polynomial, with the DFT used to calculate the coefficients of the polynomial. It is observed that the interpolation oscillates around the constant function that should describe the parameters. This comes from the fact that the interpolation lacks frequencies high enough to reconstruct the exact original data. This effect is well known also from other fields where the DFT is applied [111]. In the algorithm (3.8) this effect matters when the derivatives of the stress field are calculated:

$$\mathrm{div}\boldsymbol{\sigma} = \mathrm{div}\left(\mathbf{C}(\mathbf{x}) : \boldsymbol{\epsilon}(\mathbf{x})\right). \tag{3.72}$$

Since there is no cut off frequency, this error can only be mitigated but not be avoided. In fig. 3.9 the results for different resolutions are shown to demonstrate that the oscillations become ever smaller the higher the sample rate is, and for $N = 18$ a satisfying accuracy was observed in numerous simulations.

Another source of uncertainty is the truncation error, which is related to the last described problem. In the original problem the iteration is stopped when the quantity (3.9) is smaller than a prescribed value. The limit has to be chosen according to the required accuracy. Of course, the calculation of e is subject to round off errors as well as all other quantities, and in addition may be flawed by the lack of sample frequencies, since it is based on the derivatives of $\boldsymbol{\sigma}(\mathbf{x})$. The consequence is that the fixed point may belong to a non zero stress divergence in the discretized problem, and if the limit e is chosen too small the iteration may never stop at all. A work around can be that not the balance of linear momentum itself is checked but the difference between e^i and e^{i+1} belonging to two subsequent iterations:

$$e_{\mathrm{crit}} = |e^{i+1} - e^i|. \tag{3.73}$$

Care has to be taken also with this choice, since a small e_{crit} may indicate proximity to the fixed point or simply slow convergence of the algorithm. The last phenomenon occurs in the enhanced damage model in cases when the damaged zone has propagated to a certain size. The sole use of e_{crit} may lead the algorithm to stop although the iteration is still far away from a good approximation of the solution. The decision therefore was to use a combination of both criteria, the one suggested by Suquet (3.9) and (3.73).
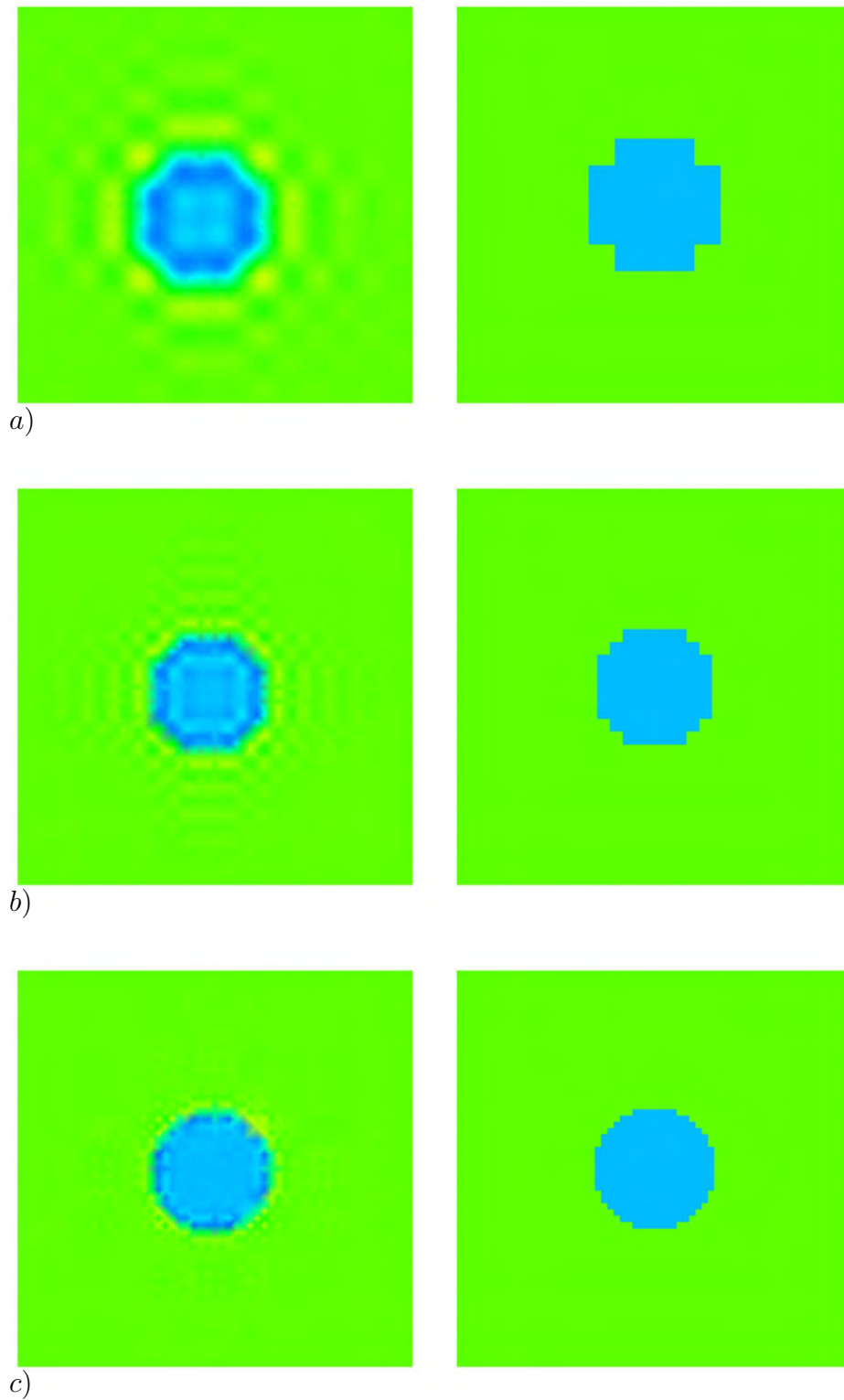
Fig. 3.9: Examples on trigonometric interpolation of a 2D circle using different sample point rate. On the right side the original data is shown, and on the left side the interpolation polynomial is visualized.

3.4 Advantages of the Algorithm

In the previous two sections possible flaws connected to the FFT based algorithm were analyzed. This is important to get a good idea about the reliability of results obtained with it, and to be able to adjust the limits of the numerical method. The uncertainty due to machine number arithmetic have been estimated and demonstrated to be within limits that do not interfere with the desired accuracy. The cut off criterion has been advanced in order to optimize the method. The problem of increased number of degrees of freedom compared to FEM for regular microstructures is qualified less important in damage simulation, since the propagation damage in fact produces an irregular microstructure, and one would need to adjust the number of elements in FEM in order to meet the requirements.

4 Validation of Model Behavior

	$Y[\mathrm{MPa}]$	ν	$\lambda[\mathrm{MPa}]$	$\mu[\mathrm{MPa}]$
steel	200000	0.29	107051	77519
concrete	35000	0.20	9722	14583

Tab. 4.1: Mechanical properties of steel and concrete: Young's Modulus Y, Poisson Ratio ν, Lamé-parameters λ and μ

4.1 Comparison of Results to Eshelby Solution

The results obtained with the numerical algorithm are compared to the closed form solution by Eshelby, see sec. 2.3.1. This has to be done in order to prove the correctness of the implementation on a computer. In addition, information can be gained about the general quality of the results, and its dependence on resolution and other parameters. The Eshelby problem is very adept for this purpose because of the simplicity of the results, at least of parts of it. It has been said in sec. 2.3.1 that the stresses inside a spherical inhomogeneity of stiffness $\mathbf{C}^I$ embedded in an infinite medium of stiffness $\mathbf{C}^0$ subjected to a far field strain $\boldsymbol{\epsilon}^0$ are constant, and can be calculated according to (2.56), which is repeated here:

$$\boldsymbol{\sigma}^0 + \boldsymbol{\sigma} = \mathbf{C}^{\mathrm{D}} : \left[\mathbf{S} : \mathbf{M}^D : \left(\mathbf{C}^I - \mathbf{C}^0 \right) + \mathbf{I} \right]^{-1} : \boldsymbol{\varepsilon}^0.$$

The FFT-based algorithm is only applicable in cases where a periodic structure of a two phase composite is assumed, which means an infinite number of equidistantly spaced spherical inhomogeneities instead of one inhomogeneity embedded in an infinite solid. Results should differ in general because the inhomogeneities interact with stress disturbances of neighboring particles. However, it is fair to assume that interaction is low for a low volume fraction of the embedded phase, and thus the numerical results obtained for small sphere radii can be expected to be close to the Eshelby solution (2.56). The statement of the classical problem starts with the assumption of a constant far field stress, contrary to the situation when the numerical algorithm is executed, where an average strain is predefined, but this does not make a difference in fact, since far field strain and far field stress are linked uniquely via Hooke's law (2.9) to each other. Calculations have been carried out with a spherical inhomogeneity positioned at the center of the RVE, as shown in fig. 4.1. The stiffness parameters λ and μ have been chosen according to the data in tab. 4.1, with steel being assigned to the spherical region and concrete assigned to the rest. If the origin of the coordinate system is located at the center of the RVE, and the edge length of the RVE is chosen to be 1, than a sphere with radius r centered in the RVE is mathematically described by the set:

$$\Omega_{\mathrm{Sphere}} = \left\{ \mathbf{x} \in V | x_1^2 + x_2^2 \leq r^2 \right\}. \tag{4.1}$$
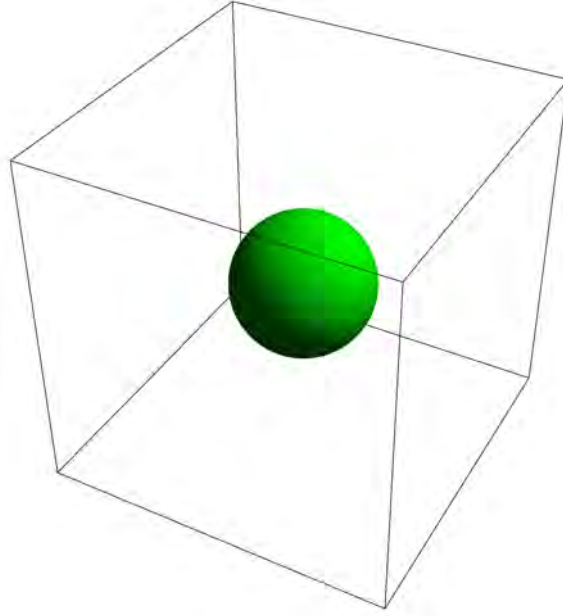
Fig. 4.1: A sphere located at the center of the RVE

For the tests a set of similar geometries was used that differed only in the radius of the sphere. Nine different volume concentrations from $c = 0.002$ to $c = 0.15$ have been chosen, as indicated in the first column of tab. 4.2. The radius of the sphere is linked to the volume fraction by

$$r = \sqrt[3]{\frac{3}{4}\frac{c}{\pi}}. \tag{4.2}$$

The corresponding radii are listed in the second column of tab. 4.2. For each radius a sampled, three dimensional RVE has been generated, with a sample point rate in one direction of $N = 128$. The data is generated by scanning the $N^3 = 2097152$ points $\mathbf{x}_\nu$ and assigning each a value by evaluating the functions

$$\lambda(\mathbf{x}_\nu) = \begin{cases} 107051 & \text{if} \quad \mathbf{x}_\nu \in \Omega_{\text{Sphere}} \\ 9722 & \text{if} \quad \mathbf{x}_\nu \notin \Omega_{\text{Sphere}} \end{cases} \tag{4.3}$$

and

$$\lambda(\mathbf{x}_\nu) = \begin{cases} 77519 & \text{if} \quad \mathbf{x}_\nu \in \Omega_{\text{Sphere}} \\ 14583 & \text{if} \quad \mathbf{x}_\nu \notin \Omega_{\text{Sphere}} \end{cases}. \tag{4.4}$$

The first of two test series is run with pure shear deformation:

$$\langle \boldsymbol{\epsilon} \rangle^{0S} = \left(0, 0, 0, \frac{1}{2}, 0, 0 \right)^T. \tag{4.5}$$

If $\langle \boldsymbol{\epsilon} \rangle^{0S}$ is taken as $\boldsymbol{\epsilon}^0$ in (2.56), then the stresswithin the inhomogeneity reads (predicted by Eshelby)

$$\boldsymbol{\sigma}^0 + \boldsymbol{\sigma} = (0, 0, 0, 49.1\,\text{MPa}, 0, 0)^T \tag{4.6}$$

in Voigt notation. The second series is subjected to a tensile load

$$\langle \boldsymbol{\epsilon} \rangle^{0T} = (1, 0, 0, 0, 0, 0) \tag{4.7}$$

$c\,[-]$	$r\,[-]$	$\boldsymbol{\epsilon}^{0S}\,[-]$		$\boldsymbol{\epsilon}^{0T}\,[-]$	
		$\langle\sigma_{12}\rangle_\Omega$ [MPa]	σ_{12V} [MPa]	$\langle\sigma_{11}\rangle_\Omega$ [MPa]	σ_{11V} [MPa]
0.15	0.329	51.2	7.3	96.0	18.1
0.10	0.288	49.8	5.4	91.6	12.8
0.05	0.229	49.0	4.0	87.9	11.1
0.01	0.134	49.6	2.8	85.4	9.7
0.008	0.124	49.8	2.6	85.3	9.6
0.006	0.113	50.0	2.7	85.3	9.5
0.004	0.098	50.4	2.7	85.2	9.4
0.002	0.078	50.9	2.8	85.2	9.1
cl. f.		**49.1**		**67.4**	

Tab. 4.2: Volume average of stress in spherical inhomogeneity for different geometries: results from numerics and closed form solution [44]

yielding by substitution into (2.56)

$$\boldsymbol{\sigma}^0 + \boldsymbol{\sigma} = (67.4\,\mathrm{MPa}, 18.3\,\mathrm{MPa}, 18.3\,\mathrm{MPa}, 0, 0, 0)^T. \tag{4.8}$$

For each geometry the numerical solution is carried out for $\langle\boldsymbol{\epsilon}\rangle^{0S}$ and for $\langle\boldsymbol{\epsilon}\rangle^{0T}$ respectively. Because of the periodic nature of the DFT and the equations upon which the algorithm is based the stresses and strains will not be constant within the inhomogeneity. Second, the discretization error already described in sec. 3.3.2 leads to stress peaks at the boundary between inhomogeneity and surrounding material. This can be seen in the figures 4.2 and 4.3, where the red color at the boundary indicates high stresses, because the sample point grid cannot capture the smooth surface of the sphere. Fig. 4.2a) to f) show the shear stress distribution $\sigma_1 2$ for six out of nine different geometries subjected to $\langle\boldsymbol{\epsilon}\rangle^{0S}$, and fig. 4.3a) to f) shows the distribution of σ_{11} for six tests where $\langle\boldsymbol{\epsilon}\rangle^{0T}$ was applied. In order to compare the numerical results to (4.6) and to (4.8), the stresses are averaged over the volume of the sphere Ω_{Sphere}. The integrals are averaged as

$$\langle\sigma_{12}\rangle_{\Omega_{\mathrm{Sphere}}} = \int_{\Omega_{\mathrm{Sphere}}} \sigma_{ij}\,\mathrm{d}\mathbf{x} \approx 1/N_{\mathrm{S}} \sum_{\nu=1}^{N_{\mathrm{S}}} \sigma_{ij}(\mathbf{x}_\nu), \tag{4.9}$$

with $\mathbf{x}_\nu \in \Omega_{\mathrm{Sphere}}$ and N_{S} being the number of sample points within the sphere. In tab. 4.2 the results for all eighteen tests are given, together with the corresponding volume concentration, radius and the closed form results for comparison. In addition, the statistical variance is given to get a feeling about the oscillation around the average within the inhomogeneity. The variance is calculated as:

$$\sigma_{ij\mathrm{V}} = \frac{1}{N_{\mathrm{S}}} \sum_{\nu=1}^{N_{\mathrm{S}}} \left(\langle\sigma_{12}\rangle_{\Omega_{\mathrm{Sphere}}} - \sigma_{12}(\mathbf{x}_\nu)\right)^2. \tag{4.10}$$

When $\langle\boldsymbol{\epsilon}\rangle^{0S}$ is applied, the results converge towards the exact solution if the radius becomes smaller. In fig. 4.2 it can be observed that the region where the stress field is disturbed by the presence of the inhomogeneity is considerably smaller than the RVE. This means that

the solution in one RVE is not influenced significantly by its neighboring RVE since only a nearly constant field reaches the boundary between both. Inspection of the three examples with the smallest radii ($r = 0.078, 0.098, 0.113$) suggests that the numerical results turns away from the exact solution, and the variance also starts to increase again. But this effect is very likely to originate in the discretization error that increases with decreasing radius as discussed in sec. 3.3.2. In fig. 4.2e) and f) it can be seen that the stress field within is of a more disturbed nature than for bigger examples.

The data for $\langle \epsilon \rangle^{0T}$ converges, too, but unfortunately towards a wrong value, something around $\langle \sigma_{11} \rangle = 85\,\mathrm{MPa}$. In fig. 4.3 it is observed that the stress field within Ω_{Sphere} is nearly constant, but not at the same level as Eshelby suggests. This is no reason to reject the results provided by the numerical algorithm presented here. It is rather more probable that the model does not approximate accurately the classical Eshelby problem. From fig. 4.3 it can be deduced that the stress disturbances reach well beyond the borders of the RVE, even for small radii, and the assumption of non-interaction has to be rated invalid in this context.

The reproduction of the Eshelby solution in case of applied shear deformation suggests that the algorithm works correctly in this case. The unsatisfying result that is obtained for tensile load is no reason to mistrust the algorithm, following the arguments just provided. In order to further check the validity, results have been compared to other closed form solutions, explained detailedly in the next section.
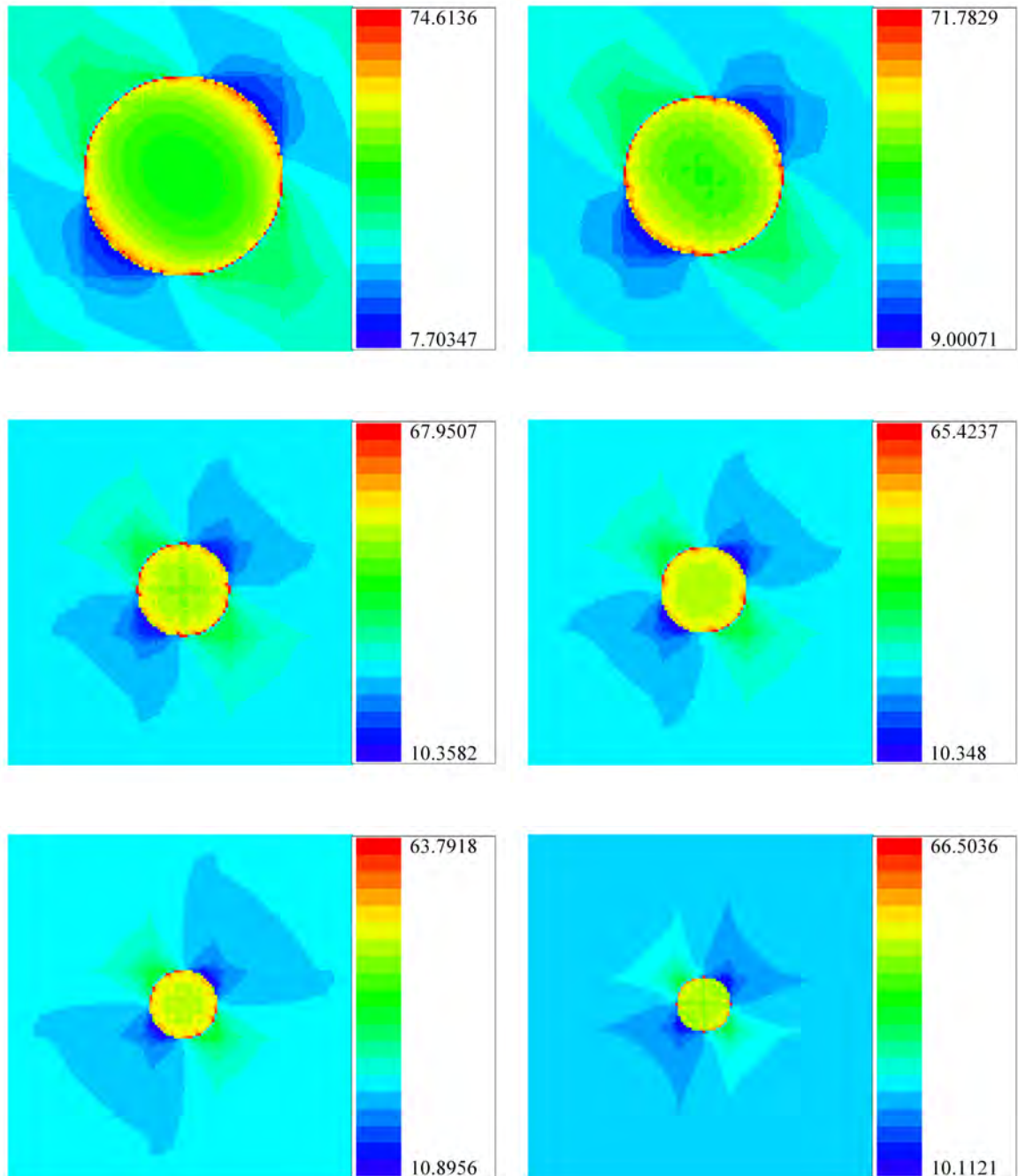
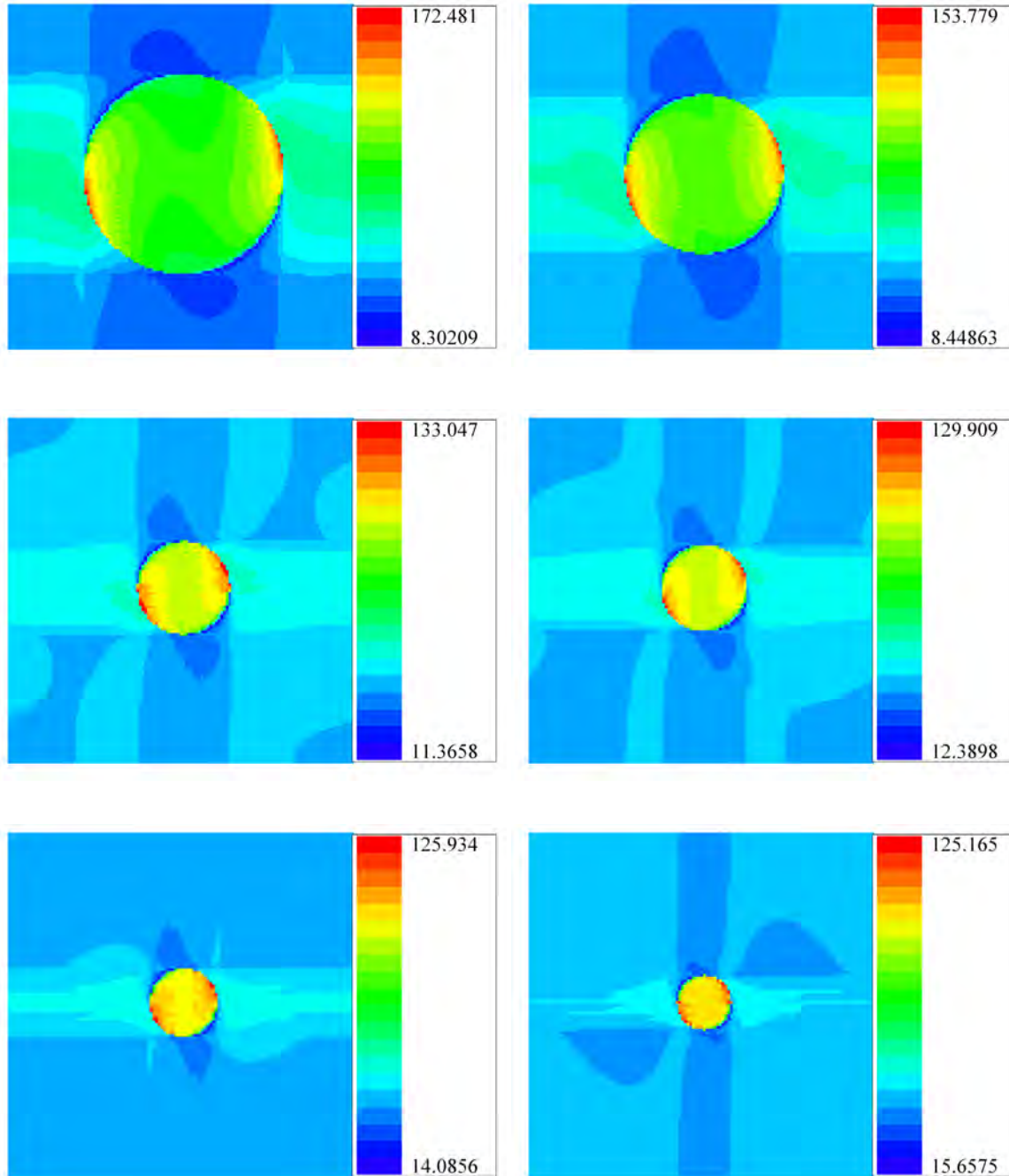Fig. 4.2: Distribution of σ_{12} shear stresses in a plane perpendicular to the x_3 axis.

Fig. 4.3: Distribution of σ_{11} tensile stresses in a plane perpendicular to the x_3 axis.
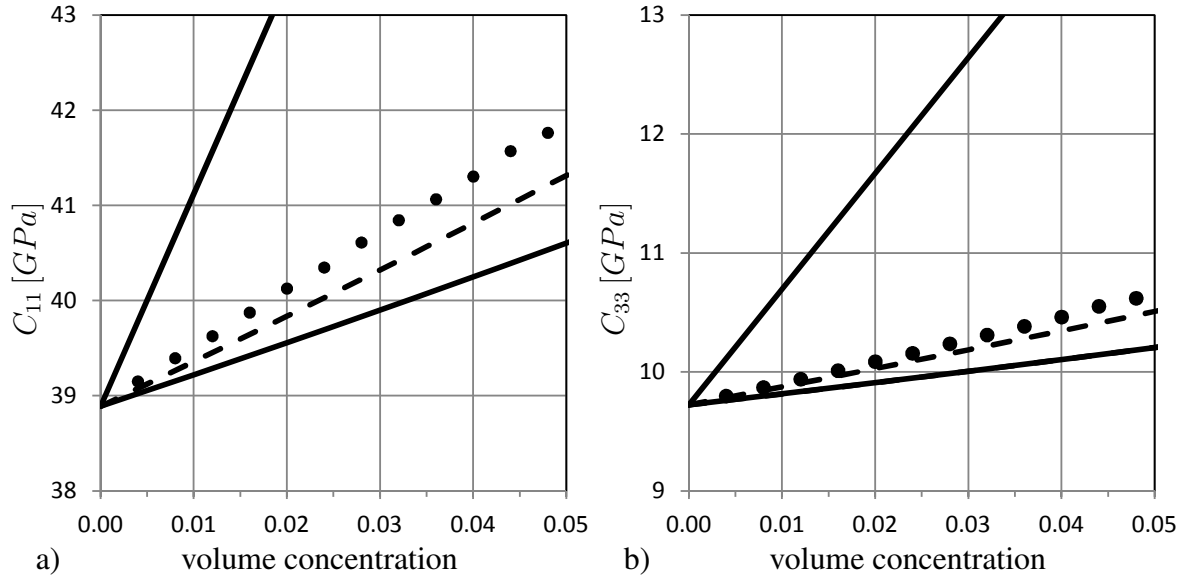
Fig. 4.4: Comparison of Suquet algorithm with Mori-Tanaka Method (dashed) and Reuss- and Voigt-bounds (solid) for an ellipsoidal inclusion (left: C_{11}, right: C_{13})

4.2 Comparison of Results to Mori-Tanaka Theory

In the previous section it was demonstrated that the algorithm, under certain circumstances, can reconstruct numerically the closed form interior solution (that means: the elastic field within the inhomogeneity) of the Eshelby problem. Since this is no rigorous proof of the correctness of the algorithm, more data supporting its validity is welcome. As mentioned in the introduction to this chapter, extensive testing is necessary to be sure about the correct implementation. The method described in sec. 4.2 compares the stresses within an inhomogeneity to the closed form solution. No information about the exterior fields is obtained. Various semi-closed-form solutions are available in the literature [74, 108], but they usually involve integral representations that have to be calculated numerically. Numerical uncertainty is high for them and thus it is difficult to verify the data obtained with the FFT-based algorithm with the solution obtained this way. Therefore a different approach has been chosen. For two sets of geometries the volume average of the stresses and strain fields are calculated. Since the data is given in sampled form, with N sample points in each coordinate direction, this is done the following way:

$$\langle \sigma_{ij} \rangle = \int_V \sigma_{ij} \, \mathrm{d}V \approx \frac{1}{N} \sum_{\nu=1}^{\nu=N^3} \sigma_{ij}(\mathbf{x}_\nu), \quad \text{and} \tag{4.11}$$

$$\langle \sigma_{ij} \rangle = \int_V \sigma_{ij} \, \mathrm{d}V \approx \frac{1}{N} \sum_{\nu=1}^{\nu=N^3} \sigma_{ij}(\mathbf{x}_\nu). \tag{4.12}$$

If all the components $\langle \sigma ij \rangle$ and $\langle \epsilon ij \rangle$ are calculated, the averaged tensorial expressions $\langle \boldsymbol{\sigma} \rangle$ and $\langle \boldsymbol{\epsilon} \rangle$ are constructed, and according to the definition (2.70) of the averaged Hooke's Law,

$$\langle \boldsymbol{\sigma} \rangle = \mathbf{C}_{\text{eff}} : \langle \boldsymbol{\epsilon} \rangle \, ,$$

some components of C can be determined. In general there are 21 independent components of C, and thus 21 equations are needed. It is clear that results for several loading conditions
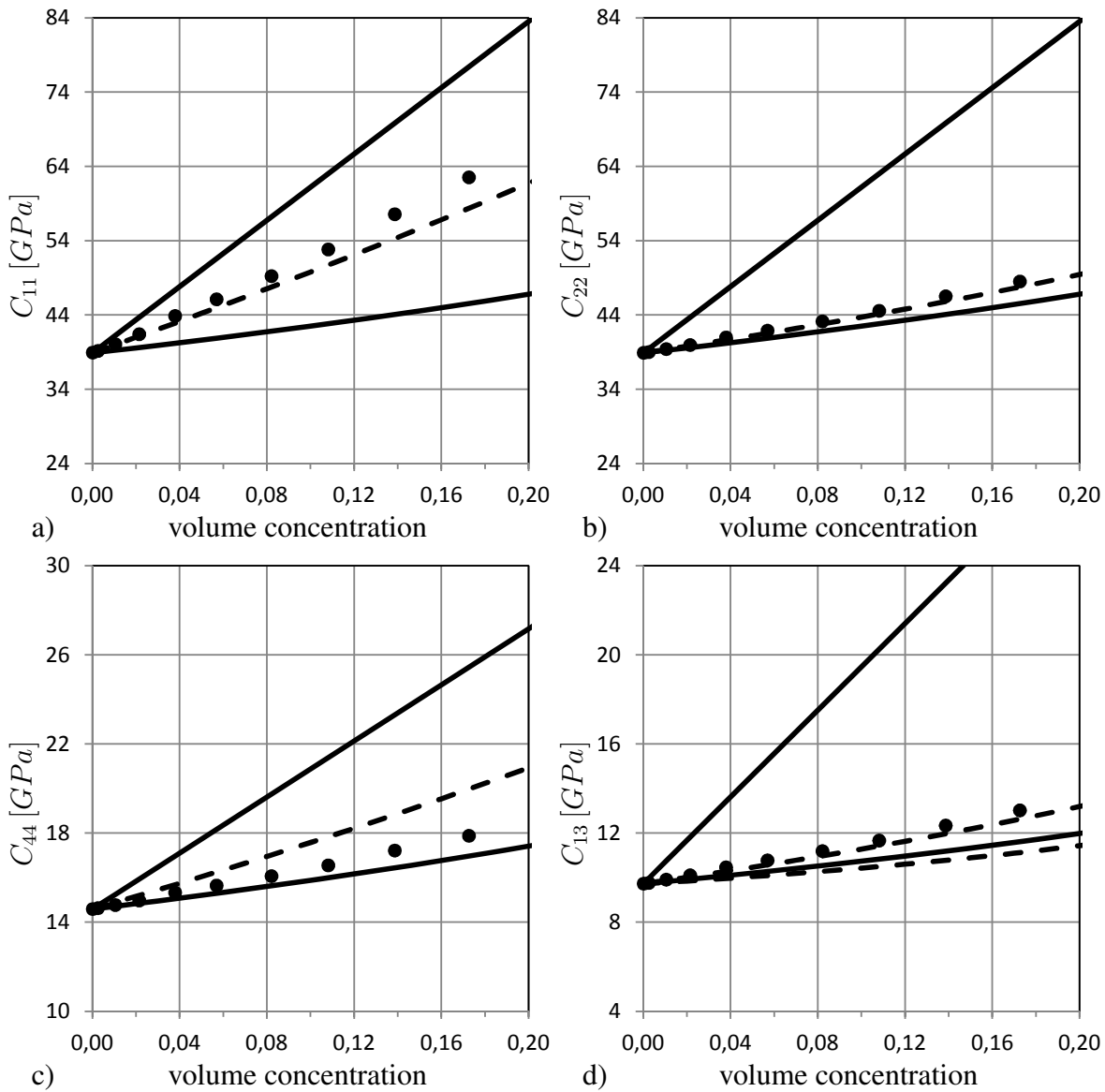
Fig. 4.5: Results for different components of the effective stiffness matrix obtained with Suquet (dot markers) compared to Voigt- and Reuss bounds, and to results obtained with Mori-Tanaka Method (dashed line). For the Mori-Tanaka Method two ellipsoids with ratios 1000:1:1 and 1:1:1000 for the half axes were assumed.

are needed to provide them. The question arises, whether or not the choice of loading conditions has an effect on the resulting effective stiffness. Hayes investigated in 1969 a statical method to uniquely determine the C_{ij} from statical experiment setups [65]. 21 experiments are necessary following his approach, and the components of $\mathbf{C}_{\text{eff}}$ are determined one by one. With respect to the situation in this project this means, that the elastic algorithm has to be executed 21 times and the results have to be evaluated each time. This method has been tested for several examples.

A rather more simple approach is the application of the six linearly independent strain states,
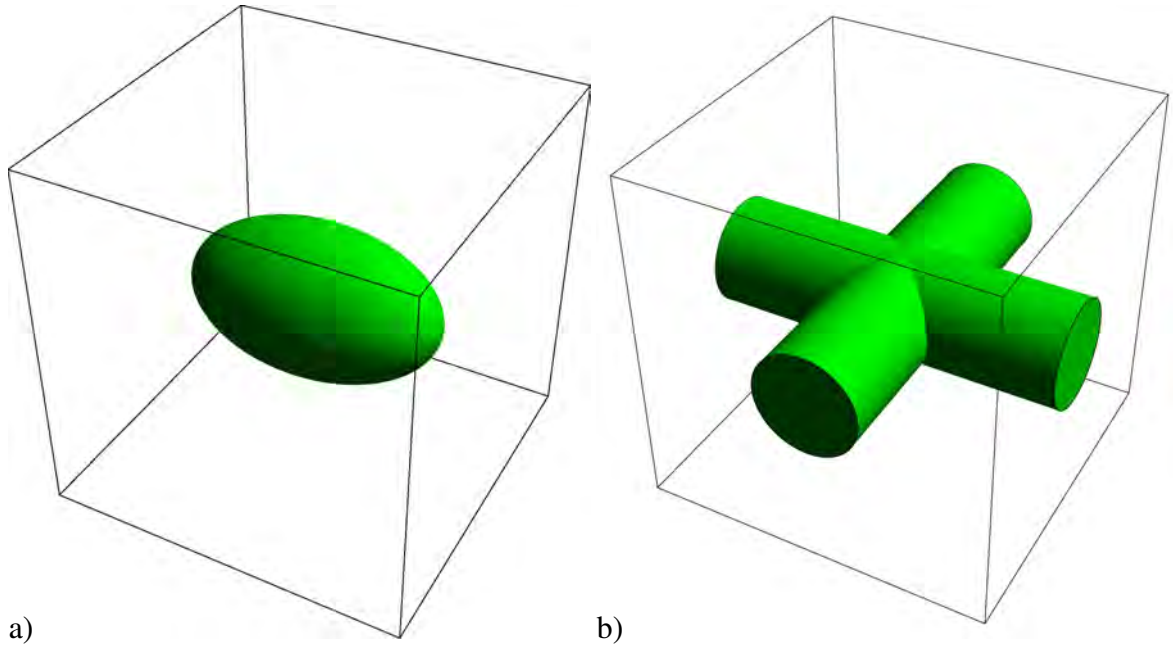
a) b)

Fig. 4.6: Representative volume element with a) embedded ellipsoidal inhomogeneity and b) lattice structure

given here in Voigt notation:

$$\langle \boldsymbol{\epsilon} \rangle^1 = (1, 0, 0, 0, 0, 0)^{\mathrm{T}} \tag{4.13}$$

$$\langle \boldsymbol{\epsilon} \rangle^2 = (0, 1, 0, 0, 0, 0)^{\mathrm{T}} \tag{4.14}$$

$$\langle \boldsymbol{\epsilon} \rangle^3 = (0, 0, 1, 0, 0, 0)^{\mathrm{T}} \tag{4.15}$$

$$\langle \boldsymbol{\epsilon} \rangle^4 = (0, 0, 0, \frac{1}{2}, 0, 0)^{\mathrm{T}} \tag{4.16}$$

$$\langle \boldsymbol{\epsilon} \rangle^5 = (0, 0, 0, 0, \frac{1}{2}, 0)^{\mathrm{T}} \tag{4.17}$$

$$\langle \boldsymbol{\epsilon} \rangle^6 = (0, 0, 0, 0, 0, \frac{1}{2})^{\mathrm{T}}. \tag{4.18}$$

For each strain state the resulting stress fields are calculated with the numerical algorithm, and is volume averaged with formula (4.12). By interpretation of Hooke's law (2.70) the components of $\mathbf{C}_{\mathrm{eff}}$ are read out as the averaged stress components:

$$\langle \boldsymbol{\sigma} \rangle^1 = \mathbf{C} \cdot \langle \boldsymbol{\epsilon} \rangle^1 = (C_{11}, C_{12}, C_{13}, C_{14}, C_{15}, C_{16})^T \tag{4.19}$$

$$\langle \boldsymbol{\sigma} \rangle^2 = \mathbf{C} \cdot \langle \boldsymbol{\epsilon} \rangle^2 = (C_{11}, C_{12}, C_{13}, C_{14}, C_{15}, C_{16})^T \tag{4.20}$$

$$\langle \boldsymbol{\sigma} \rangle^3 = \mathbf{C} \cdot \langle \boldsymbol{\epsilon} \rangle^3 = (C_{11}, C_{12}, C_{13}, C_{14}, C_{15}, C_{16})^T \tag{4.21}$$

$$\langle \boldsymbol{\sigma} \rangle^4 = \mathbf{C} \cdot \langle \boldsymbol{\epsilon} \rangle^4 = (C_{11}, C_{12}, C_{13}, C_{14}, C_{15}, C_{16})^T \tag{4.22}$$

$$\langle \boldsymbol{\sigma} \rangle^5 = \mathbf{C} \cdot \langle \boldsymbol{\epsilon} \rangle^5 = (C_{11}, C_{12}, C_{13}, C_{14}, C_{15}, C_{16})^T \tag{4.23}$$

$$\langle \boldsymbol{\sigma} \rangle^6 = \mathbf{C} \cdot \langle \boldsymbol{\epsilon} \rangle^6 = (C_{11}, C_{12}, C_{13}, C_{14}, C_{15}, C_{16})^T. \tag{4.24}$$

Both methods, the one just described and the one given by Hayes, have been run on several examples, and it was found out that both deliver results that are identical within the range of numerical uncertainty. Thus the simple method is advocated by the author due to its considerably reduced computation time. Two different sets of material data have been generated. One was an RVE with an embedded ellipsoidal inhomogeneity, as depicted in fig. 4.6a), and a ratio of half-axes of 1:1:3. Mathematically an ellipsoid of half axes a, a and $3a$ is described by the set:

$$\Omega_{\mathrm{Ell}} = \left\{ \mathbf{x} \in \mathcal{V} \,|\, \left(\frac{x_1}{a} \right)^2 + \left(\frac{x_2}{a} \right)^2 + \left(\frac{x_3}{3a} \right)^2 \right\} \tag{4.25}$$

The corresponding data was generated by evaluating sample point wise the functions

$$\lambda(\mathbf{x}_\nu) = \begin{cases} 107051\text{MPa} & \text{if} \quad \mathbf{x}_\nu \in \Omega_{\text{Ell}} \\ 9722\text{MPa} & \text{if} \quad \mathbf{x}_\nu \notin \Omega_{\text{Ell}} \end{cases} \tag{4.26}$$

and

$$\lambda(\mathbf{x}_\nu) = \begin{cases} 77519\text{MPa} & \text{if} \quad \mathbf{x}_\nu \in \Omega_{\text{Ell}} \\ 14583\text{MPa} & \text{if} \quad \mathbf{x}_\nu \notin \Omega_{\text{Ell}} \end{cases}. \tag{4.27}$$

The volume fraction c is chosen as an independent experiment parameter, and the parameter a is determined via the relationship

$$a = \sqrt[3]{\frac{c}{4\pi}}. \tag{4.28}$$

Data was generated for different volume concentrations, and for each volume concentrations the procedure described above to determine the effective properties is executed.

A second set of data has been produced with a more complex, lattice-like structure. An example is given in fig. 4.6. The mathematical description reads:

$$\Omega_{\text{Latt}} = \left\{ \mathbf{x} \in \mathbb{R}^3 \,\middle|\, x^2 + y^2 \leq r \vee y^2 + z^2 \leq r \right\} \tag{4.29}$$

and the point wise evaluated function is

$$\lambda(\mathbf{x}_\nu) = \begin{cases} 107051 & \text{if} \quad \mathbf{x}_\nu \in \Omega_{\text{Latt}} \\ 9722 & \text{if} \quad \mathbf{x}_\nu \notin \Omega_{\text{Latt}} \end{cases} \tag{4.30}$$

and

$$\lambda(\mathbf{x}_\nu) = \begin{cases} 77519 & \text{if} \quad \mathbf{x}_\nu \in \Omega_{\text{Latt}} \\ 14583 & \text{if} \quad \mathbf{x}_\nu \notin \Omega_{\text{Latt}} \end{cases}. \tag{4.31}$$

The relationship between the radius of the fibers and the volume fraction is not available in closed form because the intersection makes its calculation complex. As a work around a sequence of radii has been chosen, the geometry has been built up according to (4.29) (4.30) and (4.31) and the volume fraction has been calculated afterwards by counting the M sample points with assigned value $\lambda = 107051$ and calculating c by

$$c = \frac{1}{N^3} \sum_{\nu=1}^{M} 1. \tag{4.32}$$

The same procedure as for the ellipsoid examples is employed on the lattice RVE's.

In fig. 4.4 results are plotted for the exemplary components C_{11} and C_{33}. To estimate the validity of the results, the Voigt upper bound (2.72) and the Reuss lower bound (2.73) are also plotted, and the effective stiffness calculated with formula (2.77) from the Mori-Tanaka theory. It is observed that the Mori-Tanaka theory and results of the numerical algorithm are in very good agreement for low volume concentrations. With increasing concentration the difference between both approaches grows. This is probably due to the approximative character of the closed-form solution, which is based on the assumption, among others, that

different inhomogeneities do not interact. This assumption does only hold for low volume concentrations. For concentrations higher than 5% a comparison is no longer useful, since the main rotating axis of the ellipsoid grows too large to be in included in the volume element, and the numerical algorithm does no longer calculate results for ellipsoid particulates. For all concentrations the results are lying between Voigt and Reuss limit.

The results obtained with the lattice geometry are plotted in fig. 4.5a) to d). The Mori-Tanaka theory was not formulated for this case. However, if a sequence of ellipsoidal inhomogeneities, with the rotating axis converging to infinity, is considered, and the effective stiffness tensor is estimated according to Mori-Tanaka, it is fair to expect that the situation of a cylindrical inhomogeneity of infinite length is approximated. The Mori-Tanaka theory allows estimates for multi-phase composites, see [22], and if two ellipsoids with their main axes showing in directions perpendicular to each other are considered, with the length of their main axis converging to infinity, than the situation described with (4.29) may be approximated. This was done to generate the plots in fig. 4.5a) to d). The observations made here are basically the same as for the examples with the ellipsoidal inhomogeneities. The estimated stiffness properties all satisfy the Voigt and Reuss bounds, and lie fairly close to the Mori-Tanaka estimate.

These observations further indicate that the numerical algorithm works correctly, at least for the elastic part. Two main sources of uncertainty remain, however. Results for the stress fields that are locally wrong may still lead to the correct average value, if errors at different points even each other out. But, admittedly, the probability for that is very low. A second source of uncertainty is that it is not obvious that the shown results for the effective stiffness are correct: they just lie very close to another approximative estimate. But the Mori-Tanaka Method has been widely accepted as a good estimate, and thus the results obtained in this study can be classified as reliable.

4.3 Mesh Independence and Size-Effect

It has been mentioned already that mesh independence or mesh objectivity are important aspects in the application of numerical algorithms to any system of partial differential equations. It is obvious that the results of an algorithm should generally not depend on the analysts choice of discretization. However, the term mesh dependence must not be confused with the term discretization error. In any numerical solution a trade off has to be made between the size of the problem, usually determined by the number of sample points or finite elements used to represent the geometrical structure of a model, and the expected error in the solution obtained compared to the exact solution. In many cases where the governing equations are linear, estimates for the error are available in form of upper bounds. A suitable numerical algorithm has the property that the results theoretically converge and the limit is the exact solution when the number of discrete elements increases. Practically the achievable error is usually bounded from below because the propagation of round off errors also increases with the number of discrete elements. These phenomena are not considered when the term "'mesh independence"' is used within this work.

A widely known problem in numerical analysis of materials with local strain softening behavior is the fact that the width of damaged zones is usually confined to the spacing between two sample points or the dimension of a finite element. When damage initiates in a certain location, the stiffness at the corresponding point or finite element drops until it is (almost) zero, and only then surrounding elements start to show softening behavior. No limiting case for the dimension of the damaged zone can be reached. See fig. 4.9 this behavior is demonstrated for different examples. Apart from the fact that this behavior seems to be unnatural, it poses several problems. If bands of locally deteriorated material already have evolved in a model, the further propagation often depends on the stress distribution around them. In section 2.6 where the topic of fracture mechanics has been reviewed briefly it was demonstrated that infinite stresses appear at a perfect sharp crack. Around a damage-band in a numerical problem the results for stresses are not infinite, but a stress intensification close to its ends has to be expected. The damage propagates when the elastic energy belonging to these stresses exceeds the critical limit. By choosing an ever finer discretization, the width of the damaged zone becomes ever smaller and thus higher stresses will appear in the numerical solution. This means that, in this given situation, any exterior load can be made critical with respect to damage propagation by choosing a discretization that is fine enough. In addition, the averaged stress-strain relationship can not be determined since the peak stress will decrease with the width of the discrete mesh, see fig. 4.9 again. This renders any interpretation of the results meaningless.

Surprisingly, the lack of convergence does not indicate the inadequacy of the numerical algorithm. The results of Bazant [16, 19, 21] show that a continuum with damage localized in an infinitely small volume shows an instability at the verge of damage evolution. No solution exists in a mathematical sense, and this fact is only hidden by the inability of any discrete mesh to model infinitely small volumes. The finite dimensions stabilize the problem and results may be obtained, however these are not a solution to the given problem.

Experimental observation in tension tests on concrete has given additional hints that the assumption of localized damage is incorrect. Although concrete is usually thought of as brittle, it is quasibrittle in fact. The difference between both terms has been reviewed in sec. 2.6. In appropriate experimental setups the stress strain curve has a large descending
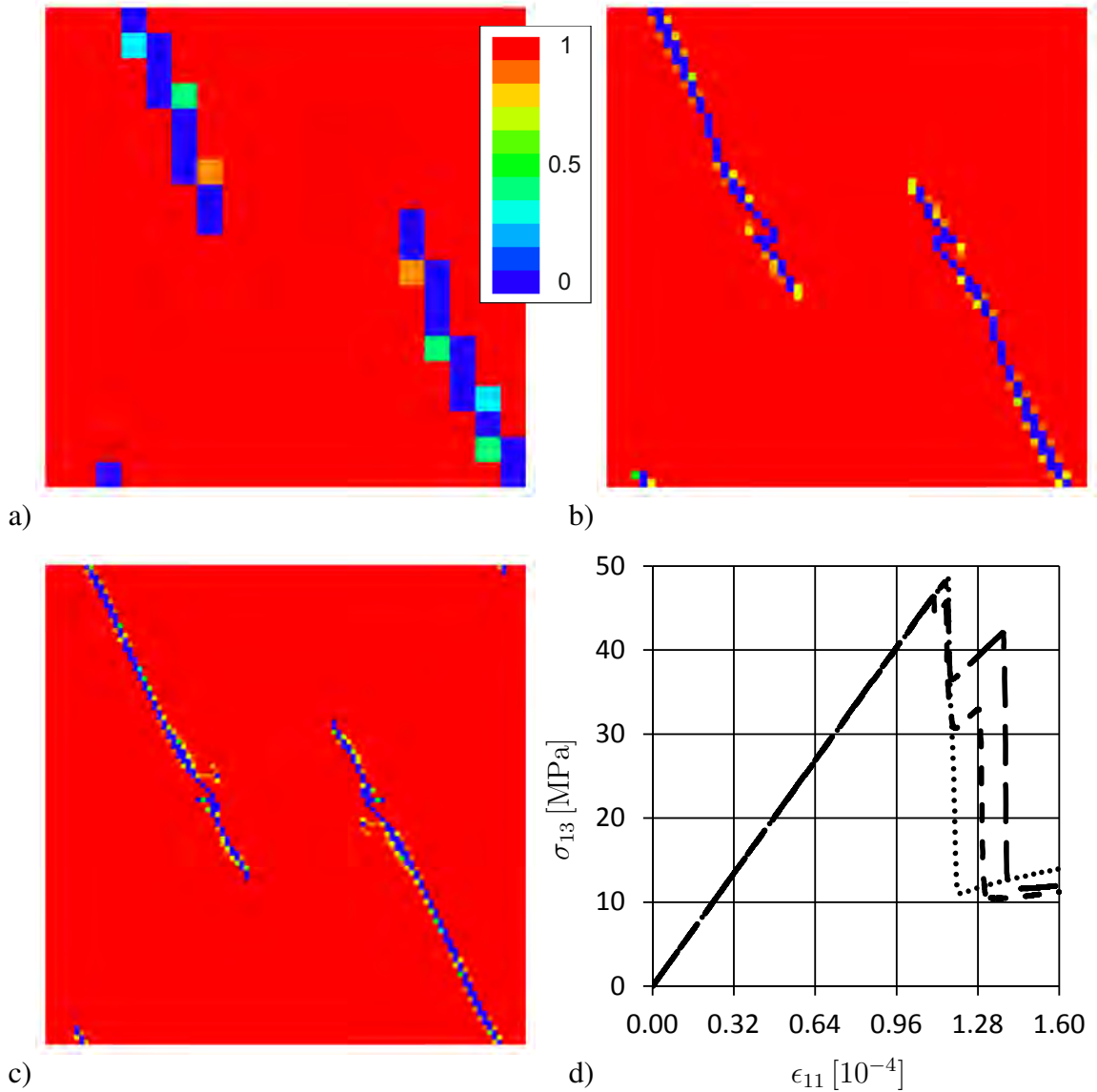
Fig. 4.7: Results with regularization practically turned off ($\beta = 0.0$). Damage results for a) $N = 20$, b) $N = 60$, c) $N = 100$. d) shows curves for three different cases: $N = 20$ (long-dashed), $N = 60$ (dashed) and $N = 100$ (dotted). Viewdirection is $v = (0, 0, 1)^T$.

part [45, 57, 122]. It was observed, e.g. by Ansari [8], that strain localizes in narrow bands where the macroscopic stiffness is reduced, due to a network of microcracks that evolves during loading. The width of these narrow bands is characteristic for a specific material and connected to a microscopic length, typically to the grain size [19].

Following these theoretical and experimental observations several non-local damage models have been developed since the end of the seventies of the twentieth century. A brief overview about the history and the physical arguments for such models is given in sec. 2.4. In sec. 3.2 it was discussed how the inclusion of the gradient term of φ and the difference term $(f(d) - \varphi)^2$ yields a non-local evolution of the damage parameter d. One of the two equations governing the nonlinear part of the model is the equation of the Helmholtz kind (3.25):

$$\varphi - \frac{\beta}{\alpha}\Delta\varphi = f(d).$$

If a function f(d) is given that is constant everywhere except one small region where the gradient and curvature are high, the solution φ to (3.25) will be a function with lower gradients and curvature everywhere. Its similarity with $f(d)$ is dependent on the parameter

$$k = \frac{\alpha}{\beta}.$$

Assume that k is high and the solution is approximately the same as the inhomogeneous part:

$$\varphi \approx f(d).$$

Then $\Delta\varphi$ has high values in regions where $f(d)$ has high curvature, and (3.25) cannot be satisfied at these points. This thought experiment shows that high values for k cause φ and $f(d)$ to be far off each other. A more detailed study on the values of k follows in the next section. If k assumes values approximately zero, even high Laplacians in φ are allowed and φ and $f(d)$ are still close to each other.

It was mentioned in sec. 3.2 that the dimensions of α and β are

$$[\alpha] = \frac{\text{Energy}}{\text{Volume}} \tag{4.33}$$

and

$$[\beta] = \frac{\text{Energy}}{\text{Volume}}\text{Length}^2 \tag{4.34}$$

respectively. The dimension of $k = \frac{\beta}{\alpha}$ accordingly is:

$$[k] = \text{Length}^2. \tag{4.35}$$

The quantity $\sqrt{k}$ with dimension Lenght is the internal length of the material. If microstructural patterns occur, especially damage bands, their minimum width is $\sqrt{k}$. All patterns with smaller dimensions are smoothed out to match this length.

In fig. 4.8 the behavior of φ is demonstrated for the one dimensional case. The following inhomogeneous linear differential equation is assumed:

$$y(x) - ky''(x) = \theta(x - a); \qquad x \in [0, 1], \tag{4.36}$$

where $\theta(x)$ is the Heaviside function with the properties:

$$\theta(x) = \begin{cases} 0 & \text{for} \quad x < 0 \\ 1 & \text{for} \quad x > 0 \end{cases}. \tag{4.37}$$

The boundary conditions are

$$y(0) = 0 \tag{4.38}$$
$$y(1) = 1. \tag{4.39}$$

The particular solution to this problem can be obtained by use of a computer algebra system:

$$y(x) = \frac{1}{4}\left(\coth\left(\frac{1}{\sqrt{k}}\right) - 1\right)e^{-\frac{a+x}{\sqrt{k}}}\left(\theta(1 - a)\left(e^{\frac{1}{\sqrt{k}}} - e^{\frac{a}{\sqrt{k}}}\right)^2\left(e^{\frac{2x}{\sqrt{k}}} - 1\right) + $$
$$4\left(\sinh\left(\frac{a+x+1}{\sqrt{k}}\right) + \cosh\left(\frac{a+x+1}{\sqrt{k}}\right)\right) \times$$
$$\left(-2\sinh\left(\frac{1}{\sqrt{k}}\right)\theta(x - a)\sinh^2\left(\frac{a-x}{2\sqrt{k}}\right)\right.$$
$$+ \theta(-a)\left(\cosh\left(\frac{a}{\sqrt{k}}\right) - 1\right)\sinh\left(\frac{1-x}{\sqrt{k}}\right) + \sinh\left(\frac{x}{\sqrt{k}}\right)\bigg)\bigg). \tag{4.40}$$

In fig. 4.8 the solution is plotted for $a = \frac{1}{2}$ and $k = 0.1$ and $k = 0.0004$. The higher choice for k causes the solution to be far off the Heaviside step function (except at the boundaries where it is forced into the same values), and the curvature is low, while the small value takes $y(x)$ closer to the step function and allows high curvature in its graph. The general observations made here are the same in the three dimensional case. Since the second term in the free energy formulation (3.16) adds the square of the absolute difference between damage function $f(d)$ and φ, and a minimization with respect to d will favor an $f(d)$ that is close to φ. Thinking in one dimension this means that the optimization will vary the inhomogeneous part (the function $\theta(x)$ in the one dimensional example and $f(d)$ in the material model formulation) towards the φ in order to lower the absolute difference between both.

In fig. 4.9 results are shown where the regularization takes effect. In contrast to the results in fig. 4.7 the damaged zone extends over a width of more than one sample point, and once the discretization is fine enough to capture the damage bands, their dimension does not depend on it any more. The stress strain curves shown in fig. 4.9f) converge to a common limit for an increasing number of sample points.
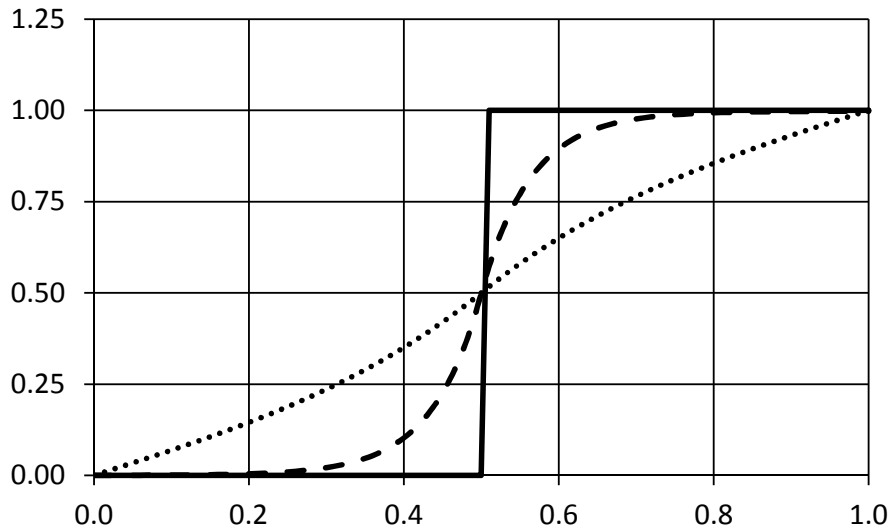

Fig. 4.8: Comparison of Heaviside function with results for (4.36). Results given for $k = 0.1$ (dotted) and $k = 0.004$ (dashed).
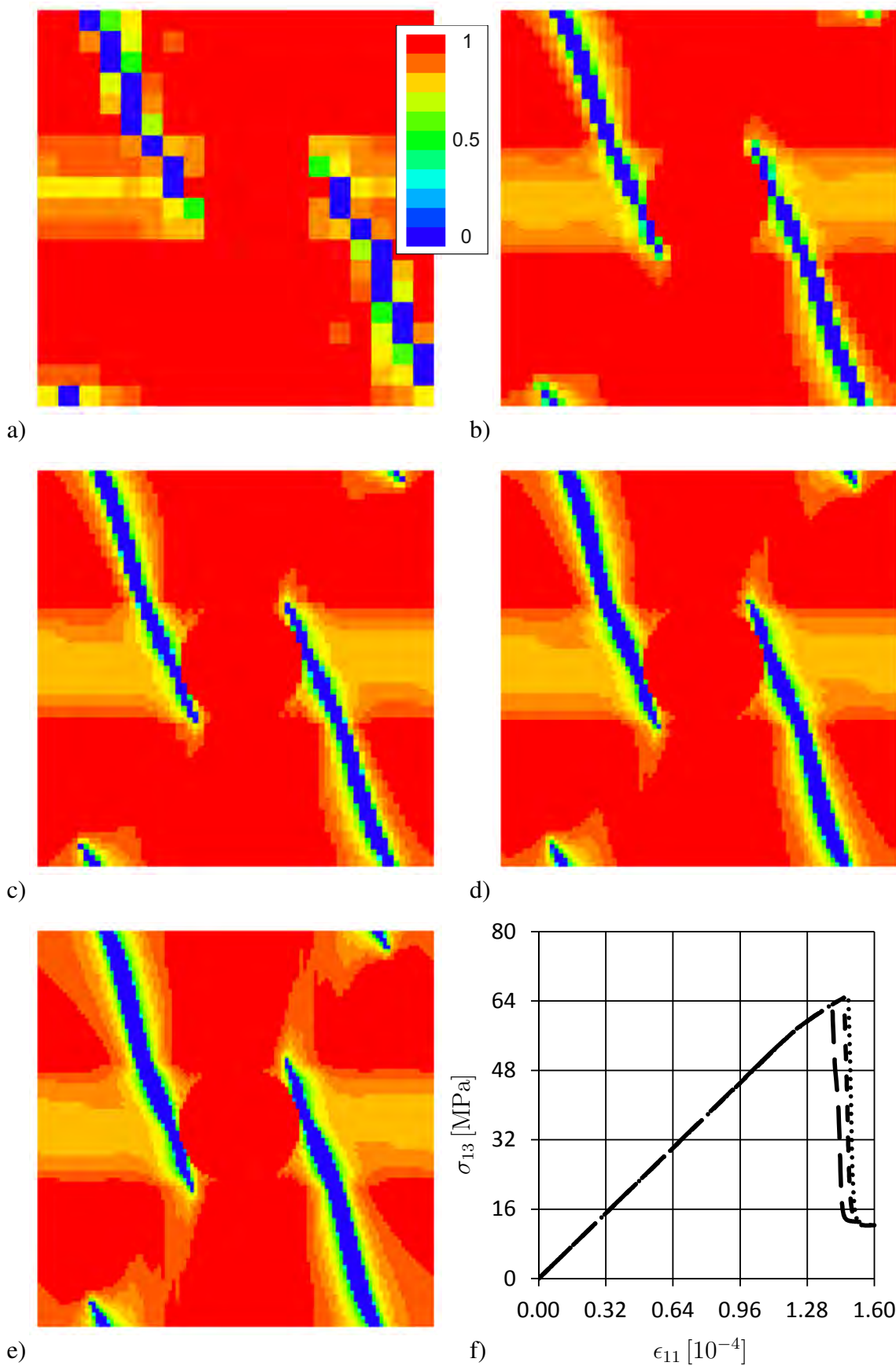
Fig. 4.9: Results with regularization ($\beta = 0.0001, \alpha = 0.1$). Damage results for a) $N = 20$, b) $N = 40$, c) $N = 60$, d) $N = 80$, e) $N = 100$. f) shows curves for three different cases: $N = 20$ (long-dashed), $N = 60$ (dashed) and $N = 100$ (dotted). View direction is $v = (0, 0, 1)^T$.

A phenomenon connected to the issue of mesh independence is the size effect, i.e. the dependence of critical loads on specimen size. Size effects occur in tension tests of many materials and are related to the relative size of the damaged zone (be it the plastic zone in metal fracture or the damage bands in concrete tests, for example) to the specimen dimensions. Since the parameter $\sqrt{k}$ is a lower bound to the minimum width of damaged zones, it must be expected that the formulation presented here is able to model a size effect as well. Inspection of the Helmholtz equation in discrete Fourier space reveals that an exterior length parameter is included in the model:

$$\hat{\varphi}(\boldsymbol{\xi}_i) = \frac{1}{1 + \frac{\beta}{\alpha} \frac{4\pi^2}{L^2} |\boldsymbol{\xi}_i|^2} \hat{f}(\boldsymbol{\xi}_i).$$

L is the length of the edges of the representative volume element. The ratio $\frac{\sqrt{k}}{L}$ determines the relative dimension of the internal length to the exterior dimensions of the RVE and, since the choice for the RVE is not arbitrary, also relative to macroscopic dimensions.
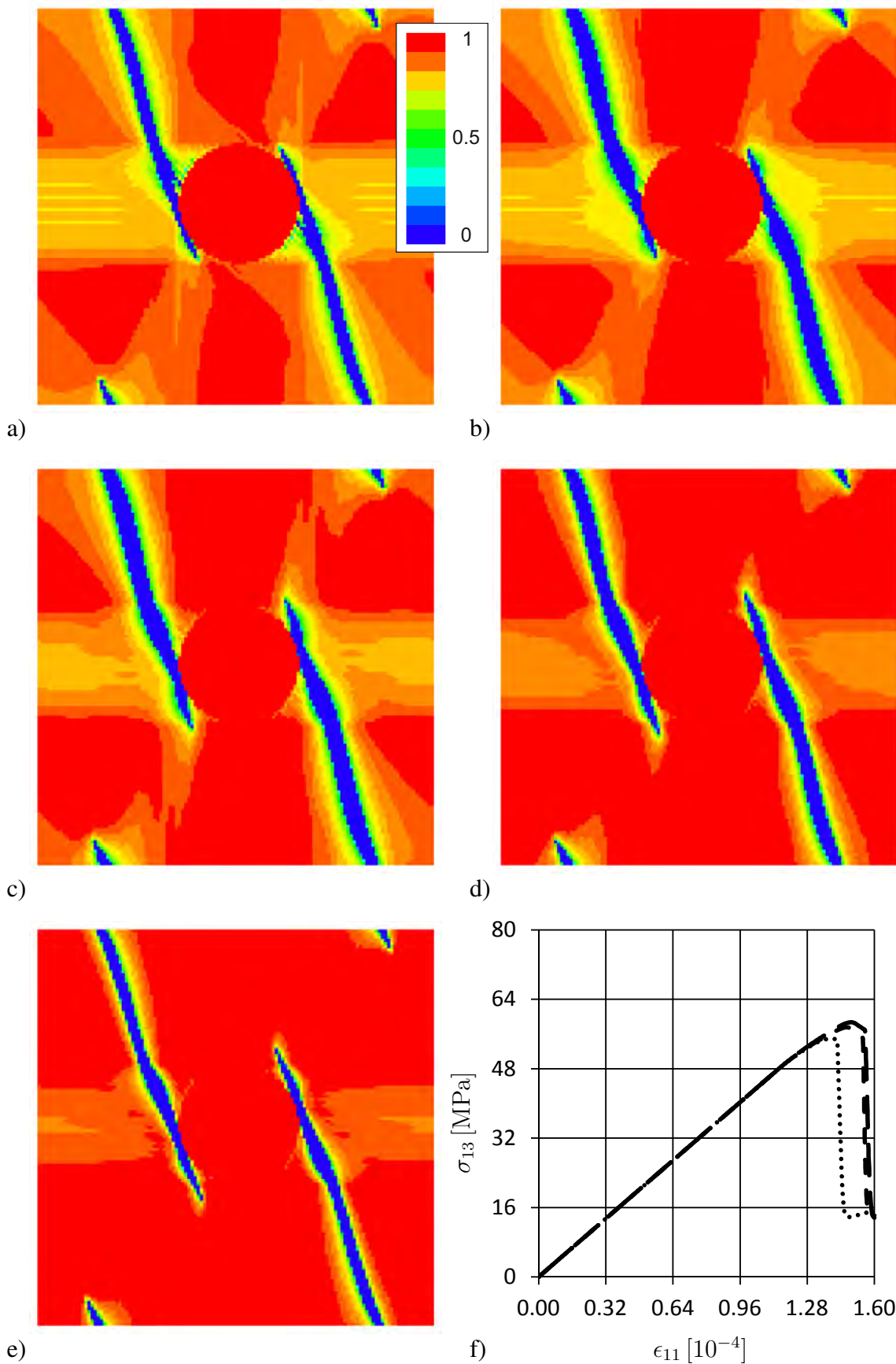
Fig. 4.10: Results to demonstrate the size effect. Damage results for a) $L = 0.1$, b) $L = 0.5$, c) $L = 1.0$, d) $L = 2.0$, e) $L = 5.0$ (dimensionless L relative to edge-length of RVE) . f) shows curves for three different cases: $L = 0.1$ (long-dashed), $L = 0.5$ (dashed) and $L = 2.0$ (dotted). View direction is $v = (0, 0, 1)^T$.

4.4 Periodicity of the Solution

a)   b)

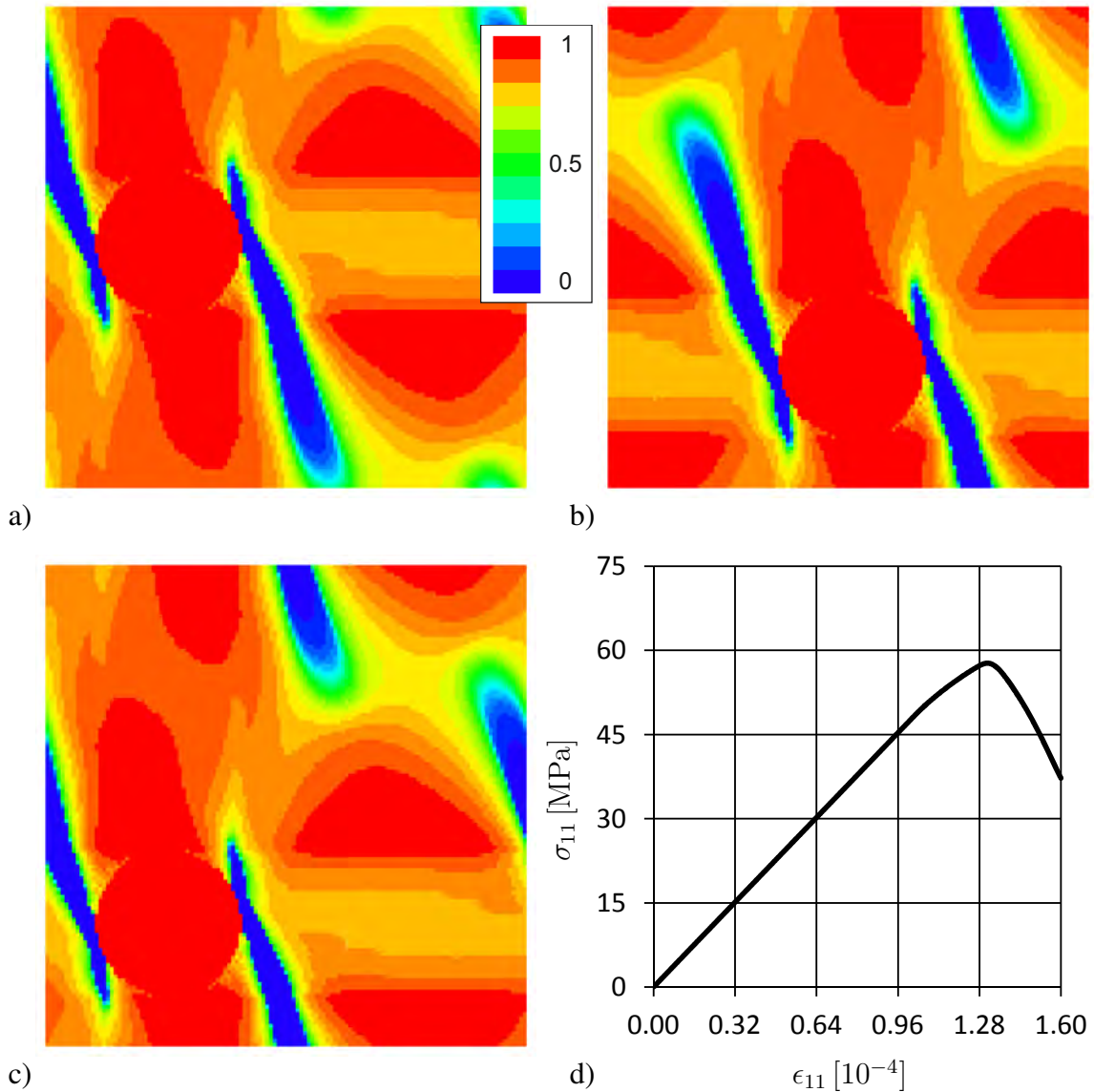c)   d)

Fig. 4.11: Three examples to demonstrate the periodicity of the numerical results. The position of the RVE with respect to the cylindrical inhomogeneity. Configuration of material parameters and load is the same in all three cases. View direction is $v = (0, 0, 1)^T$.

An important question in multiscale problems is the size of the RVE. The criteria for its choice have been reviewed in sec. 2.5. Periodic boundary conditions are natural in these problems. The solution in terms of stresses and strains is periodic, too, and should not depend on the position of the RVE relative to the microstructure. Also, the stress-strain response ($\langle\boldsymbol{\sigma}\rangle - \langle\boldsymbol{\epsilon}\rangle$-curve) should not be dependent on it. This has been checked for the current algorithm by variation of the RVE in a way, that it represents a unit cell of the same microstructure each time, and the same configuration of model parameters and load conditions is applied. Some results are presented in fig. 4.11. The same microstructure as in the previous examples has been used, but the cylinder has been shifted to different positions each time. As can be seen, the solution for the damage variable is the same in each example, only that the whole field $f(d)$, dependent on $\mathbf{x}$, is shifted by the same amount of the cylinder. Periodicity at the boundaries is preserved and tessellation of the three-dimensional space yields the same damaged structure in all cases. In fig. 4.11d) the averaged

stress-strain curves are displayed for the three examples, and they are observed as absolutely congruent. The conclusion is that the numerical algorithm really produces an approximation of the periodic stress- and strain fields, and especially numerical artifacts originating at the boundary can be excluded.

5 Results for Chosen Examples

5.1 Study of Model Parameters

The formulation of the free energy in (3.15) and (3.11), which is the basis of the material model presented and studied in this work, contains five model parameters: λ, μ, α, β and r. The symbols λ and μ denote the Lamé-parameters from classical elasticity and need not be further investigated here. The three parameters α, β and r belong to the non-local damage model. They are material specific, and the only way to determine them for a certain case is via physical experiments. The best way to achieve this is by producing data form experiment about the stress-strain relationship and determine the best fit solution with classical optimization methods, such as the least-squares method. In many cases the purpose of simulation of RVE boundary value problems is to determine the average stress-strain relationship of a composite. Thus experiments would not be carried out on the composite material, but rather on single phase materials that are present in the composite microstructure. Since the damage model is isotropic as well as the linear elastic model, only a reduced number of tests is necessary compared to anisotropic models. In this section the influence of the parameters is studied by numerous examples of simulations with different settings. It is not the aim to provide values for them adjusted to a certain real material, thus no real experimental data is used. The study is conceptual and aims at revealing the behavior of the model under certain circumstances.

5.1.1 Dissipation Parameter r

The first step to study the influence of the dissipation parameter r on the results is the examination of the equations governing material behavior, which are given in (3.25) and (3.30):

$$\varphi - \frac{\alpha}{\beta}\Delta\varphi = f$$
$$\alpha f^2 + (\psi_0 - \varphi\alpha)f \leq r.$$

As long as the material stays within the elastic domain, i.e. no damage has occurred so far, the values for φ and f are

$$\varphi = f = 1 \tag{5.1}$$

everywhere in the RVE. The second equation then turns into:

$$\alpha f^2 + (\psi_0 - \varphi\alpha)f = 1 - 1 + \psi_0 = \psi_0 \leq r. \tag{5.2}$$

Thus a simple flow-rule like condition for the onset of damage is obtained, and r plays the role of an energy threshold. No matter what the choices for α and β are, damage will

always occur at the same energy level as long as r remains the same. After initiation of damage the quotient β/α determines the shape of φ and φ, α and r together determine the further evaluation of f. Thus a change in r may not only change the point at the stress-strain curve, where the first damage occurs, but also the shape of the curve, e.g. when the peak is reached and the slope becomes negative. Also the damage pattern may change even if r is the only parameter that is altered. Figs. 5.2 and 5.1 demonstrate the impact of r. Fig. 5.1a) show the load curve for different examples, all with the same configuration except that r takes values from $r = 0.04$ to $r = 0.095$. First, it is obvious that higher values for r mean that the curves starts later to deviate form the linear form, second, the peak stress gets higher if r assumes high values. All curves look very similar up to the peak stress, although not exactly similar. It might be expected that the peak stress is linearly dependent on r but this is not the case, as can be seen in fig. 5.1b), where the peak stress is plotted against the corresponding value for r. The relationship is clearly not linear, and this fact originates in the interplay between α, β and r. A sole change of r changes the ratio of r/α and therefore the propagation of damage differs after its onset.
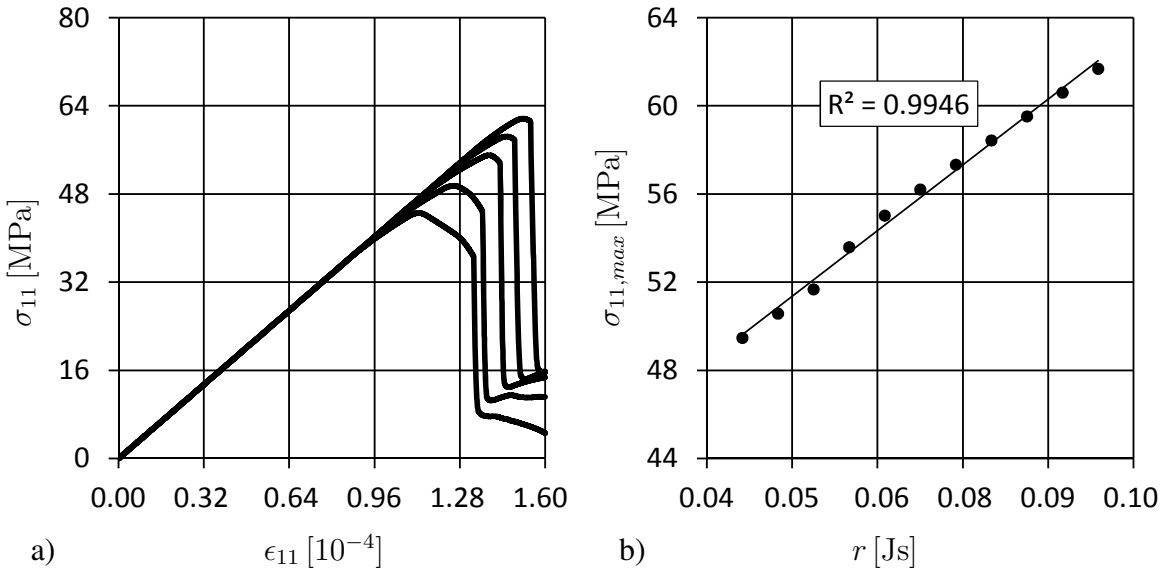

Fig. 5.1: a) Stress-strain curves for varying dissipation parameters: $r = 0.045, 0.055, 0.07, 0.085, 0.095$. Curves with higher peak belong b) Peak of stress strain relationship vs. dissipation parameter, with least-squares line and correlation coefficient R^2. Configuration: $\alpha = 0.2$, $\beta = 0.0001$, $\boldsymbol{\epsilon} = (0.0016, 0, 0, 0, 0, 0)^T$.

In fig. 5.2 three examples for the damage pattern that evolved after an average strain of

$$\langle \boldsymbol{\epsilon} \rangle = (0.0016, 0, 0, 0, 0, 0)^T \tag{5.3}$$

was reached are given. On the right side the damage distribution over the $x - y$-plane (perspective view: $(0, 0, 1)^T$) in the middle of the RVE is illustrated, and on the right side the corresponding averaged stress-strain curve is highlighted. For $r = 0.04$ the material stiffness has been largely degraded at the given state, and in addition to two very sharp, crack-like zones where the stiffness is practically zero the matrix material is globally damaged by roughly a factor of one half. The corresponding curve passes a ductile zone around the peak until a sudden drop in stiffness takes place (which belongs to the sudden origination and propagation of the two crack-like zones).
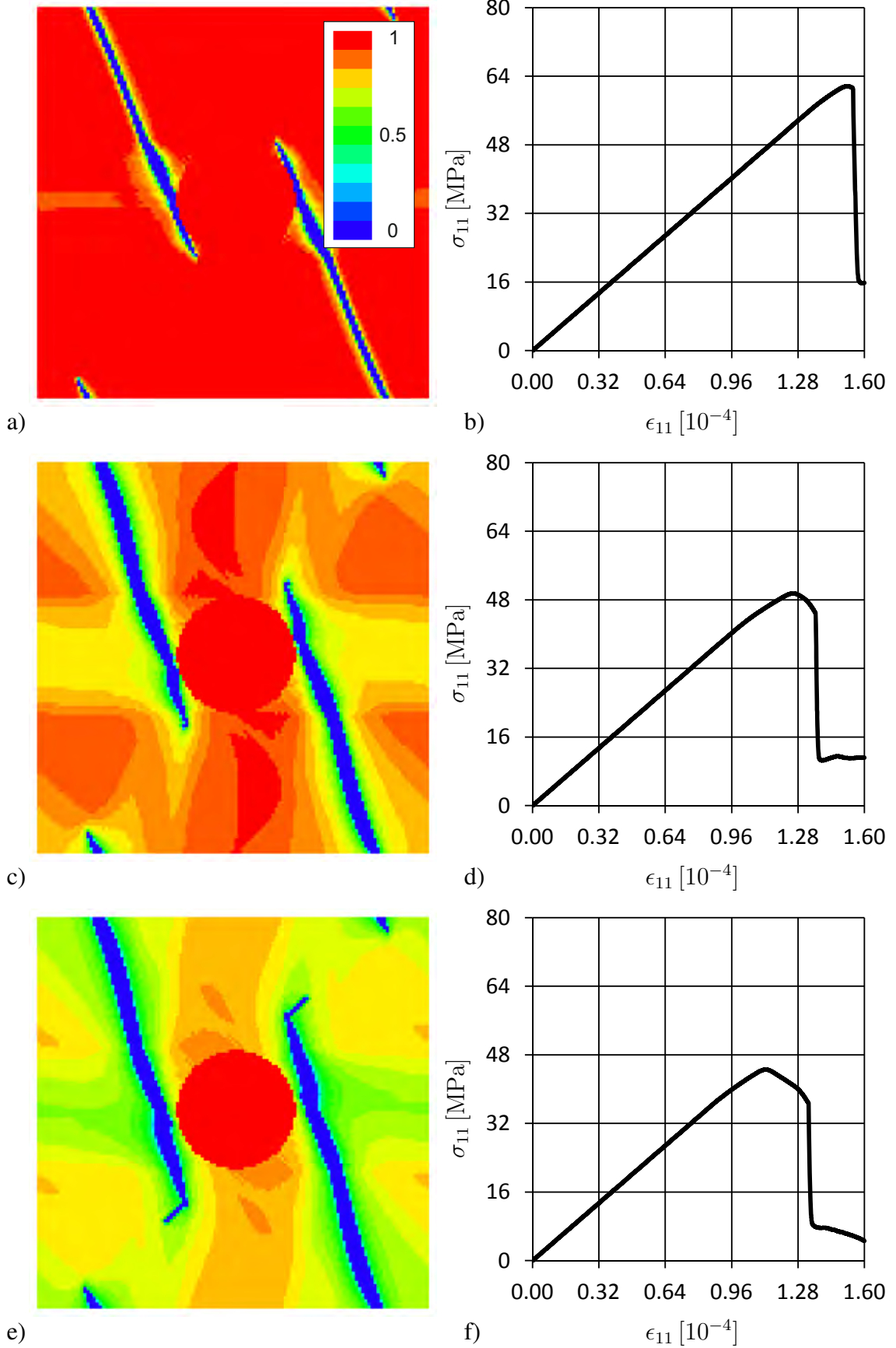
Fig. 5.2: Results for varying dissipation parameter. Configuration for all examples: $\alpha = 0.2, \beta = 10^{-4}, N = 64, \langle \boldsymbol{\epsilon} \rangle = \left(1.6 \cdot 10^{-3}, 0, 0, 0, 0, 0\right)^T, \Delta \boldsymbol{\epsilon} = 1.6 \cdot 10^{-6}$.
Dissipation parameter: $a) \, r = 0.04, \; b) \, r = 0.05, \; c) \, r = 0.95$

For $r = 0.05$ the same two crack patterns appear and there exist zones of areal degradation outside them, but parts of the matrix are still undamaged. The curve approaches a higher peak and also sees a sudden stiffness drop, but not as severe as in the first example. The last example shows damage only in two very narrow zones, and outside these zones the material is practically unchanged. The peak of the stress strain curve is the highest among the shown examples, and the stiffness drop takes place almost the moment the peak is reached. This resembles more brittle behavior than the other examples, and the observation is in line with the evolving crack pattern: sharp cracks propagating through the material cause sudden material failure contrary to materials where the damage is distributed over larger zones. It is an interesting result that only by change of the factor r the material behavior can be controlled over such a variety of phenomena, although the ductile behavior has been added to the model with the penalty terms that include α and β. In the test series presented here the most brittle behavior is accompanied by the highest resistance to crack- or damage propagation, which does not coincide with general observation made on real materials, which has been discussed in sec. 2.6. This is no problem since no simulation of different real materials is done here but a study on the behavior of the mathematical model. It is usually not possible in reality to control only one material parameter isolated without affecting the others.

5.1.2 Regularization Parameters α and β

It is convenient to introduce the parameter $k = \frac{\beta}{\alpha}$ and rewrite (3.25) and (3.30):

$$\varphi - k\Delta\varphi = f$$
$$\alpha f^2 + (\psi_0 - \varphi\alpha)f \leq r.$$

It is assumed throughout this section that a given choice for r is made, and the impact of variations in α and β is investigated.

If β becomes very small, it follows from the Helmholtz like equation that φ becomes equal to f:

$$\beta \to 0 \Rightarrow \varphi \to f \tag{5.4}$$
$$\Rightarrow \alpha f^2 - \alpha\varphi f + \psi_0 f \to \alpha(f^2 - f^2) + \psi_0 f = \psi_0 f \tag{5.5}$$
$$\Rightarrow \psi_0 f \leq r. \tag{5.6}$$

The last line shows that setting $\beta = 0$ or at least very small reduces the model to the classical local damage model (3.1), where α and β have no influence any more and the model is non-regularized and local again. Therefore it must be expected that the damage occurs locally for small β and the averaged stress strain curve is of the brittle kind. An example for the damage pattern that evolves and the resulting stress strain curve is shown in fig. 5.3a) and b). The damage is localized in small, narrow bands that resemble crack like structures, and the stress strain curve sees a sudden drop in stiffness once it passes the point of peak stress. Little deviation from the linear part is observed prior to the peak. In fig. 5.4a) a map is shown to illustrate the influence of α and $k = \frac{\alpha}{\beta}$. Blue boxes indicate that for the given combination of α and k the resulting damage field and the internal variable φ remain approximately the same. Green boxes indicate big differences between both fields. A $\times$-symbol indicates brittle, local damage behavior and a $\circ$ stands for ductile behavior with non-local damage evolution.
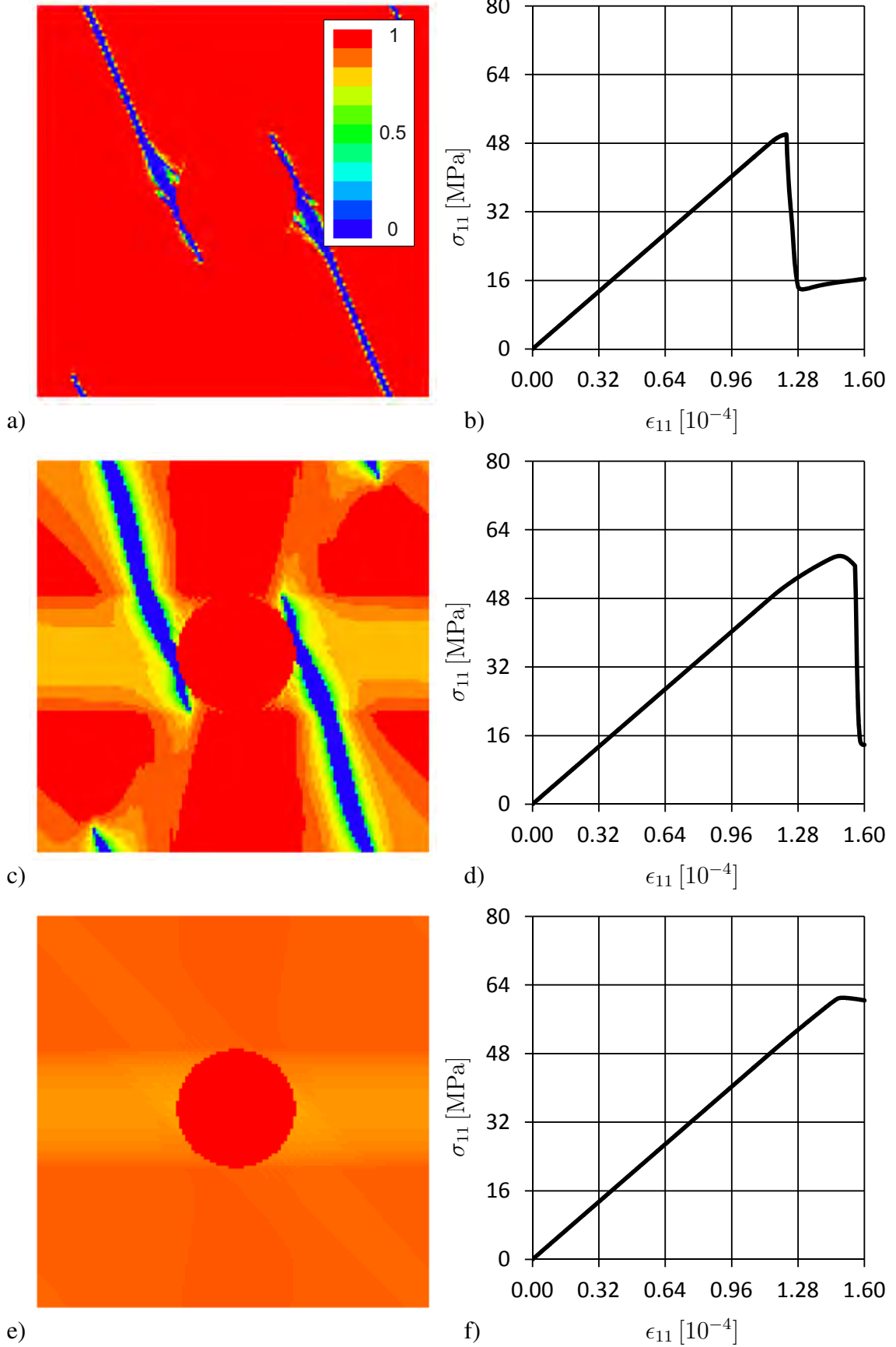
Fig. 5.3: Results for different configurations of α and β. $N = 128$, $r = 0.07$ and $\langle \boldsymbol{\epsilon} \rangle = (0.0016, 0, 0, 0, 0, 0)^T$. Regularization parameters: a) $\alpha = 0.2$, $\beta = 0.0002$, b) $\alpha = 0.4$, $\beta = 0, 0004$, c) $\alpha = 1.0$, $\beta = 1.0$. View vector is $\mathbf{v} = (0, 0, 1)^T$

a)

α \ k	10^{-7}	10^{-6}	10^{-5}	10^{-4}	10^{-3}	10^{-2}	10^{-1}	10^{0}
10^{-1}	×	×	×	×	×	×	×	×
$2 \cdot 10^{-1}$	×	×	×	×	⊗	⊗	⊗	⊗
$4 \cdot 10^{-1}$	×	×	×	⊗	O	O	O	O
$6 \cdot 10^{-1}$	×	×	⊗	O	O	O	O	O
$8 \cdot 10^{-1}$	×	×	×	O	O	O	O	O
$1 \cdot 10^{0}$	×	×	×	O	O	O	O	O
10^{1}	O	O	O	O	O	O	O	O

b)

α \ k	10^{-7}	10^{-6}	10^{-5}	10^{-4}	10^{-3}	10^{-2}	10^{-1}	10^{0}
10^{-1}	×	×	×	×	×	×	×	×
$2 \cdot 10^{-1}$	×	×	×	⊗	⊗	⊗	O	O
$4 \cdot 10^{-1}$	×	×	×	⊗	⊗	⊗	O	O
$6 \cdot 10^{-1}$	×	×	⊗	O	O	O	O	O
$8 \cdot 10^{-1}$	×	×	O	O	O	O	O	O
$1 \cdot 10^{0}$	×	×	O	O	O	O	O	O
10^{1}	O	O	O	O	O	O	O	O

Fig. 5.4: Results of parameter study on α and k. ×-symbol: localized damage, o-symbol: nonlocal damage, blue fill: $f \approx \varphi$, green fill: $f \neq \varphi$. Results for a) tension and b) shear deformation.
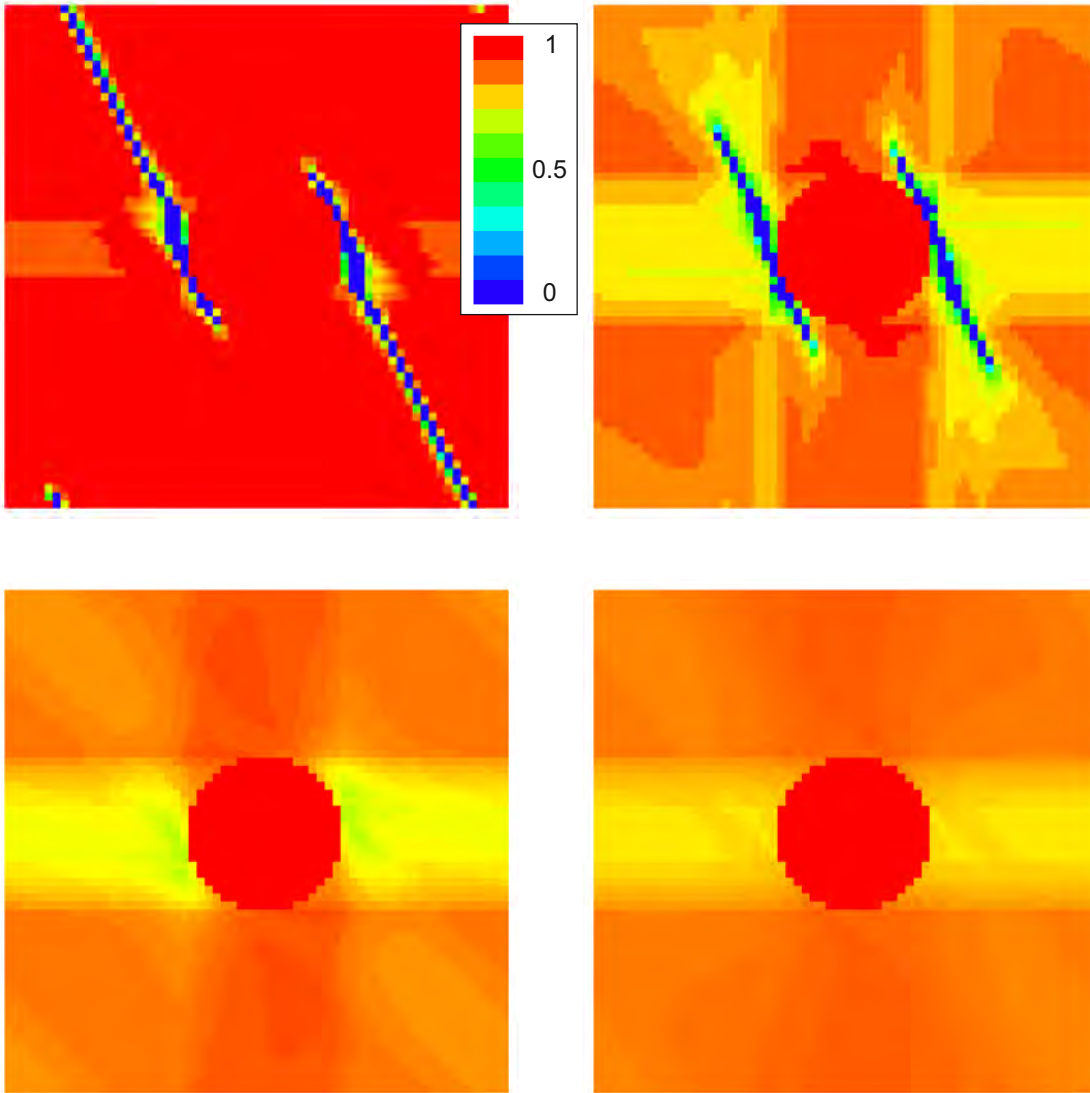

Fig. 5.5: Results for different configurations of α and β. $N = 128$, $r = 0.07$ and $\langle \boldsymbol{\epsilon} \rangle = (0.0016, 0, 0, 0, 0, 0)^T$. Regularization parameters: a) $\alpha = 0.2$, $\beta = 2.0 \cdot 10^{-8}$, b) $\alpha = 0.6$, $\beta = 6.0 \cdot 10^{-6}$, c) $\alpha = 0.6$, $\beta = 6.0 \cdot 10^{-5}$, d) $\alpha = 0.6$, $\beta = 0.006$. View vector is $\mathbf{v} = (0, 0, 1)^T$

In fig. 5.5 examples are given to provide a feeling on what "'local"' and "'non-local"' means in this context. Fig. 5.5a) clearly shows local behavior, with almost no damage occurring outside the crack like zones. Fig. 5.5b) shows a more non-local pattern, since the material stiffness has degraded in a wide horizontal band before additional damage localizes in zones similar to those in fig. a). This pattern is still classified as local, although, depending on the level of material degradation outside the crack zones, it may be classified as a mixture of both. These cases have been indicated with the symbol $\otimes$. In fig. 5.5c) and 5.5d) are examples for nonlocal behavior. Fig. c) still shows some dependence on location, whereas in fig. d) the material degrades constantly over the whole matrix volume. Low β means low k (with the actual value of k also depending on α, of course), and the upper left corner of the diagram in fig. 5.4a) shows the corresponding behavior. As expected, the material behaves brittle ($\times$-symbol) and no or very little difference is observed between φ and f (blue boxes). If β and α is chosen in a way that k remains smaller than 10^{-5} the material behavior is always brittle, and the actual choices of α and β do not make any difference.

The factor k also gets small, when α tends towards infinity. Therefore:

$$\alpha \to \infty \Rightarrow \varphi \to f \tag{5.7}$$
$$\Rightarrow \alpha f^2 - \alpha \varphi f + \psi_0 f \to \psi_0 f \tag{5.8}$$
$$\Rightarrow \psi_0 f \leq r. \tag{5.9}$$

The same conclusions as for $\beta \to 0$ can be drawn from (5.9): the material will act brittle, and damage will localize. In fig. 5.6a) and 5.6b) two examples are shown with configurations that both set $k = 10^{-8}$. The observations coincide with the results expected from analysis. The reader may be irritated by the values of α, since the analysis started with the assumption $\alpha \to \infty$. This formulation was simply chosen for convenience and in accordance to math standards. What practically counts is that k becomes very small, and this may be achieved with the given values.
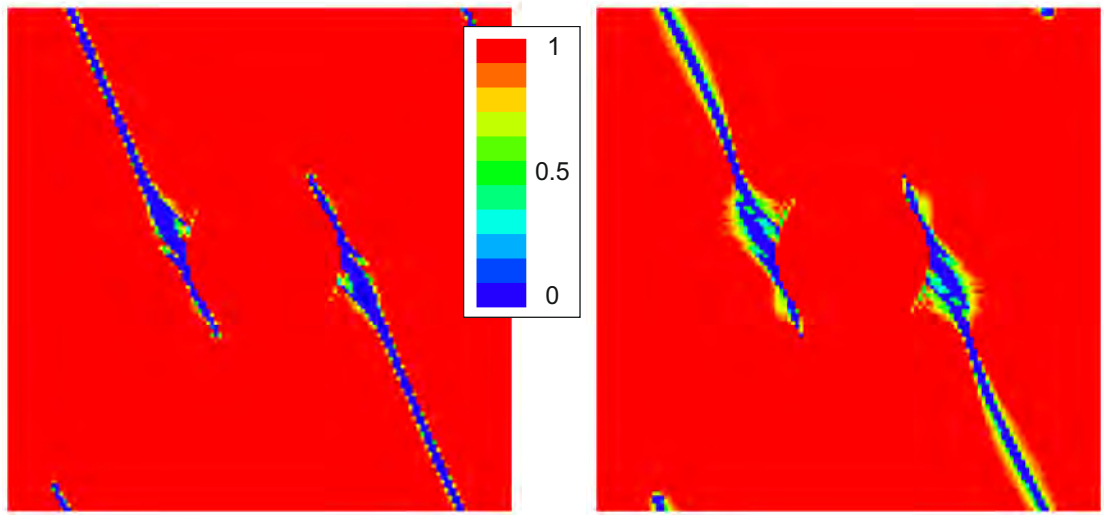

Fig. 5.6: Two results for different configurations, but with same $k = 10^{-8}$. $N = 128$, $r = 0.07$ and $\langle \boldsymbol{\epsilon} \rangle = (0.0016, 0, 0, 0, 0, 0)^T$. Regularization parameters: a) $\alpha = 0.1$, $\beta = 1.0 \cdot 10^{-9}$, b) $\alpha = 1.0$, $\beta = 1.0 \cdot 10^{-8}$. View vector is $\mathbf{v} = (0, 0, 1)^T$

It may be deduced that k might be the determining parameter for the material behavior, and two simulations with k set to the same value would yield the same results. This would rank

one of the two regularization parameters obsolete, since only the ratio between both would make a difference. However, this is generally not the case. As can be seen in fig. 5.4a), if $k = 10^{-4}$ is set, the observed results range from brittle to very ductile behavior. The reason for that is that α appears alone in (3.30), and the ratio of $\frac{r}{\alpha}$ also influences the solution. α and β cannot be treated isolated from each other, nor can one parameter be set constant when the whole range of possible model responses should be investigated.

When α and β both assume finite values such that k lies somewhere above 10^{-5}, the Helmholtz like equation will yield a field φ different from f. This is obvious since, when the energy threshold for damage initiation is exceeded in some points, f decreases locally in the first iteration. The gradient and the Laplacian of f are high near these points. The assumption $\varphi \approx f$ determines a high value also for $\Delta\varphi$, and the equation

$$\varphi + k \cdot \Delta\varphi = f$$

cannot be satisfied if k is not very small. From this follows that even at points where $\psi_0 f$ does not exceed the limit r, the equation

$$\alpha f(f - \varphi) + \psi_0 f \leq r$$

may not be satisfied. Since $(f - \varphi)$ cannot be zero for non-constant f, f itself must be reduced to lower the value of the quantity $\alpha f(f - \varphi)$. This way α determines the evolution of f in points off the points of damage origination. The higher α gets, the more damage occurs on these points, thus simulating a more non-local, ductile behavior. β penalizes the gradient of φ, therefore determining whether or not φ may see sharp slopes. Very high values for β cause φ to be approximately constant. A high ratio $k = \frac{\beta}{\alpha}$ determines the level of proximity to f. If φ and f are different, it is the value of α that increases damage in finite distances from the point of first occurrence, since it penalizes a high difference $f - \varphi$. The lower right corner of the map in fig. 5.4a) is where the results of such configurations may be found.

In the map in fig. 5.4a) it is observed that for $\alpha \in [10^{-1}, 2 \cdot 10^{-1}]$ the difference between φ and β becomes very high (transition from blue boxes to green boxes). For higher α both fields develop closer to each other again if k exceeds a certain limit, for example for $k = 10^{-1}$ and $\alpha = 4 \cdot 10^{-1}$. For $\alpha > 8 \cdot 10^{-1}$ both fields are almost equal regardless of the choice for β respective k. The reason is, that for high α the difference $f - \varphi$ must become small in order to satisfy the yield function (3.30). High k penalizes big gradients, and an approximately constant φ yields an approximately constant f because the difference must remain small. It becomes clear that ductile model behavior may come along with different fields φ and f or with no differences at all. The configurations with high k and very high α lead to results with the highest resistance to damage propagation, and a late sharp drop in elastic stiffness.

The map in fig. 5.4b) shows the results obtained for an applied average shear strain,

$$\langle \boldsymbol{\epsilon} \rangle = (0, 0, 0, 0.0014, 0, 0)^T, \tag{5.10}$$

i.e. a shear deformation in the plain perpendicular to the cylinder. The conclusions that can be drawn from the map are very similar to those drawn for tensile deformation. However, the variety of damage patterns is higher for shear deformation, as is demonstrated with the plots in fig. 5.7. Fig. 5.7a) displays the result for a brittle configuration , where damage

is located around the embedded stiff cylinder. Fig. b) shows a very ductile configuration, where localized damage occurs only after some global degradation has taken place. Serious damage localizes in zones aligned fourty five degrees to the horizontal axis, in line with the cylinders. The third example presented in fig. 5.7c) shows very ductile behavior with no appearance of localized damage so far. The corresponding curves have the familiar shapes associated with the different damage patterns respectively.
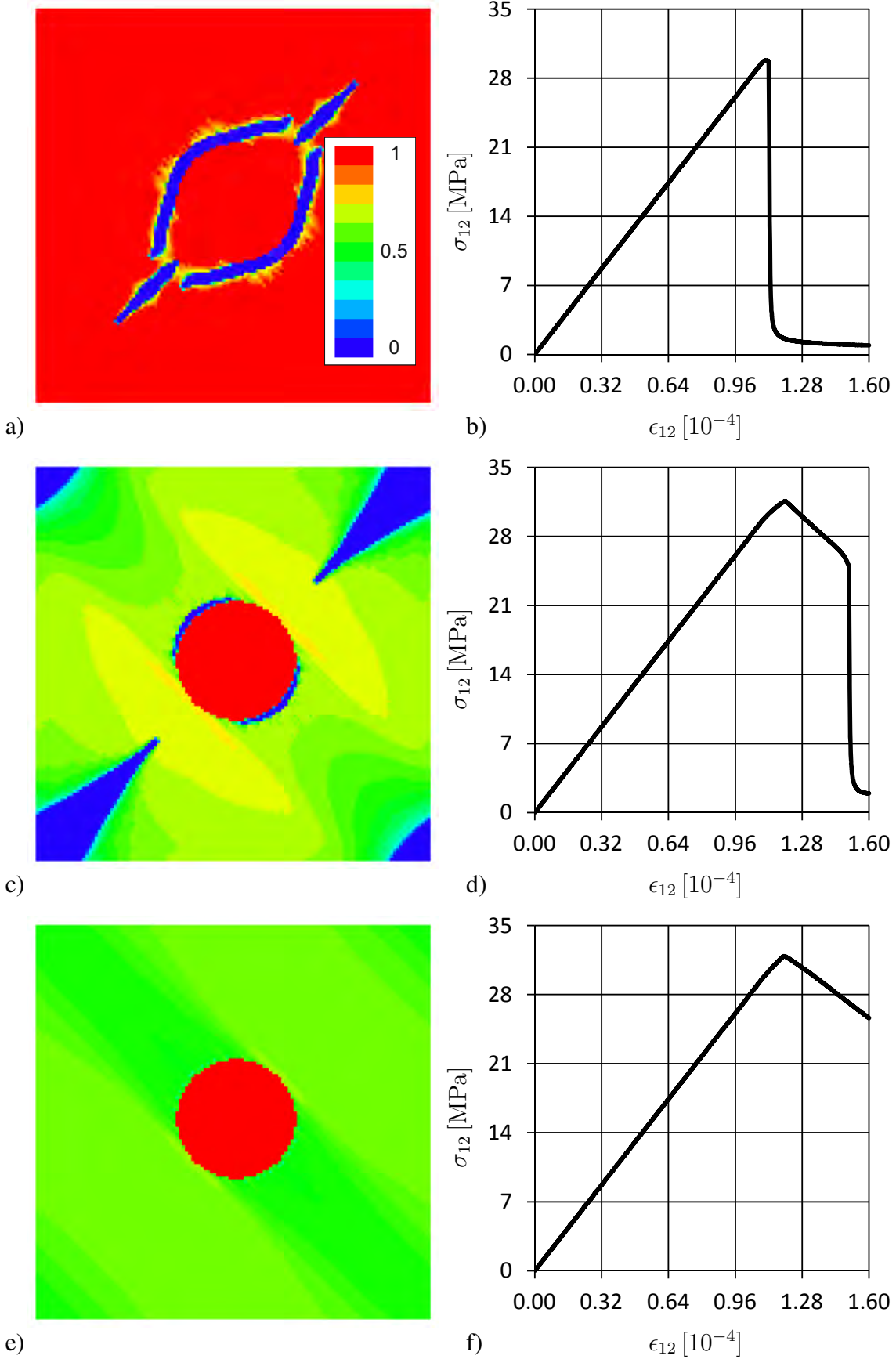
Fig. 5.7: Results for different configurations of α and β. $N = 128$, $r = 0.07$ and $\langle \epsilon \rangle = (0.0016, 0, 0, 0, 0, 0)^T$. Regularization parameters: a) $\alpha = 0.2$, $\beta = 2.0 \cdot 10^{-8}$, b) $\alpha = 0.2$, $\beta = 0.02$, c) $\alpha = 0.4$, $\beta = 0.4$. View vector is $\mathbf{v} = (0, 0, 1)^T$

5.2 Analysis of a Three Dimensional Example

After studying the influence of the model parameters α, β and r it is now possible to systematically choose them in order to approximate a desired material behavior. To show the capability of the developed algorithm two really three dimensional examples are analyzed in this and the next section. The examples analyzed until now were of a simple nature and could have been treated as two dimensional cases. That was necessary to keep the solution as simple as possible yet not to simple, such that it can serve to illustrate the behavior of the material model in certain situations. But the true capability of the algorithm presented here lies in the fact that it can handle three dimensional problems with complex microstructures, and the aim of the last part of this thesis is to demonstrate that.

The representative volume element constructed for this purpose consists of two stiff cylinders with radius $r = 0.1$ embedded in a softer matrix, while the two cylinders are positioned vertically to each other but not overlapping. Mathematically the set of spatial points filled by the stiffer material can be described by

$$\Omega = \left\{ \mathbf{x} \in \mathcal{V} | (x_2 - 0.5)^2 + (x_3 - 0.3)^2 \leq r \vee (x_1 - 0.5)^2 + (x_3 - 0.7)^2 \leq r \right\}. \tag{5.11}$$

In fig. 5.8b) a visualization of the RVE can be found. The complete parameter configuration can be found in table 5.1. From λ and μ the corresponding engineering constants Young's

$r_{\mathcal{V}\backslash\Omega}[\mathrm{J}\cdot\mathrm{s}]$	0.07
$\alpha_{\mathcal{V}\backslash\Omega}[\mathrm{J}]$	10^{-1}
$\beta_{\mathcal{V}\backslash\Omega}[\mathrm{J}\cdot\mathrm{m}^2]$	10^{-6}
$\lambda_{\mathcal{V}\backslash\Omega}[\mathrm{MPa}]$	9722
$\mu_{\mathcal{V}\backslash\Omega}[\mathrm{MPa}]$	14583
$\lambda_{\Omega}[\mathrm{MPa}]$	107051
$\mu_{\Omega}[\mathrm{MPa}]$	77519
$L[\mathrm{m}]$	0.1

Tab. 5.1: Parameter configuration

modulus Y and Possoin ratio ν can be calculated, and from them the Reuss average ν_R of the composite can be obtained by applying the following formula:

$$\nu_R = \frac{c(Y_{\mathcal{V}\backslash\Omega}\nu_{\Omega} - Y_{\Omega}\nu_{\mathcal{V}\backslash\Omega}) + Y_{\Omega}\nu_{\mathcal{V}\backslash\Omega}}{Y_{\Omega}(1 - c) + cY_{\mathcal{V}\backslash\Omega}} \approx 0.201, \tag{5.12}$$

where c is the volume concentration of the stiffer material. The average strain that is applied to the RVE is

$$\langle \boldsymbol{\epsilon} \rangle = (\nu_{\Omega}, \nu_{\Omega}, , 0, 0, 0)^T. \tag{5.13}$$

The idea is to reproduce a situation similar to one dimensional stress on the macroscopic level. The strain (5.12) will produce almost zero average stress in x_1- and x_2-direction. It will not be perfectly zero since the Reuss average is not the exact effective parameter. The tension in x_3 direction is applied perpendicular to both stiff fibers, and it may be expected

that stresses are high in the region middle to the RVE, where both fibers are closest to each other.

The first step is to analyze stress distribution prior to damage initiation within the RVE. For this purpose, the damage part of the model is deactivated when applying the strain (5.13). The corresponding results are displayed in fig. 5.8 and 5.9. The left side of fig. 5.8 shows distribution of stresses σ_{33} in three planes perpendicular to each other. On the right side the corresponding plane is visualized in the RVE to facilitate orientation. It has to pointed out that these plane do not represent cutting planes in the sense of classical elasticity, since the first and second cut would not make σ_{33} visible, respectively. Illustrated is the value that σ_{33} approaches in points belonging to the plane at choice. As has to expected from the symmetry of the problem, the distribution of σ_{33} is the same for the planes perpendicular to $\mathbf{e}_1$ and $\mathbf{e}_2$. The highest stress levels appear in the strong fibers which also has to be expected. On the third plane, which is perpendicular to $\mathbf{e}_3$, all points belong to the soft matrix. It can be seen that stresses are in the expected place. In order to better predict the appearance of damage it makes sense to analyze the elastic energy ψ_0, which is displayed in fig. 5.10. The afore mentioned symmetry is again resembled by the distribution of ψ_0, and in the third figure it can be seen that the most energy in the matrix is stored in the place between both fibers. The first two figures indicate an almost cylindrical region perpendicular to both fibers where high amounts of elastic energy are stored. This part of the RVE is stiffened considerably in x_3-direction whereas the energy level in matrix regions off the fibers is only about twenty percent of its highest value (of course, its highest value in the matrix, and not the fibers where stresses are naturally much higher). The peaks of the energy in the matrix appear at the boundaries between fibers and surrounding material, which can be deduced from fig. 5.9a) and 5.9c). It can be expected from this that damage originates somewhere in the cylindrical region perpendicular to both fibers.

The next step is to activate the damage model, with the parameters given in tab. 5.1, and analyze the evolution and distribution of damage. The applied average strain is now:

$$\langle \boldsymbol{\epsilon} \rangle = (-0.0016\nu_R, -0.0016\nu_R, 0.0016, 0, 0, 0)^T. \tag{5.14}$$

The final load is approached with the subsequent application of load steps that are one thousandth part of the final value:

$$\Delta \langle \boldsymbol{\epsilon} \rangle = 10^{-3} \langle \boldsymbol{\epsilon} \rangle. \tag{5.15}$$

In fig. 5.10 a three dimensional representation of the results for damage function $f(d)$ is given for three different stages of the process. The right side displays the stress-strain curve and serves as orientation. The scale goes from invisible over gray ($f(d) \approx 0.8$) to black ($f(d) \approx 0$). It can be seen that damage develops first in the region where it has also been expected from stress analysis. Damage is smeared over a considerable part of the region with no localized patterns visible yet. The stress strain curve deviates only slowly from the linear curve and resembles high resistance against damage propagation. In fig. 5.10b) the damage is distributed over a bigger portion of the matrix even, and additionally local concentrations of damage appear, starting from the boundaries of the fibers. The starting points are the points of peaks in the elastic energy already identified in the previous investigation. The patterns propagate into the not so much loaded region of the matrix. The stress-strain curve shows a kink and has negative slope. Finally, after damage bands have propagated into much of the matrix material across the RVE, the damage process halts and the curve flattens again, approaching small positive slope in the end. The RVE has lost approximately 80% of its stiffness.
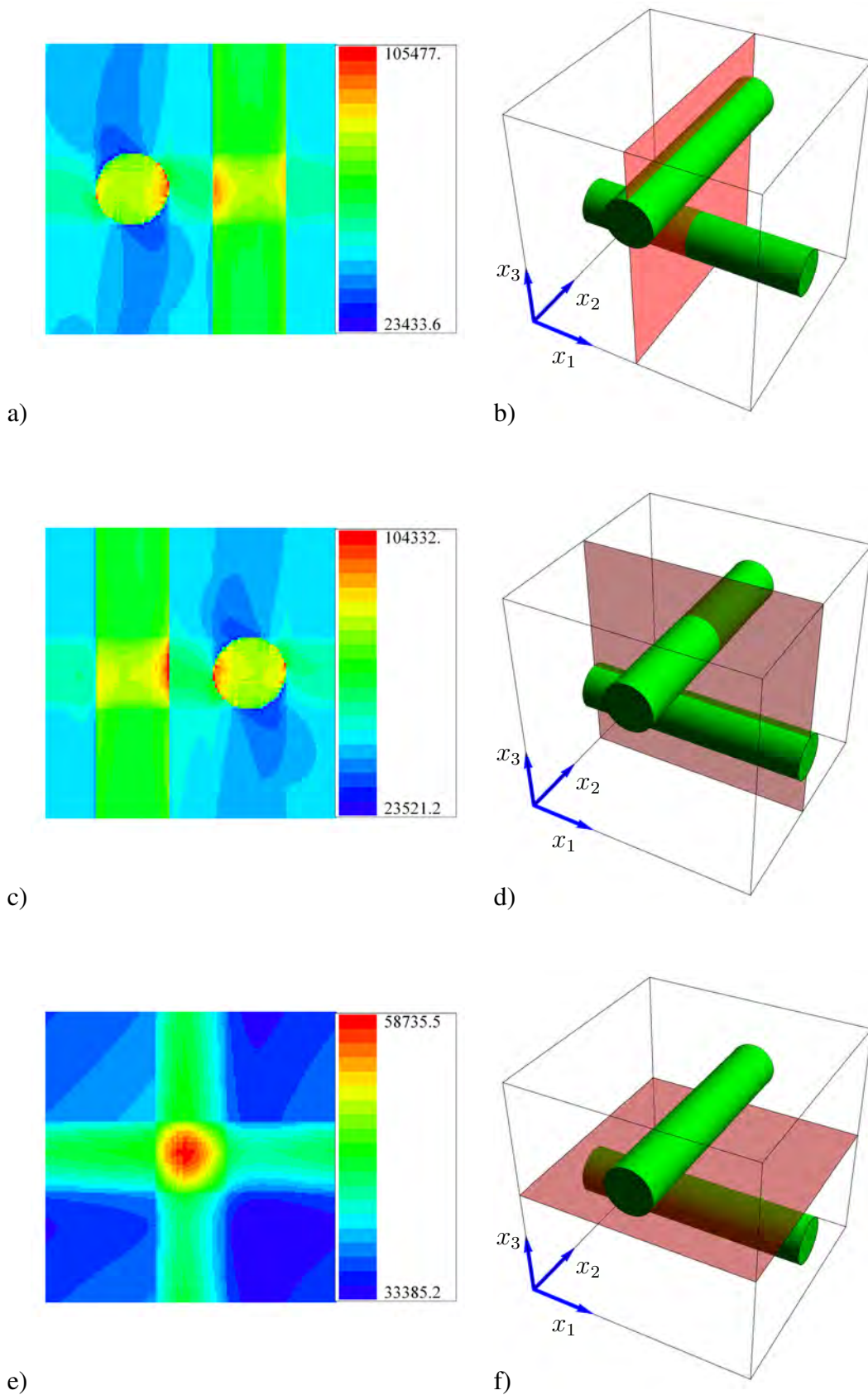
Fig. 5.8: Distribution of stress σ_{33} in planes in the middle of the RVE. Right side indicates the position of the plane that is displayed on the left side, respectively. View vectors: a) $\mathbf{v} = (1, 0, 0)^T$, b) $\mathbf{v} = (0, 1, 0)^T$, c) $\mathbf{v} = (0, 0, 1)^T$.

a)   b)

c)   d)

e)   f)

Fig. 5.9: Distribution of elastic energy ψ_0 in planes in the middle of the RVE. Right side indicates the position of the plane that is displayed on the left side, respectively. View vectors: a) $\mathbf{v} = (1, 0, 0)^T$, b) $\mathbf{v} = (0, 1, 0)^T$, c) $\mathbf{v} = (0, 0, 1)^T$.
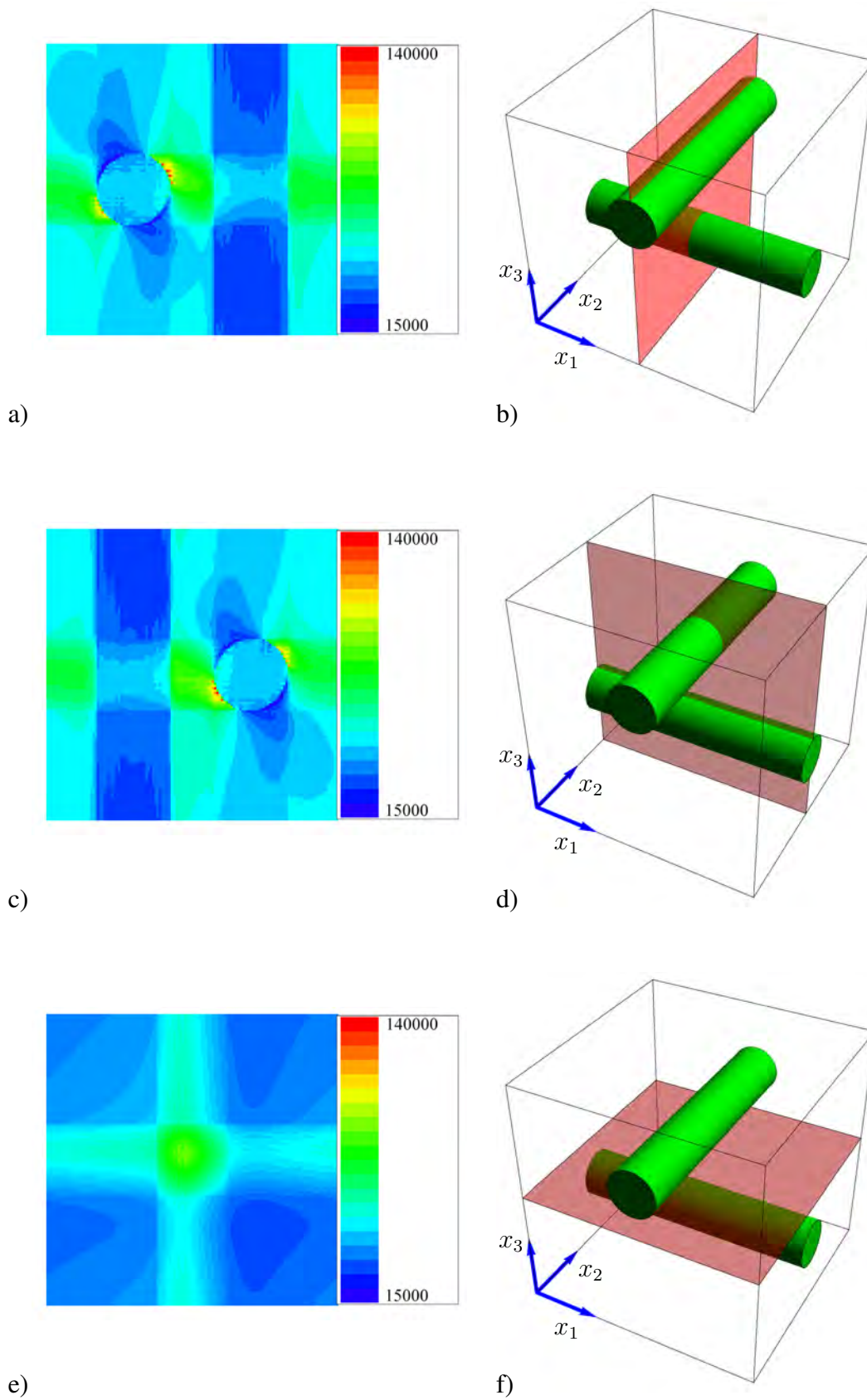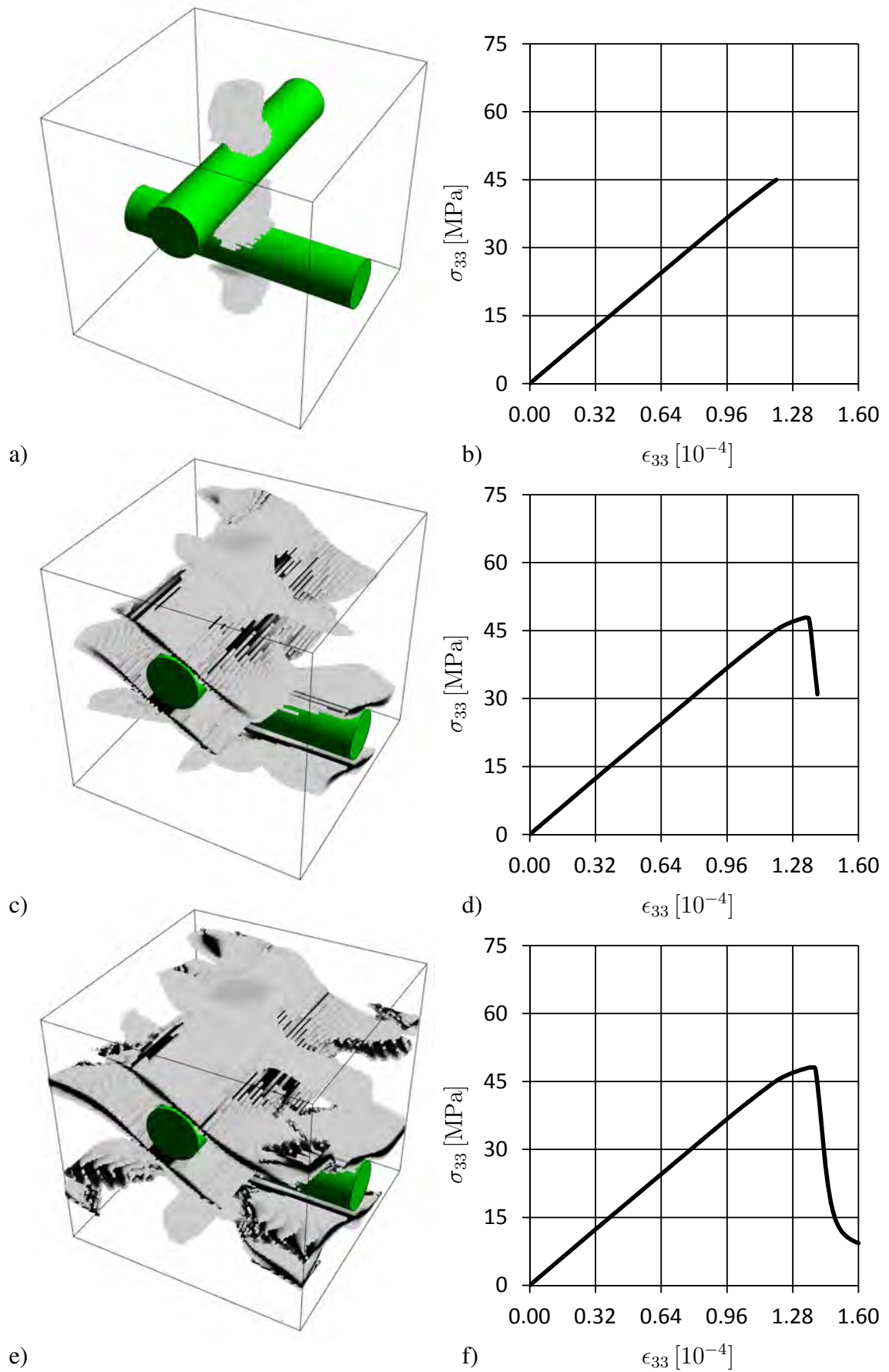
Fig. 5.10: Different states of damage evolution and corresponding stress-strain curve

A second example, with the same microstructure as the first one, has been analyzed. This time the load was changed in a way that the representative volume element is strained in direction of the fibers. This resembles the typical situation in shell concrete structures, where the steel reinforcements are located in a way that they can bear the bulk of the tensile load, to reduce tensile stresses in the concrete matrix. The applied strain is

$$\langle \boldsymbol{\epsilon} \rangle = (0.0012, 0.0012, -0.00072, 0, 0, 0)^T . \tag{5.16}$$

A pre analysis is again carried out by straining the RVE in purely elastic step with

$$\langle \boldsymbol{\epsilon} \rangle = (1, 1, -0.6, 0, 0, 0)^T , \tag{5.17}$$

and inspecting stresses and elastic energy. The results are depicted in fig. 5.11 and 5.12. The stresses σ_{11} are symmetric with respect to the rotation implied from fig. 5.12b) to 5.12d), thereby respecting the geometrical and physical symmetry of the problem. The distribution of the tensile stresses as well as the elastic energy shows little variation with respect to the maximum values that appear in the stiff fibers. It is necessary to reduce the step size in the numerical evaluation of the load path in order to catch the local influence of small peaks in the energy level. Step size was

$$\Delta \langle \boldsymbol{\epsilon} \rangle = 10^{-5} \langle \boldsymbol{\epsilon} \rangle , \tag{5.18}$$

thus slowing down calculations considerably compared to the previous example. It also becomes clear in advance that damage will originate close the fibers again, with stress peaks being good candidates for origination of crack like zones.

In fig. 5.13 the evolution of the three dimensional distribution of damage is demonstrated the same way as in fig. 5.10. The matrix material stiffness deteriorates in two plane layers that each includes one of the cylindrical inhomogeneities, respectively. Damage evolution is clearly non-local. The load curve in fig. 5.12d) shows a prepeak region where it deviates from the linear curve, showing an overall strong resistance to damage propagation. Finally the now well known, crack like patterns appear, starting at the boundaries of the cylinders and propagating into the yet undamaged regions of the matrix. A sudden drop in overall stiffness is recorded in the load curve (fig. 5.13f)). The representative volume element in this example acts stiffer than in the previous one, reaches almost the same peak in average tensile stresses, and drops in stiffness by approximately eighty percent.
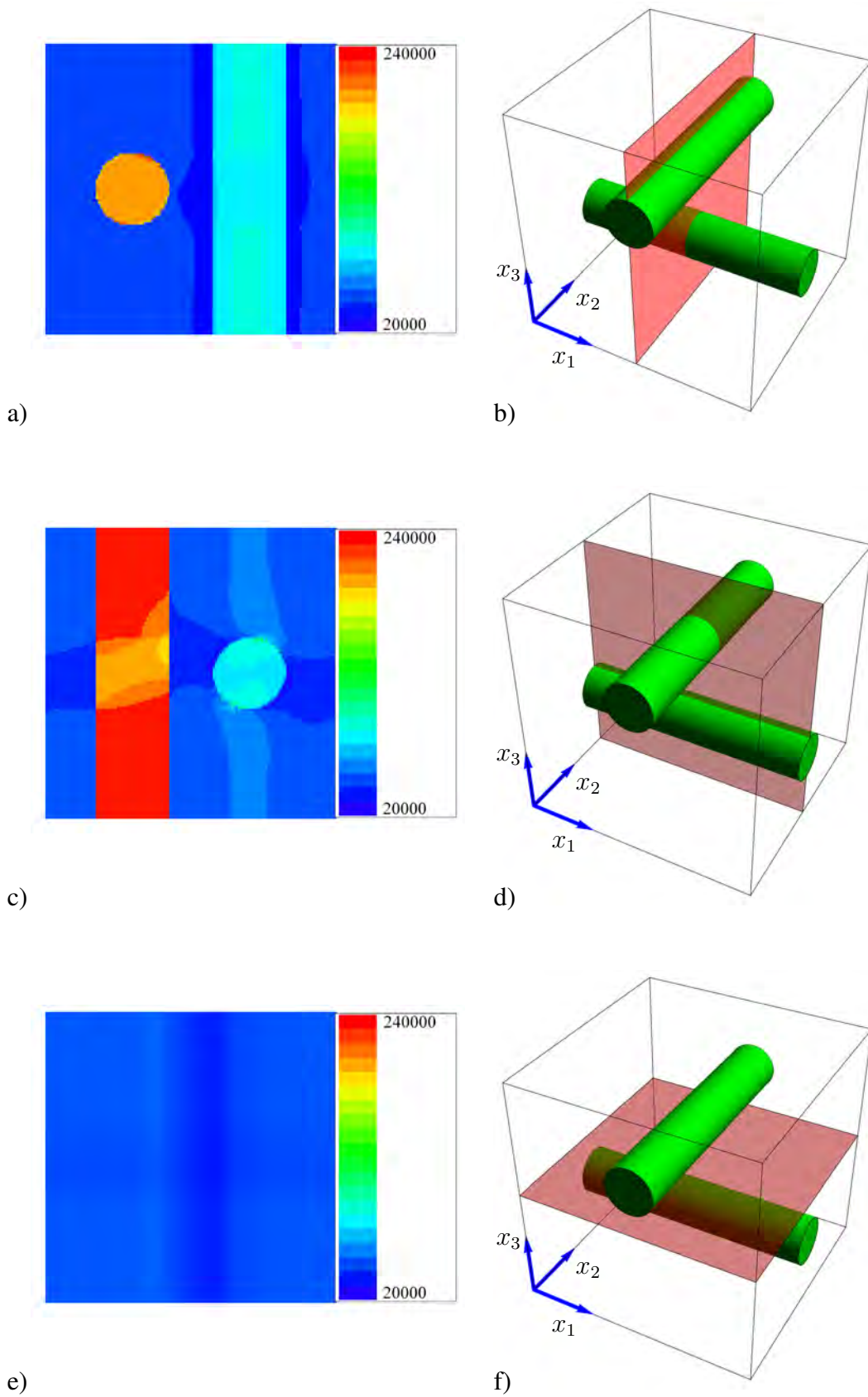
Fig. 5.11: Distribution of stress σ_{11} in planes in the middle of the RVE. Right side indicates the position of the plane that is displayed on the left side, respectively. View vectors: a) $\mathbf{v} = (1, 0, 0)^T$, b) $\mathbf{v} = (0, 1, 0)^T$, c) $\mathbf{v} = (0, 0, 1)^T$.

Fig. 5.12: Distribution of elastic energy ψ_0 in planes in the middle of the RVE. Right side indicates the position of the plane that is displayed on the left side, respectively. View vectors: a) $\mathbf{v} = (1, 0, 0)^T$, b) $\mathbf{v} = (0, 1, 0)^T$, c) $\mathbf{v} = (0, 0, 1)^T$.
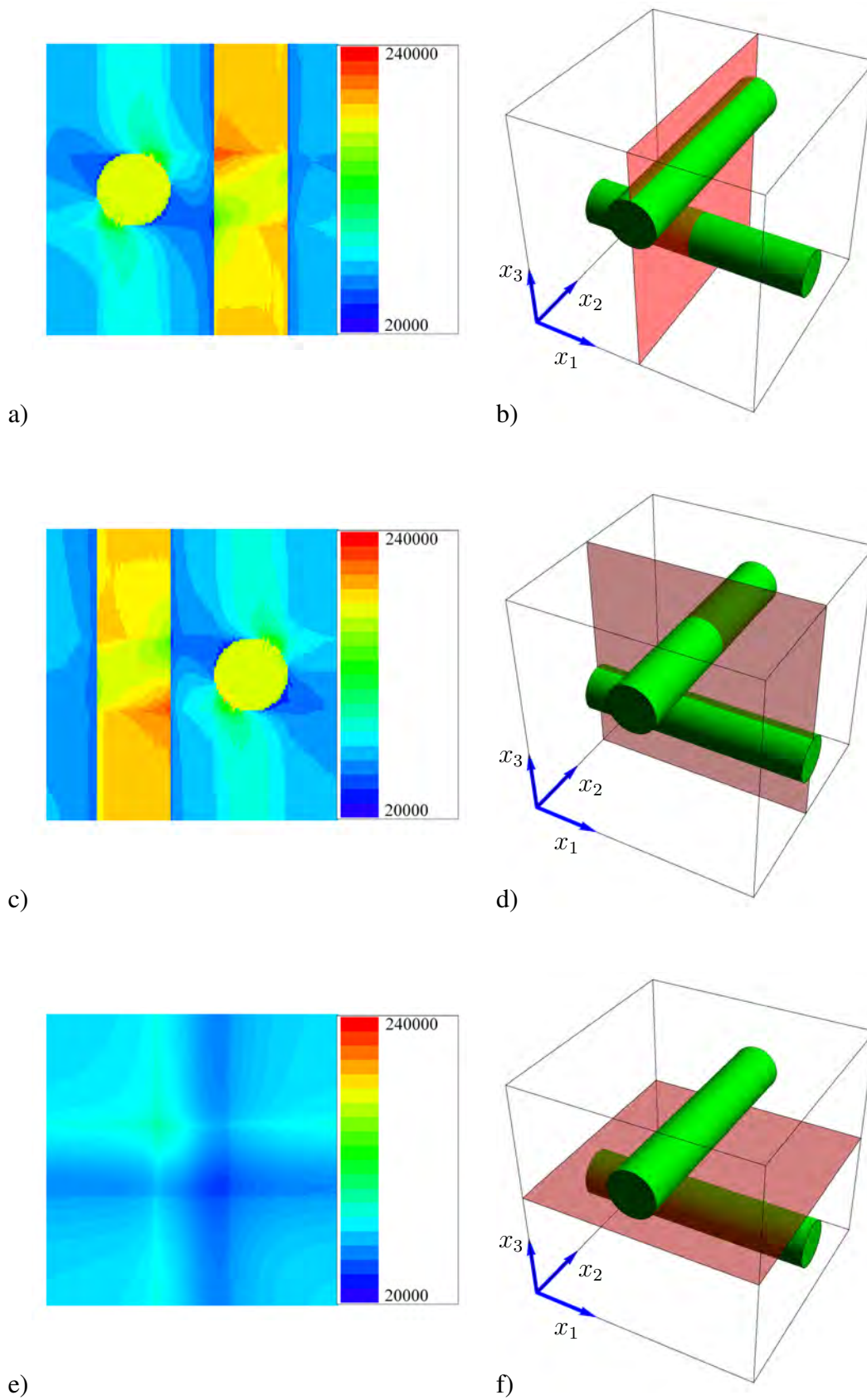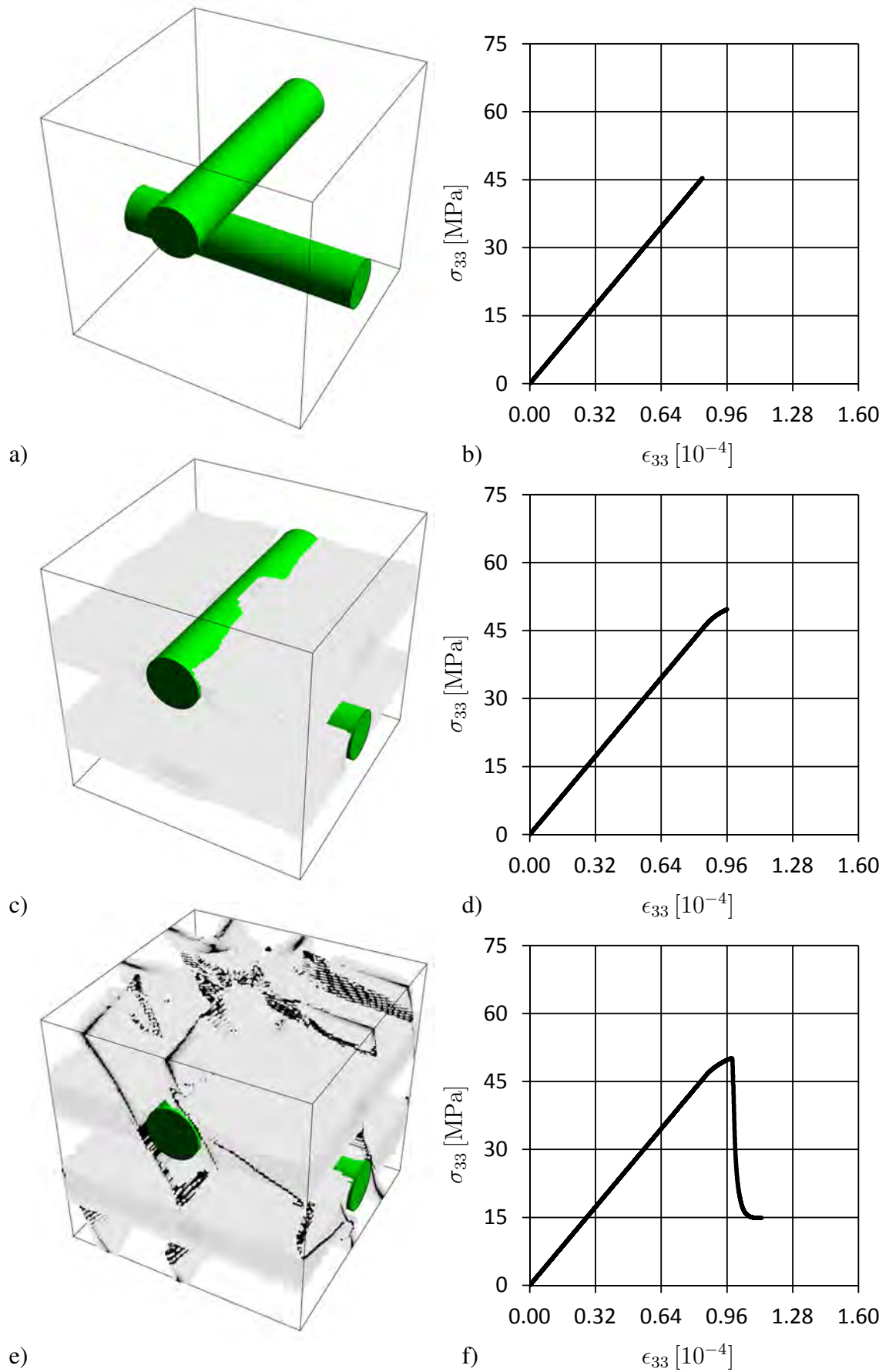
Fig. 5.13: Different states of damage evolution and corresponding stress-strain curve

5.3 Combination with Finite Element Analysis

The algorithm developed here has been formulated in discrete Fourier space because periodic microstructure was assumed at the starting point. This is a characteristic for problems involving multiple scales of different size. One example are structures made of reinforced steel, where the diameter of the reinforcing fibers is very small compared to the structure's overall dimensions. It is usually not affordable to directly simulate the structure with a resolution high enough to capture the effects on the length scale of these fibers. Nonetheless the behavior on the microscale often plays a role important enough to be incorporated in the analysis one way or the other. In the introduction to this thesis and in section 2.5 it was already mentioned that there are different methods to account for those effects. A straight forward approach to this problem is the use of the FE^2-Method or Multiscale Finite Element Method. The global structure is discretized with a coarse mesh, where coarse means not fine enough to capture the microscale geometry, and the stress-strain relationship at the integration points is calculated by another boundary value problem, namely an RVE subjected to periodic boundary conditions. Usually this second boundary value problem is analyzed with the Finite Element Method again, hence the name FE^2-Method, but any other numerical scheme may be employed. Since the algorithm that is the topic of this thesis automatically satisfies periodic boundary conditions, it may be directly implemented on the integration point level of a finite element analysis. Because of the advantages considering computational cost point out in the previous chapters it may be possible to save costs compared to the two fold Finite Element Method. In order to demonstrate this capability, an exemplary, rather simple problem has been solved this way, and its results are presented in this section.

The Finite Element Method is widely known as a tool to obtain approximate solutions to boundary value problems governed by elliptic partial differential equations. The weak formulation of the system of partial differential equations (2.13) reads:

$$\int\limits_{\Omega} \boldsymbol{\sigma} : \nabla \delta \mathbf{u}\, \mathrm{d}V = \int\limits_{\Omega} \mathbf{f} \cdot \delta \mathbf{u}\, \mathrm{d}V + \int\limits_{\partial\Omega} \mathbf{t} \cdot \delta \mathbf{u}\, \mathrm{d}A \qquad \forall \delta \mathbf{u}, \tag{5.19}$$

where $\delta \mathbf{u}$ is the variation (test function) of the displacement field. The domain to which the differential equations are restricted is divide into a finite number of z elements, connected to each other via nodes at the edges and bordering each other at their edge lines. The volume integral over the whole domain is split into z integrals over the subset occupied by the elements, respectively. The displacement field within each element is approximated by linear functions with unknown values at the nodes. The formulation of the transformed problem reads [13]:

$$\sum_{m=1}^{z} \int\limits_{\Omega_m} \mathbf{B}^T \cdot \mathbf{C} \cdot \mathbf{B}\, \mathrm{d}V = \sum_{m=1}^{z} \int\limits_{\Omega_m} \mathbf{N}_u \cdot \mathbf{f}\, \mathrm{d}V + \sum_{m=1}^{z} \int\limits_{\Omega_m} \mathbf{N}_u \cdot \mathbf{t}\, \mathrm{d}A, \tag{5.20}$$

where

$$\mathbf{B} = \begin{pmatrix} \frac{\partial}{\partial x_1} & 0 & 0 \\ 0 & \frac{\partial}{\partial x_2} & 0 \\ 0 & 0 & \frac{\partial}{\partial x_3} \\ 0 & \frac{1}{2}\frac{\partial}{\partial x_3} & \frac{1}{2}\frac{\partial}{\partial x_2} \\ \frac{1}{2}\frac{\partial}{\partial x_3} & 0 & \frac{1}{2}\frac{\partial}{\partial x_1} \\ \frac{1}{2}\frac{\partial}{\partial x_1} & \frac{1}{2}\frac{\partial}{\partial x_1} & 0 \end{pmatrix} \tag{5.21}$$

is a differential operator matrix, $\mathbf{C}$ is the stiffness tensor in Voigt notation (see sec. 2.2) and $\mathbf{N}_u$ is the matrix containing nodal values and information about the interpolated displacements. Eq . (5.20) may be rewritten in matrix notaion:

$$\mathbf{K} \cdot \widehat{\mathbf{u}} = \mathbf{f}_f + \mathbf{f}_t. \tag{5.22}$$

$\mathbf{K}$ is called stiffness matrix, $\mathbf{f}_f$ and $\mathbf{f}_t$ are the volumetric and superficial nodal forces and the vector $\widehat{\mathbf{u}}$ contains the unknown nodal values of the approximative displacement field to be solved for. A linear system of n equations has to be solved to obtain $\widehat{\mathbf{u}}$, where n is the number of nodes that depends on the number and definition of the finite elements. The elements of $\mathbf{K}$ are the results of the integrals in (5.20) which are calculated numerically by means of the Gauss integration procedure. For a detailed treatment of Finite Element Analysis in linear elasticity see [13], for example. A mathematically rigorous survey of the method, not restricted to the special case of continuum mechanics, can be found in [136].

The central idea of the FE^2-method is to solve an additional boundary value problem, consisting of a representative volume element, and use the volume average of the resulting stress and strain fields to compute the stress-strain response at Gauss point level, and use this results to calculate the entries of the stiffness matrix $\mathbf{K}$ [41, 49, 51, 52]. In general the mathematical problem becomes non-linear, and this is the case for damage mechanics treated in this work. The consequence is that the finite element scheme cannot be interpreted as system of linear equations, as in (5.22), because the element stiffness (and thus the global stiffness) depends on the solution $\mathbf{u}$:

$$\mathbf{K} = \mathbf{K}(\mathbf{u}). \tag{5.23}$$

The weak form of the problem is rewritten as

$$\mathbf{R_u} = \int_\Omega \mathbf{B}^t \cdot \boldsymbol{\sigma} \, \mathrm{d}V - \int_\Omega \mathbf{N_u} \cdot \mathbf{f} \, \mathrm{d}V - \int_{\partial\Omega} \mathbf{N_u} \cdot \mathbf{t} \, \mathrm{d}A \tag{5.24}$$

and $\mathbf{R_u}$ is called residual. For the solution of the problem it has to vanish:

$$\mathbf{R_u} = 0. \tag{5.25}$$

The Newton iterative scheme can be applied to find the solution $\mathbf{u}$:

$$\Delta\mathbf{u}^{i+1} = -\left(\frac{\partial\mathbf{R_u}^i}{\partial\mathbf{u}}\right)^{-1} \cdot \mathbf{R_u}^i. \tag{5.26}$$

As explained in section 2.5, a condition for the applicability of this method is that boundary conditions in stress and strains are periodic at the boundaries of the representative volume

element. The numerical algorithm studied here is formulated in discrete Fourier space, thus periodicity of all field variables is automatically implied. The results obtained with the algorithm are ready to use in a finite element analysis. In each iteration in (5.26) one loading step has to be calculated with the FFT algorithm, and the procedure has to be carried out at each Gauss point. It is typical for the Multiscale Finite Element Method that computational cost becomes large in terms of CPU time as well as memory requirements, and this case is no exception from the rule. However, the FFT-based algorithm still may save a lot of time, since no meshing of the microgeometry and no assembly of a stiffness matrix is necessary. Additionally, the large potential for parallelization of the algorithm will make results available in reasonable time at least on vector computer systems.

This section is concerned with a simple example that is chosen to demonstrate the general possibility of the combination of the two methods. A simple strip geometry is assumed with the axis of largest extension aligned with the x_3-axis of the reference coordinate system, which means that stress σ_{33} and ϵ_{33} act normal on a plane perpendicular to its longest extension. Tension in direction along the main strip axis is applied. On node of the outer plane is placed slightly off the plane in which the other nodes lie, to produce a disturbance in the otherwise homogeneous stress and strain fields in the strip. This triggers damage evolution in a location close to this point.

The stress-strain response on the macroscopic scale is calculated by comparison of the average stresses and strains that result from the submodel simulation. Although no damage variable is defined at a macroscopic level, a strain softening behavior is thus induced and mesh dependent results have to be expected. Results for strain ϵ_{33} for sample calculations that were run with different meshes are shown in figure 5.14. Two stages of the simulation are compared to each other, respectively. It is observed, that strain localizes around the displaced node, as expected. The geometrical extension of the localization is confined to the element size of the mesh, thus producing smaller localized zones with higher resolution. This fact reflects the expected mesh dependency. In figure 5.15 the force-displacement relationship, that can be extracted from the data obtained at the end of the strip that is subjected to displacement, is plotted. Although the results for the strain fields show mesh-dependent behavior, the curve for all three mesh arrangements have the same peak, and except some mesh dependent oscillations show the same mean behavior after the peak. After a drop of the curve it stabilizes and continues with a modest positive slope.
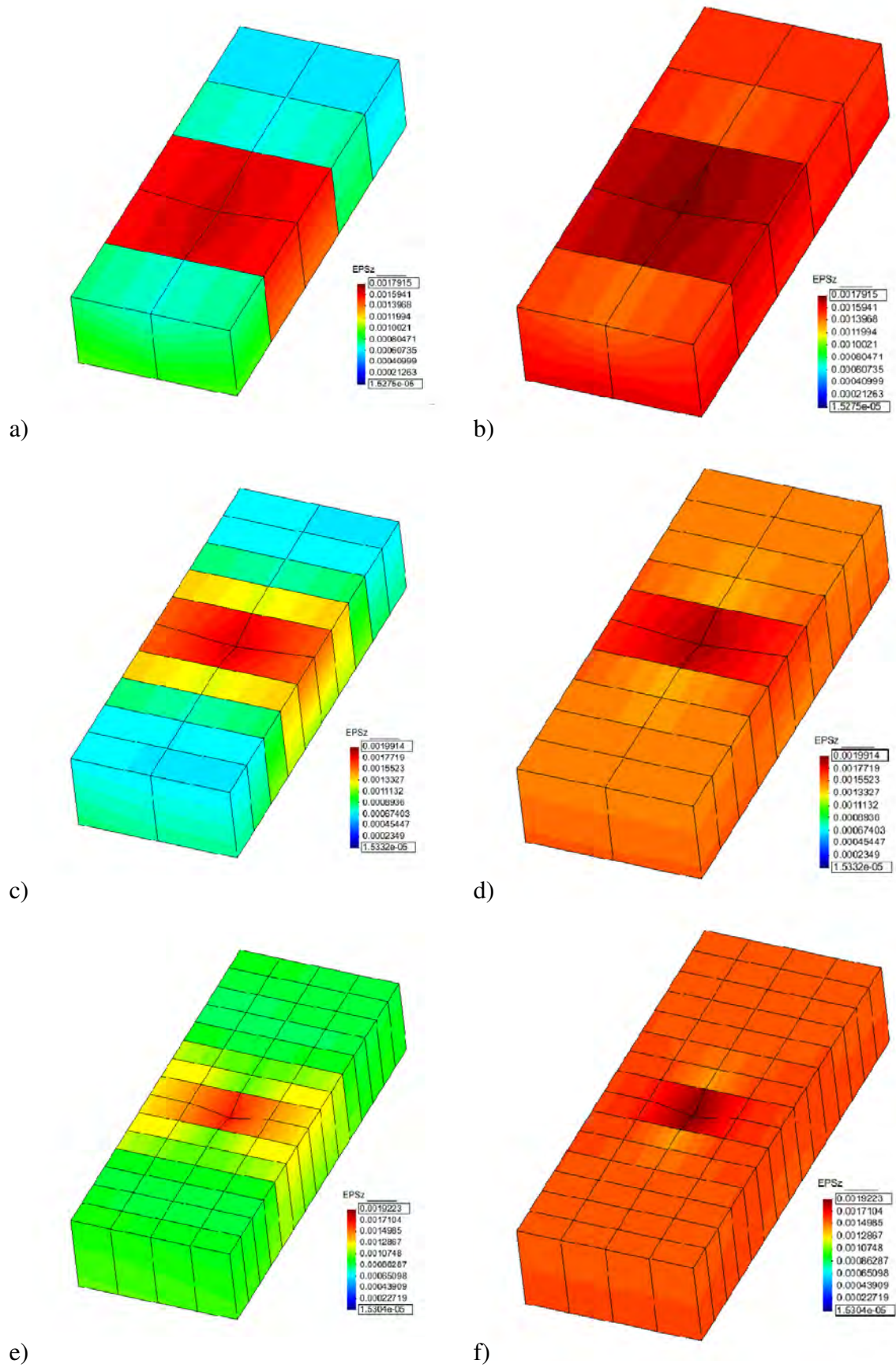
Fig. 5.14: Strain calculated with the Finite Element Method meshed with different resolution. $a)$ strain ϵ_{zz} after one third of loadpath, $b)$ strain ϵ_{zz} after two thirds of loadpath.
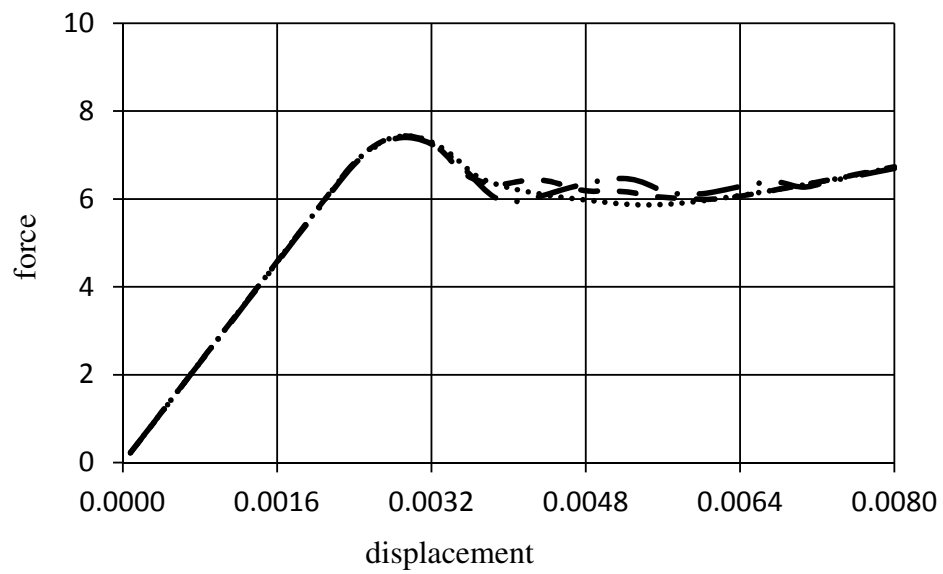
Fig. 5.15: Comparison of force-displacement curve for finite element calculations with varying resolution: 10 Elements (dash-dot line), 20 Elements (dashed line) and 30 Elements (dotted line).

6 Summary and Outlook

Throughout this work the implementation of a scalar valued damage model into FFT-based analyzing techniques has been studied. The development started with a review of the algorithm published by Moulinec and Suquet that had been designed to calculate the elastic response of composites with periodic microstructure. This algorithm is based on the fast Fourier transform of the corresponding (periodic) fields like stresses and strains, and takes advantage of the fact that the non-local integral representation of the linear elastic boundary value problem becomes local in Fourier space.

An expression for the Helmholtz free energy has been postulated. It consists of the elastic energy term, which includes the effective stress concept typical for damage models, and two additional terms that give the model a non-local character. An additional field variable φ is formulated, and the damage variable is linked to φ via a difference term, and a parameter that "'penalizes"' large differences between them. The second parameter penalizes the gradient of φ. These are measures to introduce an internal length to the model and make the results mesh independent. A dissipation potential in terms of $\dot{d}_+$ is also assumed. The principle of the minimum of the dissipation potential is applied and the equations that govern the process of damage evolution are found this way. The formulation yields a scalar valued equation and a partial differential equation of the Helmholtz kind for $f(d) = e^{-d}$ and φ. Application of the discrete Fourier transform changes the Helmholtz equation into a local, multiplicative operator, and this is what makes the formulation especially suitable for implementation into a numerical scheme that is based on the fast Fourier transform, as is the algorithm by Suquet. A numerical scheme is developed to provide results for composites with a periodic microstructure.

Following the assessment of the governing equations and of the numerical algorithm, the propagation of numerical uncertainty throughout the procedure was investigated. Direct expressions for the uncertainty were used where they were available, i.e. for steps that only involve simple addition or multiplication. To get an idea about the uncertainty of the involved fast Fourier transform, it has been applied to several trial fields, and the inverse transform has been applied thereafter. The original data could be compared to the manipulated data, and hence the error between both could be established. An estimate for the uncertainty of one iteration step has been given, and it has been shown that the error remains small for reasonable numbers of iterations. This contributes to the stability of the algorithm.

To demonstrate the power of the algorithm, some examples with simple geometry were analyzed and the results presented. A high number of degrees of freedom (above two million) were given in the three dimensional examples and still the algorithm was capable of simulating a complete load path within a couple of hours on a single core machine. It has been demonstrated that the load curve converges for increasingly detailed discretization, showing no sign of mesh dependent behavior. The microstructural damage patterns that involve during the load path assume finite dimensions, covering more than one sample point in width when the discretization is fine enough to reproduce it. Furthermore it has been shown that

the resulting stress and strain field as well as the damage pattern are truly periodic, and the solution does not depend on the position the representative volume element assumes relative to the microstructure of the material. This is an important property when the use within a multiscale finite element approach is envisioned. The relationship between the averaged stresses and strains resembles typical load curves of materials that tend to quasi brittle failure. By adjustment of three independent model parameters it is possible to calibrate the model behavior between a very brittle behavior towards a more restrained one that shows high resistance to material deterioration . Two of these parameters (labeled α and β throughout this work) are connected to the regularizing terms in the free energy, and the third one is the dissipation rate r. Finally a simple example was given where a three dimensional structure was analyzed with a MsFEM ansatz, to prove the general possibility of this approach. Although mesh dependence occurs in the macroscopic strain fields, because of the strain softening material character at the integration points, the overall force-displacement relationship does not show this behavior.

It can be said that the goal that was carved out in the introduction of this thesis has been accomplished so far. The suitability of FFT based numerical analysis for damage models has been demonstrated, and a model and a numerical algorithm are available now that are capable to reproduce the basic phenomena of isotropic damage. It is now time to briefly outline possible directions for future progress.

Only composites whose constituents all behave elastically isotropic can be analyzed with the current implementation. However, there are no theoretical constraints against including anisotropic phases in the formulation. The reference material, and hence the Greens operator can still be isotropic, although use of an anisotropic reference medium might accelerate convergence for complex problems. The complexity of the numerical problem increases linearly with the increase of elastic parameters, as does the size of the input data and the memory requirements of the procedure. Usually memory is no limiting property on modern 64 bit multi core computers. It has to be mentioned that for anisotropic materials the orientation of symmetry axes relative to the reference coordinate system has to be accounted for, which means that additionally to the elastic parameters it might be necessary to save information about the corresponding directions of material principal axes.

Another enhancement of the formulation presented here could be the introduction of a more sophisticated damage model. Several damage variables can be included, each to model different aspects of damage like fiber-breakage, tensile or shear mode fracture or crack closure effects under pressure conditions. Instead of a scalar damage variable a tensorial one may be considered to model anisotropic damage evolution. In this case the strength of the introduction of an additional field variable comes really into play, because all components of the damage tensor can be linked to it, and thus it is not necessary to calculate the gradient of a tensorial quantity throughout the numerical procedure. The same holds true in case of non-local plasticity models, that are usually based on the gradient of the plastic strain in the literature. ´

Bibliography

[1] J. E. Aarnes and Y. Efendiev. Mixed multiscale finite element methods for stochastic porous media flows. *SiAM Journal on Scientific Computation*, 30(5):2139–2339, 2008.

[2] J. E. Aarnes, V. Kippe, and K.-A Lie. Mixed multiscale finite elements and streamline methods for reservoir of large geomodels. *Advances in Water Resources*, 28(3):257–271, 2005.

[3] M.M Abdel Wahab, I.A Ashcroft, A.D Crocombe, and S.J Shaw. Prediction of fatigue thresholds in adhesively bonded joints using damage mechanics and fracture mechanics. *Journal of Adhesion Science and Technology*, 15(7):763–781, 2001.

[4] G. Allaire and R. Brizzi. A multiscale finite element method for numerical homogenization. *Multiscale Modeling and Simulation*, 4(3):790–812, 2005.

[5] D. H. Allen. Homogenization principles and their application to continuum damage mechanics. *Composite Science and Technology*, 61(15):2223–2230, 2001.

[6] M. Alves, J. Yu, and N. Jones. On the elastic modulus degradation in continuum damage mechanics. *Computers & Structures*, 76(6):703–712, 2000.

[7] T. L. Anderson. *Fracture mechanics: Fundamentals and applications*. CRC Taylor & Francis, Boca Raton, 3rd edition, 2005.

[8] F. Ansari. Stress-strain response of microcracked concrete in direct tension. *ACI Materials Journal*, 84(6):481–490, 1987.

[9] T. Arbogast, G. Pencheva, M. F. Wheeler, and I. Yotov. A multiscale mortar mixed finite element method. *Multiscale Modeling and Simulation*, 6(1):319–346, 2007.

[10] K.E Atkinson. *An Introduction to Numerical Analysis*. John Wiley & Sons LTD, 2nd edition, 1988.

[11] I. Babuška, J. R.t Whiteman, and T. Strouboulis. *Finite elements: An introduction to the method and error estimation*. Oxford Univ. Press, Oxford, 2011.

[12] D.M Barnett. The precise evaluation of derivatives of the anisotropic elastic green's functions. *Phyisca Status Solidi (b)*, 49(741-748), 1972.

[13] K. J. Bathe and E. L. Wilson. *Numerical Methods in Finite Element Analysis*. Prentice-Hall, New Jersey, 1st edition, 1976.

[14] Z. P. Bazant. Mechanics of distributed cracking. *Applied Mechanics Reviews*, 39(5):675–705, 1986.

[15] Z. P. Bazant. Scaling laws in mechanics of failure. *Journal of Engineering Mechanics*, 119(9):1828–1844, 1993.

[16] Z. P. Bazant and L. Cedolin. Blunt crack band propagation in finite element analysis. *Journal of the Engineering Mechanics Division*, 105(2):297–315, 1979.

[17] Z. P. Bazant and L. Cedolin. Fracture mechanics of reinforced concrete. *Journal of the Engineering Mechanics Division*, 106(2):1287–1306, 1980.

[18] Z. P. Bazant and D. Novak. Energetic-statistical size effect in quasibrittle failure at crack initiation. *ACI Materials Journal*, 97(3):381–392, 2000.

[19] Z. P. Bazant and Oh B.H. Crack band theory for fracture of concrete. *Materials and Structures*, 16(3):155–177, 1983.

[20] Z. P. Bazant and J. Eligehausen R. Ozbolt. Fracture size effect: Review of evidence for concrete structures. *Journal of Structural Engineering*, 120(8):2377–2398, 1994.

[21] Zdenek P. Bazant and L. Cedolin. Fracture mechanics of reinforced concrete. *Journal of the Engineering Mechanics Division*, 106(2):1287–1306, 1980.

[22] Y. Benveniste, G.J Dvorak, and T. Chen. On diagonal and elastic symmetry of the approximate effective stiffness tensor of heterogeneous media. *Journal of the Mechancis and Physics of Solids*, 39(7):927–946, 1991.

[23] J. M. Blackledge. *Digital signal processing: Mathematical and computational methods, software development, and applications*. Horwood, Chichester, 2003.

[24] B. Budiansky. On the elastic moduli of some heterogeneous materials. *Journal of the Mechancis and Physics of Solids*, 13:223–227, 1965.

[25] B. Budiansky and J. R. O'Connel. Elastic moduli of a cracked solid. *International Journal of Solids and Structures*, 12:81–97, 1976.

[26] J.-L Chaboche. Continuous damage mechanics - a tool to describe phenomena before crack initiation. *Nuclear Engineering and Design*, 64(2):233–247, 1981.

[27] A. Chudnovsky. Crack layer theory: Report to national aeronautics and space administration, nasa report no. 174631, 1984.

[28] A. Chudnovsky and M. Kachanov. Interaction of a crack with a field of microcracks. *International Journal of Engineering Science*, 21(8):1009–1018, 1983.

[29] A. Chudnovsky and A. Moet. Thermodynamics of translational crack layer propagation. *Journal of Materials Science*, 20(2):630–635, 1985.

[30] J.W Cooley and J.W Tukey. An algorithm for the machine calculation of complex fourier series. *Mathematics of Computation*, 19:297–301, 1965.

[31] V. Dattoma, S. Giancane, R. Nobile, and F.W Panella. Fatigue life prediction under variable loading based on a new non-linear continuum damage mechanics model. *International Journal of Fatigue*, 28(2):89–95, 2006.

[32] R. deBorst and J. Pamin. Some novel developments in finite element procedures for gradient-dependent plasticity. *International Journal for Numerical Methods in Engineering*, 39:2477–2505, 1996.

[33] O.W Dillon Jr. and J. Kratochvil. A strain gradient based theory of plasticity. *International Journal of Solids and Structures*, 6(12):1513–1533, 1970.

[34] B. Dimitrijevic and K. Hackl. A method for gradient enhancement of inelsatic material models. *Proccedings of First South-East European Conference on Computational Mechanics*, pages 191–197, 2006.

[35] B. Dimitrijevic and K. Hackl. A method for gradient enhancement of continuum damage models. *Technische Mechanik*, 28(1):43–52, 2008.

[36] B. Dimitrijevic and K. Hackl. A regularization framework for damage-plasticity models via gradient enhancement of the free energy. *Numerical Methods in Biomedical Engineering*, 27(8):1199–1210, 2011.

[37] Y. Efendiev, V. Ginting, T.Y Hou, and R. Ewing. Accurate multiscale finite element methods for two-phase flow simulations. *Journal of Computational Physics*, 220(1):155–174, 2006.

[38] Y. Efendiev and T.Y Hou. *Multiscale Finite Element Methods: Theory and Applications*. Surveys and Tutorials in the Applied Mathematical Sciences. Springer, 2009.

[39] Y. Efendiev, T.Y Hou, and X.-H Wu. Convergence of a nonconforming multiscale finite element method. *SIAM Journal of Numerical Analysis*, 37(3):888–910, 2000.

[40] Y. Efendiev and X.-H Wu. Multiscale finite elements for problems with highly oscillatory coefficients. *Nummerische Mathematik*, 90(3):459–486, 2002.

[41] B. Engquist, O. Runborg, and P. Lötstedt. *Multiscale Methods in Science and Engineering*. Springer-Verlag, s.l, 1 edition, 2005.

[42] F. Erdogan and G.C Sih. On the crack extension in planes under plane loading and transverse shear. *Journal of Basic Engineering*, 85:519–527, 1963.

[43] A.C Eringer and D.G.B Edelen. On nonlocal elasticity. *International Journal of Engineering Science*, 10(3):233–248, 1972.

[44] J. D. Eshelby. The determination of the elastic field of an ellipsoidal inclusion, and related problems. *Proceedings of the Royal Society A: Mathematical, Physical and Engineering Sciences*, 241(1226):376–396, 1957.

[45] R.H Evans and M.S Marathe. Microcracking and stress-strain curves for concrete in tension. *Materials and Structures*, 1(1):61–64, 1968.

[46] D.J Eyre and G.W Milton. A fast numerical scheme for computing thte response of composites using grid refinement. *The European Physical Journal Applied Physics*, 6(1):41–47, 1999.

[47] G. Faivre. Déformations de cohérence d'un précipité qudratique. *phyisca status solidi (b)*, 35(1):249–259, 1969.

[48] J. Fish. Multiscale damage modeling for composite materials: theory and computational framework. *International Journal for Numerical Methods in Engineering*, 52(1-2):161–191, 2001.

[49] J. Fish. *Multiscale methods: Bridging the scales in science and engineering*. Oxford Univ. Press, Oxford, 2010.

[50] R. M.L Foote, Y.-W Mai, and B. Cotterell. Crack growth resistance curves in strain-softening materials. *Journal of the Mechancis and Physics of Solids*, 34(6):593–607, 1986.

[51] U. Galvanetto and M. H. Aliabadi. *Multiscale modeling in solid mechanics: Computational approaches*, volume 3 of *Computational and experimental methods in structures*. Imperial College and Distributed by World Scientific, London and London and New York, 2010.

[52] B. Gambin, J. J. Telega, and P. Castañeda. *Nonlinear homogenization and its applications to composites, polycrystals and smart materials*, volume 170 of *NATO science series. Series II, Mathematics, physics, and chemistry*. Kluwer Academic Publishers, Dordrecht and London, 2004.

[53] A.C Gavazzi and D.C Lagoudas. On the numerical evaluation of eshelby's tensor and its application to elastoplastic fibrous composites. *Computational Mechanics*, 7:13–19, 1990.

[54] W.W Gentleman and G. Sande. Fast fourier transform for fun and profit. *Proc. AFIPS*, 29:563–578, 1966.

[55] P. Germain, Q.S Nguyen, and P. Suquet. Continuum thermodynamics. *Transactions of the ASME*, 50:1110–1120, 1983.

[56] J. Gomez and C. Basaran. A thermodynamics based damge mechanics constitutive model for low cycle fatigue analysis of microelectronics solder joints incorporating size effects. *International Journal of Solids and Structures*, 42(13):3744–3772, 2005.

[57] V.S Gopalaratnam and S.P Shah. Softening response of plain concrete in direct tension. *Journal Proceedings of American Concrete Institute*, 82(3):310–323, 1985.

[58] A.E Green and R.S Rivlin. Multipolar continuum mechanics. *Archive For Rational Mechanics And Analysis*, 17(2):113–147, 1964.

[59] A.A Griffith. The phenomena of rupture and flow in solids. *Philosophical Transactions A*, 221:163–198, 1920.

[60] Z.-Y Guo and Z.-X Li. Size effect on single-phase channel flow and heat transfer at microscale. *International Journal of Heat and Fluid Flow*, 24(3):284–298, 2003.

[61] M.E Gurtin. The linear theory of elasticity. In *Mechanics of Solids*, volume 2, pages 1–273.

[62] M.E Gurtin. *An Introduction to Continuum Mechanics*, volume 158 of *Mathematics in Science and Engineering*. Academic Press, New York, 1981.

[63] K. Hackl and F.D Fischer. On the relation between the principle of maximum dissipation and inelastic evolution given by dissipation potentials. *Proceedings of the Royal Society A: Mathematical, Physical and Engineering Sciences*, 464:117–132, 2008.

[64] Z. Hashin and S. Shtrikman. On some variational principles in anisotropic and non-homogeneous elasticity. *Journal of the Mechancis and Physics of Solids*, 10:335–342, 1962.

[65] M. Hayes. A simple statical approach to the measurement of the elastic constants in anisotropic media. *Journal of Materials Science*, 4:10–14, 1969.

[66] R.F.S Hearmon. *An Introduction to Applied Anisotropic Elasticity*. Oxford University Press, Oxford, 1961.

[67] R. Hill. The elastic behavior of a crystalline aggregate. *Journal of the Mechancis and Physics of Solids*, 11:359–354, 1963.

[68] R. Hill. Elastic properties of reinforced solids: some principles. *Journal of the Mechancis and Physics of Solids*, 11:372–357, 1963.

[69] J.B Hiriart-Urruty and C. Lemaréchal. *Fundamentals of convex analysis*. Grundlehren Text Editions. Springer, Berlin, 2nd edition, 2004.

[70] T. Ichimura, M. Hori, and H. Kuwamoto. Earthquake motion simulation with multiscale finite-element analysis on hybrid grid. *Bulletin of the Seismological Society of America*, 97(4):1133–1143, 2007.

[71] C.E Inglis. Stresses in a plate due to the presence of cracks and sharp corners. *Transactions of Institute of Naval Architects*, 55:219–241, 1913.

[72] G.R Irwin. Onset of fast crack propagation in high strength steel and aluminium alloys. *Sagamore Research Conference Proceedings*, 2:289–305, 1956.

[73] M. Jirasek. Nonlocal models for damage and fracture: Comparison of approaches. *International Journal of Solids and Structures*, 35:4133–4145, 1998.

[74] J.W Ju and L.Z Sun. A novel formulation for the exterior-point eshelby's tensor of an ellipsoidal inclusion. *Transactions of the ASME*, 66:570–574, 1999.

[75] P. Junker and K. Hackl. Finite element simulations of poly-crystalline shape memory alloys based on a micromechanical model. *Computational Mechanics*, 47(5):505–517, 2011.

[76] M. Kachanov. On the time to failure uder creep conditions. *Otd. Tekhn. Nauk*, 8:26–31, 1958.

[77] V.G Kouznetsova, M. G.D. Geers, and W.A.M Brekelmans. Multi-scale second-order computational homogenization of multi-phase materials: a nested finite element solution strategy. *Computer Methods in Applied Mechanics and Engineering*, 193(48-51):5525–5550, 2004.

[78] V.G Kouznetsova, M.G.D Geers, and W. A.M. Brekelmans. Computational homogenisation for non-linear heterogeneous solids. In *Multiscale Modeling in Solid Mechanics*, volume 3, pages 1–42.

[79] D. Krajcinovic. Damage mechanics: acomplishment, trends and needs. *International Journal of Solids and Structures*, 37(1-2):267–277, 2000.

[80] E. Kröner. Berechnung der elastischen konstanten des vielkristalls aus den konstanten des einkristalls. *Zeitschrift für Physik*, 151:504–518, 1958.

[81] E. Kröner. Elasticity theory of materials with longrange cohesive forces. *International Journal of Solids and Structures*, 3:731–742, 1968.

[82] E. Kröner. *Statistical continuum mechanics: Course held at the Department of General Mechanics, October 1971*, volume 92 of *Courses and lectures / International Centre for Mechanical Sciences*. Springer, Wien, 1972.

[83] R.A Lebensohn and P. Castañeda. On the accuracy of the self-consistent approximation for polycrystals: comparison with full-field numerical simulations. *Acta Materialia*, 52(18):5347–5361, 2004.

[84] R.A Lebensohn, M. Montagnat, P. Mansuy, P. Duval, and A. Meysonnier. Modeling viscoplastic behavior and hoeterogeneous intracrystalline deformation of comlumnar ice polycrystals. *Acta Materialia*, 57(5):1405–1415, 2009.

[85] H. Lee, J. Daniel, and Y. Kim. Continuum damage mechanics-based fatigue model of asphalt concrete. *Journal of Materials in Civil Engineering*, 12(2):105–112, 2000.

[86] J.K Lee, D.M Barnett, and H.I Aaronson. The elastic strain energy of coherent ellipsoidal precipitates in anisotropic crystalline solids. *Metallurgical and Materials Transactions A*, 8(6):963–970, 1977.

[87] S.G Lekhnitskii. *Theory of Elasticity of an Anisotropic elastic body: Translated by P. Fern*. Holden-Day, San Francisco, 1963.

[88] J. Lemaitre. How to use damage mechanics. *Nuclear Engineering and Design*, 80:233–245, 1984.

[89] J. Lemaitre and R. Desmorat. *Engineering Damage Mechanics: Ductile, Creep, Fatigue and Brittle Failures.* Springer-Verlag, Berlin and Heidelberg, 2005.

[90] F. Li and Z. Li. Continuum damage mechanics based on modeling of fiber reinforced concrete in tension. *International Journal of Solids and Structures*, 38(5):777–793, 2000.

[91] Victor C. Li, C.-M Chan, and C.K.Y Leung. Experimental determination of the tension-softening relations for cementitious composites. *Cement and Concrete Research*, 17(3):441–452, 1987.

[92] E. Lorentz and A. Benallal. Gradient constitutive relations: numerical aspects and application to gradient damage. *Computer Methods in Applied Mechanics and Engineering*, 194:5191–5220, 2005.

[93] A.E Love. *A Treatise on the Mathematical Theory of Elasticity*. Dover Publications, New York, 4th edition, 1927.

[94] J. E. Luco and R. J. Apsel. On the green's functions for a layered half-space. part i. *Bulletin of the Seismological Society of America*, 73(4):909–929, 1983.

[95] I.G Main. A damage mechanics model for power-law creep and earthquake aftershock and foreshock sequences. *Geophysical Journal International*, 142:151–161, 2000.

[96] X. Markenscoff. On the shape of the eshelby inclusions. *Journal of Elasticity*, 49(2):163–166, 1997.

[97] X. Markenscoff and V.A Lubarda. On the absence of eshelby property for non-ellipsoidal inclusions. *International Journal of Solids and Structures*, 35(25):3405–3411, 1998.

[98] A. Masud and R. A. Khurram. A multiscale fintie element method for the incompressible navier-stokes equations. *Computer Methods in Applied Mechanics and Engineering*, 195(13-16):1750–1777, 2006.

[99] J. Mazars and G. Pijaudier-Cabot. From damage mechanics to fracture mechanics and conversely: a combined approach. *International Journal of Solids and Structures*, 33(20):3327–3342, 1996.

[100] M.M Mehrabadi and S.C Cowin. Eigentensors of linera anisotropic elastic materials. *Quarterly Journal of Mechanics and Applied Mathematics*, 43(1):15–41, 1990.

[101] A. Menzel and P. Steinmann. A theoretical and computational framework for anisotropic continuum damage mechanics at large strains. *International Journal of Solids and Structures*, 38(52):9505–9523, 2001.

[102] R.D Mindlin. Second gradient of strain and surface-tension in linear elasticity. *International Journal of Solids and Structures*, 1(4):417–438, 1965.

[103] R.D Mindlin. On first strain-gradient theories in linear elasticity. *International Journal of Solids and Structures*, 4(1):109–124, 1968.

[104] T. Mori and K. Tanaka. Average stress in matrix and average elastic energy of materials with misfitting inclusions. *Acta Metallurgica*, 21(5):571–574, 1973.

[105] H. Moulinec and P. Suquet. A fast numerical method for compouting the linear and nonlinear mechanical properties of composites. *Comptes rendus d l'Académie des sciences. Série II, Mécanique, physique, chimie, astronomie*, 318(11):1417–1423, 1994.

[106] H. Moulinec and P. Suquet. A numerical method for computing the overall response of nonlinear composites with complex microstructure. *Computer Methods in Applied Mechanics and Engineering*, 157(1-2):69–94, 1998.

[107] H. Moulinec and P. Suquet. Comparison of fft-based methods for computing the response of composites with highly contrasted mechanical properties. *Physica B: Condensed Matter*, 338:58–60, 2003.

[108] T. Mura. *Micromechanics of defects in solids*, volume 3 of *Mechanics of elastic and inelastic solids*. Kluwer Acad. Publ, Dordrecht, 2 edition, 1982.

[109] K.Z Najo, D.L Turcotee, and R. Shcherbakov. A model of damage mechanis for the deformation of the continental crust. *Journal of Geophysical Research*, 110, 2005.

[110] S. Nemat-Nasser and M. Hori. *Micromechanics: Overall properties of heterogeneous materials*. Elsevier, Amsterdam, 2. rev. ed., transferred to digital print. 2006 edition, 2010.

[111] A. Neubauer. *DFT - Diskrete Fourier-Transformation: Elementare Einführung*. Studium. Springer Vieweg, Wiesbaden, 2012.

[112] G. D. Nguyen. *A Thermodynamic Approach to Constitutive Modelling of Concrete using Damage Mechanics and Plasticity Theory: Doctoral Thesis*. 2005.

[113] S. F. Oberman. Floating point division and square root algorithms and implementation in the amd-k7. *Proceedings of the IEEE Symposium on Computer Arithmetic*, pages 106–115, 1999.

[114] M. Ohlberger. A posteriori error estimate for the heterogeneous multiscale finite element method for elliptic homogenization problems. *Multiscale Modeling and Simulation*, 4(1):88–114, 2006.

[115] E. Pan. Static green's functions in multilayered half spaces. *Applied Mathematical Modeling*, 21:509–521, 1997.

[116] Y.-C Pan and T.-W Chou. Point force solution for an infinite transversely isotropic solid. *Transactions of the ASME*, pages 608–612, 1976.

[117] R. H.J. Peerlings, R. de Borst, W. A.M. Brekelmans, and M. G.D. Geers. Gradient-

enhanced damage modelling of concrete fracture. *Mechanics of Cohesive Materials*, 3(4):323–342, 1998.

[118] R. H.J. Peerlings, R. deBorst, W. A.M. Brekelmans, and J. H.P. deVree. Gradient enhanced damage for quasi-brittle materials. *International Journal for Numerical Methods in Engineering*, 39(19):3391–3403, 1996.

[119] R.H.J Peerlings, M.G.D Geers, R. de Borst, and W.A.M Brekelmans. A critical comparison of nonlocal and gradient-enhanced softening continua. *International Journal of Solids and Structures*, 38(44-45):7723–7746, 2001.

[120] I.J Perrin, D.R Hayhurst, and R.A Ainsworth. Approximate creep rupture lifetimes for butt welded ferritic steel pressurised pipes. *European Journal of Mechanics - A/Solids*, 19(2):223–258, 2000.

[121] G. Pijaudier-Cabot and Z. P. Bazant. Nonlocal damage theory. *Journal of Engineering Mechanics*, 113:1512–1533, 1987.

[122] S. Popovics. A review of stress-strain relationships for concrete. *Journal Proceedings of American Concrete Institute*, 67(3):243–248, 1970.

[123] Rabotnov. Creep rupture. *Proc. XII Internat. Cong. Appl. Mech.*, 1968.

[124] A. Reuss. Calculation of flow limits of mixed crystals on the basis of the plasticity of mono-crystals. *Zeitschrift für Angewandte Mathematik und Mechanik*, 9:49–58, 1929.

[125] J.R Rice. A path independent integral and the approximate analysis to fracture mechanics in yielding materials. *Journal of Strain Analysis*, 1:145–153, 1966.

[126] G.J Rodin. Eshelby's inclusion problem for polygons and polyhedra. *Journal of the Mechanics and Physics of Solids*, 44(12):1977–1995, 1996.

[127] J.G Rots, P. Nauta, Kusters G.M.A., and J. Blaauwendraad. Smeared crack approach and fracture localization in concrete. *Heron*, 30(1), 1985.

[128] M. H. Sadd, Q. Dai, V. Parameswaran, and A. Shukla. Simulation of asphalt materials using finite element micromechanical model with damage mechanics. *Transportation Research Record: Journal of the Transportation Research Board*, 1832:86–95, 2003.

[129] R. Sankaran and C. Laird. Deformation field of a misfitting inclusion. *Journal of the Mechancis and Physics of Solids*, 24(4):251–262, 1976.

[130] I. Sevostianov, N. Yilmaz, V. Kushch, and V. Levin. Effective elastic properties of matrix composites with transversely-iostropic phases. *International Journal of Solids and Structures*, 42:455–476, 2005.

[131] J. C. Simo and J.W Ju. Strain- and stress based continuum damage models - ii. computational aspects. *International Journal of Solids and Structures*, 23(7):841–870, 1987.

[132] J. C. Simo and J.W Ju. Strain- and stress based continuum damage models i. formulation. *International Journal of Solids and Structures*, 23(7):821–840, 1987.

[133] L.M Smith and V. Yakhot. Finite-size effects in forced two-dimensional flow. *Journal of Fluid Mechanics*, 274:115–138, 1994.

[134] F. V. Souza. Multiscale model for predicting damage evolution in composites due to impact loading. *Composite Science and Technology*, 68(13):2624–2634, 2008.

[135] J. Stoer and F. L. Bauer. *Einführung in die numerische Mathematik: Unter Berücksichtigung von Vorlesungen von F. L. Bauer*, volume 105 of *Heidelberger Taschenbücher*. Springer, Berlin, 3rd edition, 1979.

[136] G. Strang and G. J. Fix. *An analysis of the finite-element method*. Prentice-Hall series in automatic computation. Prentice-Hall, Englewood Cliffs and NJ, 1st edition, 1973.

[137] E. B. Tadmor, R. S. Elliott, and R. E. Miller. *Continuum mechanics and thermodynamics: From fundamental concepts to governing equations*. Cambridge University Press, Cambridge and New York, 2012.

[138] R. Talreja. Multi-scale modeling in damage mechanics of composite materials. *Journal of Materials Science*, 41(20):6800–6812, 2006.

[139] K. Tanaka and T. Mori. Note on volume integrals of the elastic field around an ellipsoidal inclusion. *Journal of Elasticity*, 2:199–200, 1972.

[140] C. Temperton. Self-sorting mixed-radix fast fourier transform. *Journal of Computational Physics*, 52:1–23, 1983.

[141] S. P. Timoshenko and J. N. Goodier. *Theory of elasticity*. McGraw-Hill, New York, 3rd edition, 1987.

[142] T. C. Ting. *Anisotropic elasticity: Theory and applications*. Oxford University Press, New York, 1996.

[143] T. C. Ting and V.-G Lee. The three-dimensional green's function for general anisotropic linear elastic media. *The Quarterly Journal of Mechanics and Mathematics*, 50(3):407–426, 1997.

[144] R.A Toupin. Elastic materials with couple-stresses. *Archive For Rational Mechanics And Analysis*, 11(1):385–414, 1962.

[145] D. L. Turcotte and R. Shcherbakov. Can damage mechanics explain temporal scaling laws in brittle fracture and seismicity? *Pure and Applied Geophysics*, 163(5-6):1031–1045, 2006.

[146] G. Uva and G. Salerno. Towards a multiscale analysis of periodic mason brickwork: a fem algorithm with damage and friction. *International Journal of Solids and Structures*, 43(13):3739–3769, 2006.

[147] J. G. M. van Mier. Mulitaxial strain-softening of concrete part i: fracture. *Materials and Structures*, 19(3):179–190, 1986.

[148] W. Voigt. Über die beziehungen zwischen den beiden elasticitätskonstanten isotroper körper. *Ann. Phys.*, 38:573–587, 1889.

[149] W. Voigt. *Lehrbuch der Kristallphysik*. Leipzig, 1910.

[150] G. Z. Voyiadjis. Multiscale analysis of multiple damage mechanisms coupled with inelastic behavior of composite materials. *Journal of Engineering Mechanics*, 127(Special Issue):636–645, 2001.

[151] X. Weiya and W. Lide. Study on statistical damage constitutive model of rock. *Chinese Journal of Rock Mechanics and Engineering*, 6, 2002.

[152] A.A Wells. Unstable crack propagation in metals: Cleavage and fast fracture. *Proceedings of the Crack Propagation Symposium*, 1, 1961.

[153] M.L Williams. On the stress distribution at the base of a stationary crack. *Journal of Applied Mechanics*, 24:109–114, 1957.

[154] J. R. Willis. Variational and related methods for the overall properties of composites. *Advances in Applied Mechanics*, 21:1–78, 1981.

[155] K. Wilmanski. *Continuum Thermodynamics - Part I: Foundations*. World Scientific, Singapore, 2008.

[156] F.G Yuan, S. Yang, and B. Yang. Three-dimensional green's functions for composite laminates. *International Journal of Solids and Structures*, 40:331–342, 2003.

Curriculum Vitae

Personal Data

Name	Christoph Moos
Date of Birth	April 15th, 1983
Place of Birth	Iserlohn, NRW, Germany
Nationality	german
Marital Status	unmarried

School Education

08/1993 – 06/2002	Mariengymnasium (Highschool), Bocholt, NRW, Germany

Military Service

10/2002 – 06/2003	PiBtl. 140 (Engineers), Emmerich, NRW, Germany

University Education

10/2003 – 02/2009	Mechanical Engineering
	Ruhr-University of Bochum, Germany,
	focus: Applied Mechanics
	Diploma (Dipl.-Ing.)

Professional Occupation

03/2009 – present	Research Assistant, Lehrstuhl für Allgemeine Mechanik,
	Ruhr-University of Bochum, German